Multi-Technique Characterization of 3.45 Ga Microfossils on Earth: A Key Approach to Detect Possible Traces of Life in Returned Samples from Mars

Laura Clodoré, Frédéric Foucher, Keyron Hickman-Lewis, Stéphanie Sorieul, Jean Jouve, Matthieu Réfrégiers, Guillaume Collet, Stéphane Petoud, Bernard Gratuze, Frances Westall

ASTROBIOLOGY
Volume 24, Number 2, 2024

DOI: 10.1089/ast.2023.0089

Multi-Technique Characterization of 3.45 Ga Microfossils on Earth: A Key Approach to Detect Possible Traces of Life in Returned Samples from Mars

Laura Clodoré,[1] Frédéric Foucher,[1,2] Keyron Hickman-Lewis,[3,4] Stéphanie Sorieul,[5] Jean Jouve,[5] Matthieu Réfrégiers,[1] Guillaume Collet,[1,6] Stéphane Petoud,[1] Bernard Gratuze,[7] and Frances Westall[1]

Abstract

The NASA Mars 2020 Perseverance rover is actively exploring Jezero crater to conduct analyses on igneous and sedimentary rock targets from outcrops located on the crater floor (Máaz and Séítah formations) and from the delta deposits, respectively. The rock samples collected during this mission will be recovered during the Mars Sample Return mission, which plans to bring samples back to Earth in the 2030s to conduct in-depth studies using sophisticated laboratory instrumentation. Some of these samples may contain traces of ancient martian life that may be particularly difficult to detect and characterize because of their morphological simplicity and subtle biogeochemical expressions. Using the volcanic sediments of the 3.45 Ga Kitty's Gap Chert (Pilbara, Australia), containing putative early life forms (chemolithotrophs) and considered as astrobiological analogues for potential early Mars organisms, we document the steps required to demonstrate the syngenicity and biogenicity of such biosignatures using multiple complementary analytical techniques to provide information at different scales of observation. These include sedimentological, petrological, mineralogical, and geochemical analyses to demonstrate macro- to microscale habitability. New approaches, some unavailable at the time of the original description of these features, are used to verify the syngenicity and biogenicity of the purported fossil chemolithotrophs. The combination of elemental (proton-induced X-ray emission spectrometry) and molecular (deep-ultraviolet and Fourier transform infrared) analyses of rock slabs, thin sections, and focused ion beam sections reveals that the carbonaceous matter present in the samples is enriched in trace metals (*e.g.*, V, Cr, Fe, Co) and is associated with aromatic and aliphatic molecules, which strongly support its biological origin. Transmission electron microscopy observations of the carbonaceous matter documented an amorphous nanostructure interpreted to correspond to the degraded remains of microorganisms and their by-products (extracellular polymeric substances, filaments…). Nevertheless, a small fraction of carbonaceous particles has signatures that are more metamorphosed. They probably represent either reworked detrital biological or abiotic fragments of mantle origin. This study serves as an example of the analytical protocol that would be needed to optimize the detection of fossil traces of life in martian rocks. Key Words: Microfossils—Biosignatures—Microanalysis—Organic material—Archean—Mars. Astrobiology 24, 190–226.

[1]CNRS-Centre de Biophysique Moléculaire, Orléans, France.
[2]CNRS-Conditions Extrêmes et Matériaux: Haute Température et Irradiation, Orléans, France.
[3]Natural History Museum, London, United Kingdom.
[4]Dipartimento BiGeA, Università di Bologna, Bologna, Italy.
[5]University of Bordeaux, CNRS, IN2P3, CENBG, Gradignan, France.
[6]Chair of Cosmetology, AgroParisTech Innovation, Orléans, France.
[7]CNRS-Institut de Recherche sur les ArchéoMATériaux, Orléans, France.

1. Introduction

While the current conditions on Mars make the presence of extant life unlikely at its surface, life may have appeared and developed in its early history, during the Noachian period (>3.5 billion years ago, Ga) when liquid water was present at the surface and the planet sustained an atmosphere (McKay and Stoker, 1989). Early in their histories, before 3.5 Ga, the environments on Earth and on Mars were locally similar, characterized by a CO_2-rich atmosphere, bodies of liquid water at the surface, and the availability of organic molecules and other bio-essential elements (*e.g.*, C, H, N, O, P, S, Cl, Se) provided by rocks and meteorites (Des Marais, 2010). Given the presence of the necessary ingredients for prebiotic chemistry, and local environments that could have hosted the emergence of life, it is proposed that life may have appeared independently on Mars (McKay and Stoker, 1989; Des Marais *et al.*, 2008). However, by comparison with the globally habitable situation on Earth and the history of the evolution of terrestrial life, Mars suffered from a spatiotemporal variability in its early habitability and a lack of long-term habitable environments (Cockell *et al.*, 2012; Westall *et al.*, 2013, 2015b). Thus, if life ever emerged on Mars, life forms on the planet are likely to have remained relatively primitive, perhaps similar to terrestrial chemotrophs (Westall *et al.*, 2015b) and/or to anoxygenic phototrophs (Hickman-Lewis *et al.*, 2022a). Of the chemotrophs, chemolithotrophs use inorganic compounds in rocks and minerals as a source of energy, whereas chemoorganotrophs obtain their energy from the oxidation of organic substrates. These kinds of microorganisms were common on the Early Earth, inhabiting globally ubiquitous anaerobic, volcano–sedimentary environments (Westall *et al.*, 2015b).

Many present and future missions to Mars have the objective of exploring its geological environment to search for potential traces of life. Since 2012, the Mars Science Laboratory Curiosity rover has been exploring Gale crater to examine records of past water, climate, and habitability on Mars. In particular, the exploration of the central mound of the crater, Mount Sharp, and the surrounding plain has revealed the presence of ancient streams, lakes, and deltas indicating (sub)surface environments that were intermittently habitable for at least a few million years (Grotzinger *et al.*, 2015). The lower strata of Mount Sharp are composed of clastic sedimentary rocks deposited in the beds of lakes or in fluvial environments. They are made up of basaltic minerals that have undergone diagenetic processes and include hydrated phases that indicate the aqueous alteration of basaltic material. The global environmental transition from a warmer and wet climate to a cold and dry climate, characterized by a transition from smectite-bearing to sulfate-bearing strata (Bibring *et al.*, 2006; Rampe *et al.*, 2020), has been observed in Gale Crater. Moreover, the rover also detected a diversity of organic molecules of exogeneous (meteoritic) and probable endogenous (martian) origin preserved in the Gale crater sediments (Freissinet *et al.*, 2015; Eigenbrode *et al.*, 2018; Millan *et al.*, 2022). The Mars 2020 Perseverance rover is actively exploring Jezero Crater to locate and characterize habitable paleoenvironments and search for possible evidence of life (Farley *et al.*, 2020).

The rover has started collecting rock samples with high biosignature preservation potential that will be returned to the Earth in the 2030s for high-resolution studies (Farley *et al.*, 2022). Samples collected during the first Science Campaign include four pairs of igneous rock cores from outcrops located on the crater floor; specifically, four samples of basaltic to andesitic lava flow from the Máaz formation and four samples of an olivine cumulate from the Séítah formation (Simon *et al.*, 2023). Fluorescence spectroscopy data identified the presence of potential aromatic organic materials in association with the alteration mineralogy of the igneous units of the crater floor (Scheller *et al.*, 2022; Sharma *et al.*, 2023). Another nine sedimentary rock cores, including sulfate minerals preserving possible organic materials (Benison *et al.*, 2023), have been taken. Two regolith samples likely composed of sedimentary and igneous grains have been collected from the delta front and the upper fan (Farley and Stack, 2023). For almost every pair of samples collected during the first and second science campaigns, one sample was deposited by Perseverance in a first sample cache (the Three Forks sample depot) on the martian surface whereas the second was retained within the rover to be cached with future samples (Simon *et al.*, 2023).

Further, the ExoMars Rosalind Franklin rover, to be launched in 2028, will be equipped with a suite of instruments, including a drill that will allow the collection of samples at depths up to 2 m in the subsurface (Vago *et al.*, 2017). Following on from the rationale regarding the limited possibility of evolution of life on Mars, our hypothesis is that putative ancient martian life, dating from the Late Noachian to Early Hesperian, could be relatively similar to the chemotrophs detected in Paleoarchean (ca. 3.2–3.5 Ga) terrestrial rocks, that is, very small microbial life forms that leave very subtle fossilized traces (Westall *et al.*, 2006, 2015b). Yet, as we demonstrate here, such traces of life are difficult to analyze on Earth even with sophisticated laboratory instrumentation. Their traces will thus be even more difficult to document on Mars using *in situ* instrumentation (Azua-Bustos, 2023), underlining the importance of Mars Sample Return (MSR).

To evaluate the detection of traces of life in martian rocks *in situ* and/or in samples returned to Earth, we studied fossil traces of life associated with ancient volcano-sedimentary materials from the 3.46 Ga Kitty's Gap Chert (East Pilbara, Australia) (Fig. 1). These sediments may contain some of the oldest traces of life known on Earth in the form of silicified microorganisms (Westall *et al.*, 2006, 2011, 2015b). As described by Westall *et al.* (2006, 2011, 2015b), sedimentary rocks of the Kitty's Gap Chert hosted microorganisms interpreted as anaerobic, autotrophic chemolithotrophs that coat the surfaces of volcanic particles and occur in the fine-grained, dusty volcanic matrix of the sediments. Most of the interpreted microfossils are silicified, very small coccoidal structures <1 μm in size forming monolayer colonies (several microns to tens of microns in size) over the surfaces of volcanic particles. They are always associated with a film-like phase interpreted as extracellular polymeric substances (EPS) produced by microbes to attach themselves on surfaces of mineral particles from which they can absorb the chemical elements more efficiently. The purported microfossils are carbonaceous; carbon isotopic compositions of individual, mm thick, microfossil-

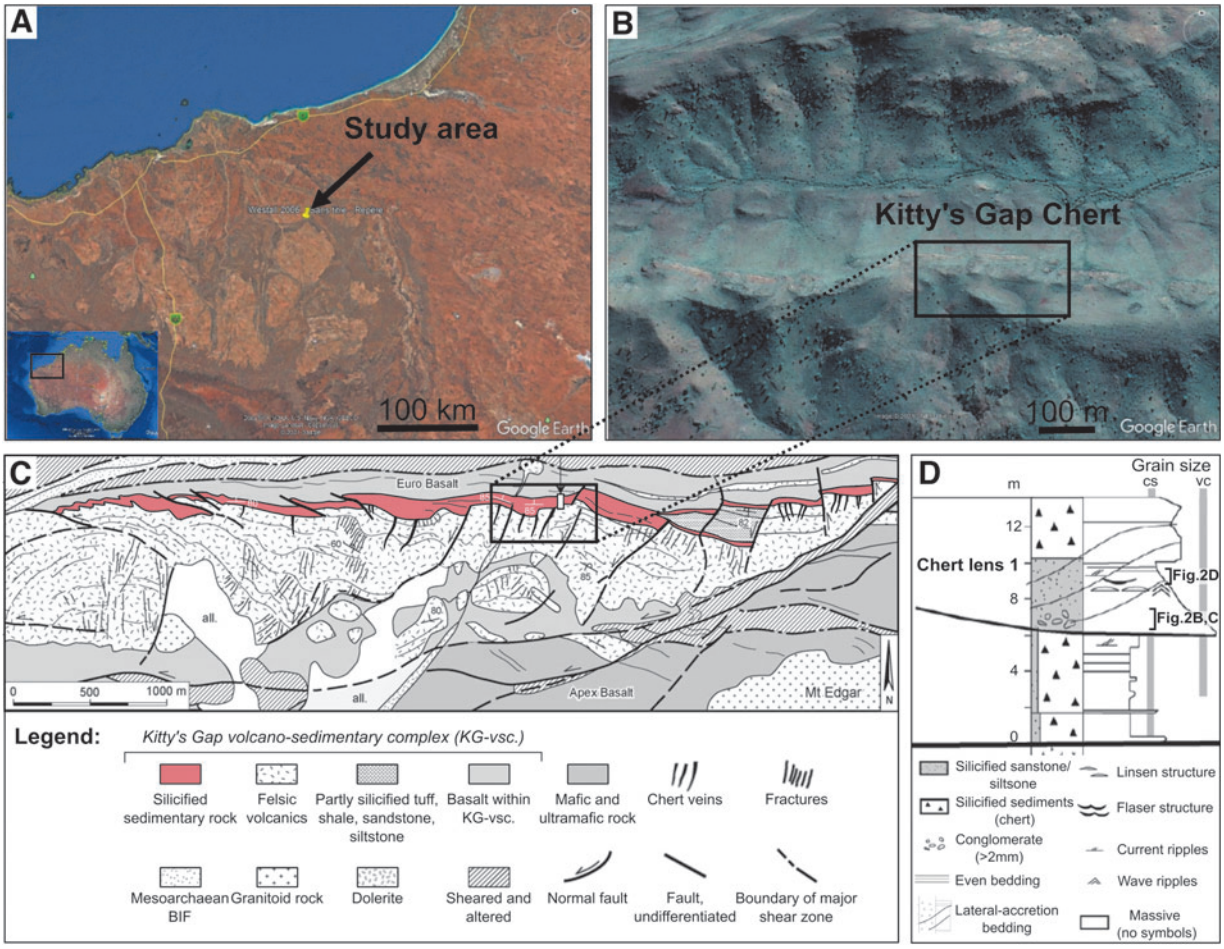

FIG. 1. **(A)** Satellite image (Google Earth) of the Pilbara Craton within Australia; black arrow indicates the location of the Kitty's Gap Chert. **(B)** Satellite image (Google Earth) of the Kitty's Gap Chert with black box indicating the location of the main study area from which the studied samples were obtained. **(C)** Detailed geological cross-section of the Kitty's Gap volcano-sedimentary sequence (KG-vsc.; modified after de Vries, 2004). **(D)** Sedimentary log of chert lens 1 in the Kitty's Gap Chert of which samples from this study are part (Fig. 2B–D), with grain size: coarse silt (cs) and very coarse sand (vc) (modified after de Vries et al., 2010).

containing sediment layers range from −25.9‰ to −27.8‰ (Westall *et al.*, 2006) and are compatible with microbial fractionation (Schidlowski, 2001).

However, the low biomass production rate and metabolic productivity of the interpreted chemolithotrophs resulted in low concentrations of only 0.01–0.05 wt % of total organic carbon in the sediments (Westall *et al.*, 2006). In addition to the colonies of coccoids, detrital fragments of microbial filaments and phototrophic mats also occur, together with rare rod-shaped microorganisms (Westall *et al.*, 2006). Because of their simple morphology, these purported fossilized microorganisms are still considered to be controversial despite numerous indicators of their syngenicity and biogenicity (Wacey, 2009). Studies of abiotic biomorphs have also highlighted the difficulties in interpreting biogenicity (García-Ruiz *et al.*, 2003, 2009; Cosmidis and Templeton, 2016; Criouet *et al.*, 2021). If potential traces of primitive life exist in returned samples from Mars and if they resemble interpreted primitive microfossils in the Kitty's Gap Chert and other early Earth horizons, definitive interpretations of their biogenicity will be hotly debated. For this reason, the Kitty's Gap microfossils provide an ideal subject for testing advanced techniques to document complementary types of biosignatures. Such sequences of analyses can be considered trial runs of the approaches needed if similar potential microfossils occurred in samples returned from Mars. Moreover, the original interpretation of the microfossils in the Kitty's Gap Chert was made by using technologies that have since been improved. New understanding of what constitutes reliable biosignatures (Meadows *et al.*, 2022) and new state-of-the-art technologies are now available that can elucidate the biogenicity of the structures and their microenvironment (Brasier *et al.*, 2015).

Biosignatures are defined in this study as structures, chemical signatures, and substances consistent with the action of a biological agent (Des Marais *et al.*, 2008). In particular, the measurements must meet a certain number of criteria necessary to affirm the detection of traces of life, which convinces the scientific community (the burden of proof) (Brasier *et al.*, 2002), namely instrumental criteria, such as sensitivity (the concentration measured must be greater than the limit of quantification to be detected), the absence of contamination, and the ability to repeat measurements under similar conditions, as well as contextual

criteria regarding the detectability, preservation, and reliability (distinction from abiotic backgrounds) of biosignatures in the environment (Neveu *et al.*, 2018). Other criteria such as compatibility with what we know about life on Earth and the last resort hypothesis (the biological hypothesis is the only plausible hypothesis that can explain the origin of the observed structures) are also crucial (Neveu *et al.*, 2018). Multiple measurements are, therefore, necessary to satisfy all of these criteria and increase the probability of confirming the biological origin of proposed traces of life.

In this study, we used multiple complementary methods to fully characterize the purported fossilized traces of life of the Kitty's Gap Chert and, thus, evaluate their biogenicity (and syngenicity). Our approach, based on a maximum of physico-chemical data to confirm the biogenicity of the investigated structures, provides an example of the degree of analytical rigor that will be needed to search for potential traces of life in martian rocks. This includes the following:

- Documentation of the paleoenvironment through study of sedimentary facies (*e.g.*, laminations, micro-ripples, lenticular bedding, orientation of volcanic clasts), petrology (*e.g.*, nature, composition, size and shape of clasts), mineralogy (including biominerals), and geochemistry (*e.g.*, trace and rare-earth elements);
- Physical characterization of carbonaceous phases: micro- and nanostructure (*e.g.*, diffuse carbon, films, particles), and crystallography (amorphous or graphitized);
- Chemical characterization of the carbonaceous matter: analysis of elemental and molecular composition of carbonaceous materials in the sediments;
- Distribution of carbonaceous materials in the rock: detection and localization of carbonaceous deposits, in particular with respect to volcanic particle surfaces and the volcanic dust-filled sedimentary matrix.

2. Materials and Methods

2.1. Geological setting

The Kitty's Gap Chert is a well-preserved sedimentary stratigraphic unit within the Pilbara craton, Australia, that forms part of the Panorama Formation, in the Coppin Gap greenstone belt (Fig. 1). The sedimentary horizon in question is underlain by felsic volcanics and overlain by volcanics of basaltic composition, whose felsic rocks are dated at 3.446 Ga (de Vries, 2004; de Vries *et al.*, 2006). The succession is more than 40 m thick (de Vries *et al.*, 2010). The Kitty's Gap Chert is a typical example of silicified volcanoclastic sediments (80–99% of silica) deposited in a shallow-water littoral environment in the vicinity of hydrothermal vents linked to a volcanic system (de Vries, 2004; de Vries *et al.*, 2006; Westall *et al.*, 2006, 2011). The sediments were silicified by Si-enriched Archean seawater (de Vries, 2004; van den Boorn *et al.*, 2010). Silica was also sourced from abundant hydrothermal veins that reach into the lowermost layer of the sediments (de Vries, 2004; de Vries *et al.*, 2010), as well as via silica-saturation of pore waters owing to devitrification of volcanic clasts during diagenesis.

2.2. Sample collection and preparation

We investigated samples from the lower 4 m of the Kitty's Gap Chert (120°04′53″E; 20°53′62″S). The samples were collected by Frances Westall (2000). Samples 00AU39 and 00AU40 are part of the main sedimentary chert lens 1, and sample 00AU37b was obtained from sediments brecciated by an intruding hydrothermal vein (Fig. 2A). Sample 00AU37b was collected directly from within a hydrothermal silica vein in the lower part of the succession and is part of a conglomerate (00AU37) that exhibits millimeter- to centimeter-size, light-colored clasts in a black chert matrix (Fig. 2B).

Sample 00AU39 is a conglomerate located a few centimeters away from the hydrothermal vein, at the base of chert lens 1, and is composed of dark pebbles surrounded by coarsely laminated millimeter- to centimeter-thick deposits (Fig. 2C). Sample 00AU40 is located $\sim$15 m east of the hydrothermal vein, at the top of chert lens 1, and is a heterolithic chert alternating between coarse light gray and fine dark gray laminations characterized by diverse sedimentary structures, such as current micro-ripples, flaser-linsen bedding, and undulating lamination (Fig. 2D).

For sample 00AU37b, a powder with a particle size of <80 μm and one thin section 30 μm thick were prepared. Powders with a particle size of <80 μm, slabs a few centimeters thick, and thin sections 70 μm thick were prepared from samples 00AU39 and 00AU40 for multiscale and multi-technique analysis. Detached thin sections, 30 and 70 μm thick, were also prepared from 00AU39 and 00AU40. In addition, focused ion beam (FIB) sections of $\sim$100 nm thickness were prepared from thin sections of 00AU39 and 00AU40 for nanoscale analysis. All samples are part of the International Space Analogue Rock Store (ISAR) collection, CBM, CNRS (Orléans, France; http://isar.cnrs-orleans.fr/isar/) (Bost *et al.*, 2013).

2.3. Methods

2.3.1. Optical microscopy. Two microscopes, a Nikon Eclipse Ti equipped with a Nikon DS-Fi3 camera and an Olympus BX51 equipped with a Pixelink M20-CYL camera, were used at CBM, CNRS. The first microscope was used to produce high-resolution (<1 μm/pixel) image mosaics of the full thin sections to document the larger scale structures and textures of the rocks and to locate regions of interest (ROIs). The second microscope was used to analyze the petrological context and observe the alteration of volcanic clasts and the distribution of the carbonaceous deposits. Specific ROIs were chosen and imaged by using transmitted and reflected polarized light at different magnifications (50×, 200×, 500× and 1000×).

2.3.2. (Scanning) transmission electron microscopy. Two transmission electron microscopy (TEM)/scanning transmission electron microscopy (STEM) instruments, a JEOL ARM200 CFEG (MACLE facility, CNRS) and a PHILIPS CM20 (ICMN, CNRS), were used to obtain nanoscale resolution images of the microstructure (*e.g.*, particle size and shape) and the crystallography of minerals and carbonaceous matter in FIB sections. One hundred nanometers thick FIB sections were prepared at IEMN, CNRS (Lille, France), using a ZEISS Crossbeam

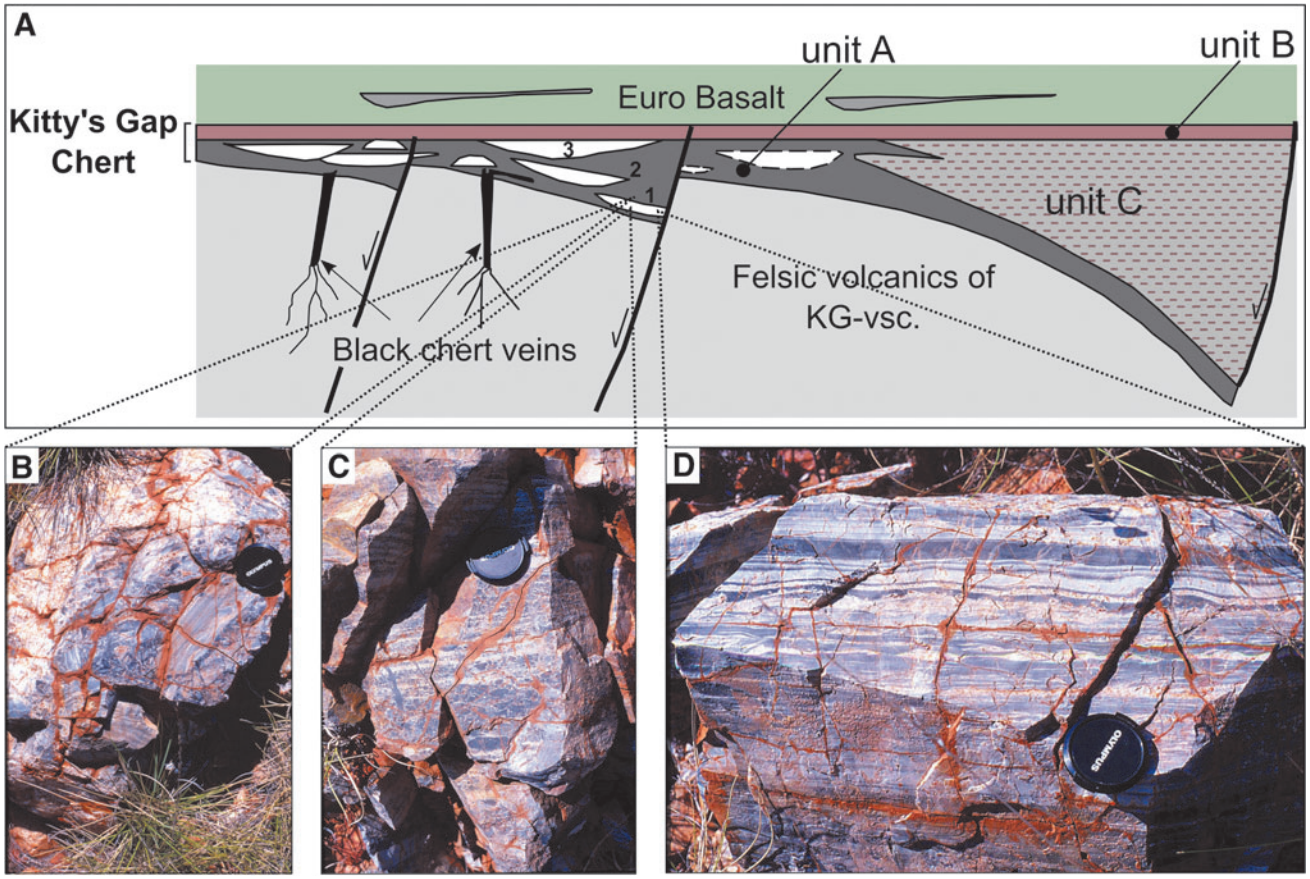

FIG. 2. **(A)** Schematic drawing (not to scale, width of geological cross-section ~1.5 km) of silicified sediments of Kitty's Gap and chert lenses, including chert lenses numbered 1–3 from unit A (modified after de Vries, 2004). Field photographs of **(B)** sample 00AU37 showing a conglomerate composed of white and gray clasts in a black chert vein (sample 00AU37b) extracted from a hydrothermal vein crossing the chert lens 1, **(C)** sample 00AU39 showing a conglomerate formed of dark pebbles embedded in a sandy material at the base of chert lens 1, and **(D)** sample 00AU40 showing dark and light laminations with micro-ripples, flaser-linsen bedding and undulating lamination at the top of chert lens 1. Lens cap for scale, 5.4 cm diameter. Photographs taken by Frances Westall (2000).

microscope. TEM imaging and STEM observations were carried out using a 200 keV energy beam, with a current of 15 μA, and a spatial resolution of ca. 0.1 nm. Major element analyses were performed by energy dispersive X-ray (EDX).

2.3.3. Raman spectroscopy. Raman spectra and images were recorded on thin sections using a WITec Alpha 500RA at CBM, CNRS, to detect, identify, and map the mineral phases and carbonaceous matter. Data were acquired using a green laser (Nd:YAG frequency doubled, excitation wavelength 532 nm), 20× or 50× objectives with numerical apertures of 0.40 and 0.75, and measured spot sizes of ca. 1.6 μm and ca. 0.8 μm diameter, respectively. The laser power was set between 5 and 14 mW at the sample surface. The spatial resolution of the maps depends on the ratio of the scan size over the number of spectra per line but was approximately about 1 μm/spectrum. The average spectral resolution was ~3 cm^{-1} using a 600 g/mm grating. Acquisition time was 0.1–0.4 s per spectrum per pixel. For more details about Raman spectroscopy imaging protocols, the reader is directed to the work of Foucher *et al.* (2017).

2.3.4. Synchrotron radiation deep-ultraviolet fluorescence (micro)spectroscopy. Deep-ultraviolet (DUV) fluorescence spectroscopy (excitation wavelength 275 nm) was performed on detached thin sections by using Telemos, a DUV microscope, and Polypheme, a DUV inverted microspectrofluorometer, at the DISCO beamline, Synchrotron SOLEIL (Saint-Aubin, France). This method was used to identify and map aromatic compounds, minerals, and metallic oxides in the samples. Microscopy observations were made with a 100× objective with a spatial resolution of 7.2 μm/pixels (glycerin immersion). Different filters were used to detect the aromatic molecules (329–351 and 352–388 nm) (Ménez *et al.*, 2018), minerals, and metallic oxides (412–438, 420–480, and 499–529 nm) (MacRae and Wilson, 2008; Gaft *et al.*, 2015; Zhyrovetsky *et al.*, 2017). The spectrometer acquires spectra between 285 and 550 nm using a 100× objective and an acquisition time of 10 s per spectrum per pixel.

2.3.5. Synchrotron radiation X-ray fluorescence spectroscopy. X-ray fluorescence (XRF) imaging of thin sections was carried out on detached thin sections using the DiffAbs beamline (Gueriau *et al.*, 2020) at Synchrotron SOLEIL to identify and map the distribution and concentration of major and traces elements. The microbeam setup consists of two cylindrical, vertically focusing mirrors, a

fixed-exit double crystal monochromator made of two Si(111) crystals, and two mirrors in Kirkpatrick-Baez geometry, which allow monochromatizating and focusing of the beam down to $\sim 10 \times 10\,\mu m$. All measurements were performed using an incident beam energy of 13 keV, permitting the detection of elements from the K line of Ar at 2.4 keV (from ambient air) to the L line of Ge at 11 keV. The spatial resolution was 10 to 40 μm, and the spectral resolution was 120–150 eV, with an integration time of 80–120 ms. XRF spectra were recorded with a four-element silicon drift detector (Vortex).

2.3.6. Fourier transform infrared spectroscopy. Transmission Fourier transform infrared (FTIR) mapping and spectra were performed on detached thin sections using a Thermo Nicolet iN40 Infrared Imaging Microscope at the Imaging and Analysis Centre, Natural History Museum (London, United Kingdom), to determine the molecular composition of the carbonaceous matter, focusing on aliphatic compounds within the wavenumber range 2800–3040 cm^{-1}, and aromatic/alkenic compounds within the wavenumber range 1300–1800 cm^{-1}.

Multiple analyses were made with a 30 μm spatial resolution and a 4 cm^{-1} spectral resolution. A reference background spectrum in air was taken before each analysis and subtracted from the sample spectrum. In addition, infrared (IR) signatures of aliphatic CH_2 and CH_3 ratios were used to estimate the length of the aliphatic chain and the degree of branching in the carbonaceous matter, permitting interpretation of the nature of precursor (*i.e.*, pre-degradation) organic molecules, such as membrane lipids, using the following equations, where $Abs(CH_3)$ and $Abs(CH_2)$ refer to the absorbance peaks of the asymmetric stretching bands of the aliphatic CH_3 (end-methyl, 2960 cm^{-1}) and CH_2 (methylene, 2925 cm^{-1}) after linear baseline correction (Lin and Ritz, 1993; Igisu *et al.*, 2009):

$$\frac{CH_2}{CH_3} = \frac{Abs(CH_2)}{Abs(CH_3)} = \frac{Abs(\sim 2925\ cm^{-1})}{Abs(\sim 2960\ cm^{-1})} \quad (1)$$

$$\frac{CH_3}{CH_2} = R_{3/2} = \frac{Abs(CH_3)}{Abs(CH_2)} = \frac{Abs(\sim 2960\ cm^{-1})}{Abs(\sim 2925\ cm^{-1})} \quad (2)$$

2.3.7. Proton-induced X-ray emission. Proton-induced X-ray emission (PIXE) spectrometry maps and spectra were acquired on carbon-coated, detached thin sections using microscale proton-induced X-ray emission (μPIXE) spectrometry (Barberet *et al.*, 2021) combined with Rutherford Backscattering Spectrometry (RBS) at the AIFIRA facility, CENBG (Gradignan, France), to study the distribution of trace elements, in particular transition metals in the carbonaceous matter at a scale of 10–100 μm. Three Si-detectors (one RBS and two PIXE) collected the data: the RBS was used for charge monitoring, whereas the two PIXE detectors were used for elemental quantification and mapping. The first PIXE detector is equipped with an aluminum ''Funny Filter'' (thickness 100 μm, hole size 2 mm) and a Kapton filter (thickness 50 μm). The second PIXE detector is equipped with only an aluminum ''Funny Filter'' (thickness 100 μm).

We used a microbeam of 3 MeV proton (1 μm diameter) with a current of 200 pA; a scan speed of 500 μs/pixel; and a total acquisition time of ca. 10 h per analysis. For the last analyses, we optimized these parameters by using a beam of 2.5 μm with a current of 900 pA, which allowed more accurate mapping and quantification, with a total acquisition of ca. 5 h. For some analyses, we only used one PIXE detector equipped with an aluminum ''Funny Filter'' (thickness 100 μm, hole size 3.64 mm) and a Kapton filter (thickness 50 μm). Two standards were used for the first setup, NIST1411 (soft borosilicate glass) and Inox (iron, chromium, zinc and nickel metallic elements), and one for the second setup, NIST610 (borosilicate glass). These standards cover the energy range from 1 to 20 keV in which trace elements from Si to Mo could be detected.

2.3.8. Inductively coupled plasma optical emission and mass spectrometry. Bulk geochemistry was measured on powders of the three samples—00AU37b, 00AU39, and 00AU40—using inductively coupled plasma optical emission spectrometry (ICP-OES) and ICP-mass spectrometry (ICP-MS) at CRPG (Nancy, France). Bulk major and trace elements were measured using iCapQ ICP-MS and iCap6500 ICP-OES instruments to reconstruct characteristics of the paleoenvironment.

2.3.9. Laser ablation inductively coupled plasma mass spectrometry. Laser ablation (LA)-ICP-MS analyses were performed on two slabs of ca. 1–2 cm thickness (one slab from sample 00AU39 and one from sample 00AU40) by using an Element XR ICP-MS (Thermo Fischer Scientific) coupled to a 193 nm Excimer (ArF) laser ablation system RESOlution M50E (Resonetics) equipped with an S155 Laurin cell at IRAMAT, CNRS.

Standard Reference Materials NIST 610 and NIST 612 were used for calibration and mass spectrometer tuning. Multiple transects of laser ablation line analyses were taken through various areas of interest to reconstruct paleoenvironmental variations at a local scale. Eleven lines were acquired in different laminations in sample 00AU40 and nine lines were acquired in major different structures in sample 00AU39 using a laser with an energy of 5 mJ, a frequency of 20 Hz, and a spot size of 100 μm.

The acquisition time was 30 s per spectrum after 10 s of uptake time to eliminate transient signal. Calibration was performed by using standards reference glass NIST 610 and NIST 612, which run periodically (every 20 samples) to correct for drift. NIST 610 and 612 were used to calculate the response coefficient (k) of each element (Gratuze, 1999, 2016), and the measured values of each element were normalized against ^{28}Si, the internal standard, to produce a final percentage.

Quantitative data for each structures of interest were obtained for the following isotopes: ^{23}Na, ^{24}Mg, ^{27}Al, ^{28}Si, ^{31}P, ^{39}K, ^{44}Ca, ^{47}Ti, ^{51}V, ^{52}Cr, ^{55}Mn, ^{57}Fe, ^{59}Co, ^{60}Ni, ^{65}Cu, ^{64}Zn, ^{71}Ga, ^{74}Ge, ^{75}As, ^{85}Rb, ^{88}Sr, ^{89}Y, ^{90}Zr, ^{93}Nb, ^{95}Mo, ^{121}Sb, ^{133}Cs, ^{137}Ba, ^{139}La, ^{140}Ce, ^{141}Pr, ^{146}Nd, ^{147}Sm, ^{153}Eu, ^{157}Gd, ^{159}Tb, ^{163}Dy, ^{165}Ho, ^{166}Er, ^{169}Tm, ^{172}Yb, ^{175}Lu, ^{178}Hf, ^{181}Ta, ^{208}Pb, ^{232}Th, and ^{238}U.

Trace and rare earth elements plus yttrium (REE+Y) compositions (the 15 lanthanides, yttrium, and scandium) of the bulk chert samples and areas of interest obtained by

ICP-MS and LA-ICP-MS were normalized by using Mud from Queensland (MuQ) (Kamber *et al.*, 2005) to remove the natural variations in REE + Y and to facilitate the comparison of measurements with the compositional characteristics of upper crustal reservoirs. MuQ represents a bimodal felsic and mafic input, that is, the terrigenous input expected from greenstone belts in the Archean oceans. Most Precambrian sedimentary deposits are characterized by a seawater REE + Y pattern modulated by hydrothermal and other influences (Bau and Dulski, 1996; Allwood *et al.*, 2010; Gourcerol *et al.*, 2015; Hickman-Lewis *et al.*, 2020b) showing:

- an enrichment in heavy REE (HREE) compared with light REE (LREE), and a low $(Pr/Yb)_{MuQ}$ ratio, signifying a marine influence;
- super-chondritic Y/Ho ratios (≥27), reflecting a marine input;
- negative Ce anomalies resulting from Ce(III) oxidation in the water column;
- positive Eu anomalies linked to a hydrothermal influence;
- positive La, Gd, Y, and Lu anomalies related to a marine input;
- flattening of normalized patterns via enrichment in LREE that results from terrigenous fluvial (continental runoff) input that is rapidly altered to typical seawater patterns during interactions with marine waters;
- an enrichment in middle REE, and particularly in HREE (Sm, Tm, Yb, and Lu), resulting from the adsorption of REE onto bacterial cell walls.

Elemental anomalies relative to neighboring and near-neighboring elements in ICP-MS and LA-ICP-MS plots were calculated following the methods proposed by Lawrence and Kamber (2006) and Lawrence et al. (2006):

$$(Ce/Ce*)_{MuQ} = Ce_{MuQ}/(Pr_{MuQ}(Pr_{MuQ}/Nd_{MuQ})) \quad (3)$$

$$(Eu/Eu*)_{MuQ} = Eu_{MuQ}/\left(Sm^2{}_{MuQ} \times Tb_{MuQ}\right)^{1/3} \quad (4)$$

$$(La/La*)_{MuQ} = La_{MuQ}/\left(Pr_{MuQ}(Pr_{MuQ}/Nd_{MuQ})^2\right) \quad (5)$$

$$(Y/Y*)_{MuQ} = Y_{MuQ}/(0.5Er_{MuQ} + 0.5Ho_{MuQ}) \quad (6)$$

$$(Gd/Gd*)_{MuQ} = Gd_{MUQ}/\left(Tb^2{}_{MUQ}xSm_{MUQ}\right)^{1/3} \quad (7)$$

The different methods used in this study are summarized in Supplementary Table S1 of Supplementary Data.

3. Results

3.1. Investigating the paleoenvironmental context

Sedimentological, petrological, mineralogical, and geochemical characterization of the chert samples were used to reconstruct the paleoenvironmental context of the volcano-sedimentary deposits.

3.1.1. Sedimentological characterization. The Kitty's Gap Chert is characterized by three distinct units (Fig. 2): units A and B composed of silicified volcanoclastic materials (forming the main part of Kitty's Gap) and unit C, which is thicker and mainly composed of shale and fine-grained sandstone and minor chert (de Vries *et al.*, 2010). The samples analyzed in this study were extracted from unit A, which is composed of *en echelon* stacking of cherts lenses, tens of meters wide, surrounded by even-bedded chert. The cherts lenses comprise dark and light gray sedimentary deposits with a well-preserved granular texture. Primary sedimentary structures can also be observed throughout the lenses, from low-angle oblique bedding at the bottom through extensive cross-bedding at the meter-scale to small-scale ripples to parallel bedding at the top (de Vries *et al.*, 2010).

3.1.2. Petrological characterization. Hand sample and optical microscopy observations of a rock sample and thin section from sample 00AU37b (silica vein) show a smooth, glassy texture where light veins, a few millimeters in diameter and composed of microcrystalline quartz, cross a homogenous black chert matrix (Fig. 3).

Rock samples and thin sections from samples 00AU39 and 00AU40 (Fig. 4) exhibit a microlithic texture that is typical of volcanic rocks—with phenocrystals embedded in a matrix composed of finer minerals, that is microliths, that are only visible under the microscope—and volcanic glass. The volcanic protoliths (*e.g.*, volcanic glass, K-feldspar, biotite, and amphibole) have been replaced by hydromuscovite (phyllosilicate enriched in SiO_2, Al_2O_3, and K_2O that contains variable amounts of traces such as Fe_2O_3, MgO, and Na_2O) and are outlined by nanometer-sized Ti-oxide spherules (Orberger *et al.*, 2006; Westall *et al.*, 2006). Silica veins also appear in these samples, ranging in width from <100 μm up to a few millimeters. In sample 00AU39 located from near the hydrothermal vein, the silica veins consist of coarse-grained quartz (<300 μm in diameter) visible in analyzed polarized light and outlined with flakes of sericite.

Sample 00AU39 is mostly composed of rounded to angular, dark pebble-like structures surrounded by a light material composed of coarse particles (Fig. 4A, B). The light layers are enriched in poorly sorted volcanic protoliths replaced by silica and hydromuscovite (Fig. 4C), with particle sizes varying between 50 and 500 μm. The dark pebbles are more homogenous and comprise fine-grained volcanic dust particles in a silica gel-like matrix with a homogenous grain size that is <20 μm (well sorted), intermixed with silica and rare, larger volcanic protoliths (<100 μm; Fig. 4C).

Sub-horizontal stylolites are also visible through the rock and correspond to saw-tooth surfaces along which the mineral matrix has been removed by pressure dissolution (Fig. 4B, C).

Sample 00AU40 (KG 1 of Orberger *et al.*, 2006) is characterized by several horizontal laminations that alternate between light gray and dark gray (Fig. 4D, E). The light gray laminations are composed of coarser material, such as volcanic protoliths replaced by silica and hydromuscovite (Fig. 4F), with particle sizes varying between 50 and 500 μm (poorly sorted). The regular and homogenous dark gray laminations are primary volcanic material formed of volcanic ash deposits (<20 μm; well sorted) mixed with silica and with rare volcanic protoliths (<100 μm; Fig. 4F).

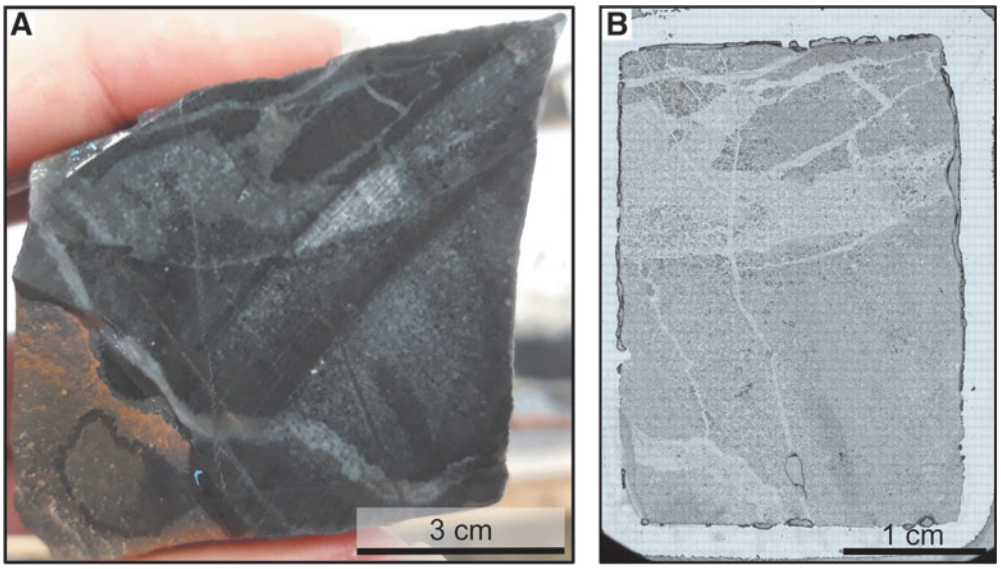

FIG. 3. **(A)** Photograph of the slab from which thin section 00AU37b was prepared. **(B)** Image mosaic of thin section 00AU37b (Nikon Eclipse Ti microscope).

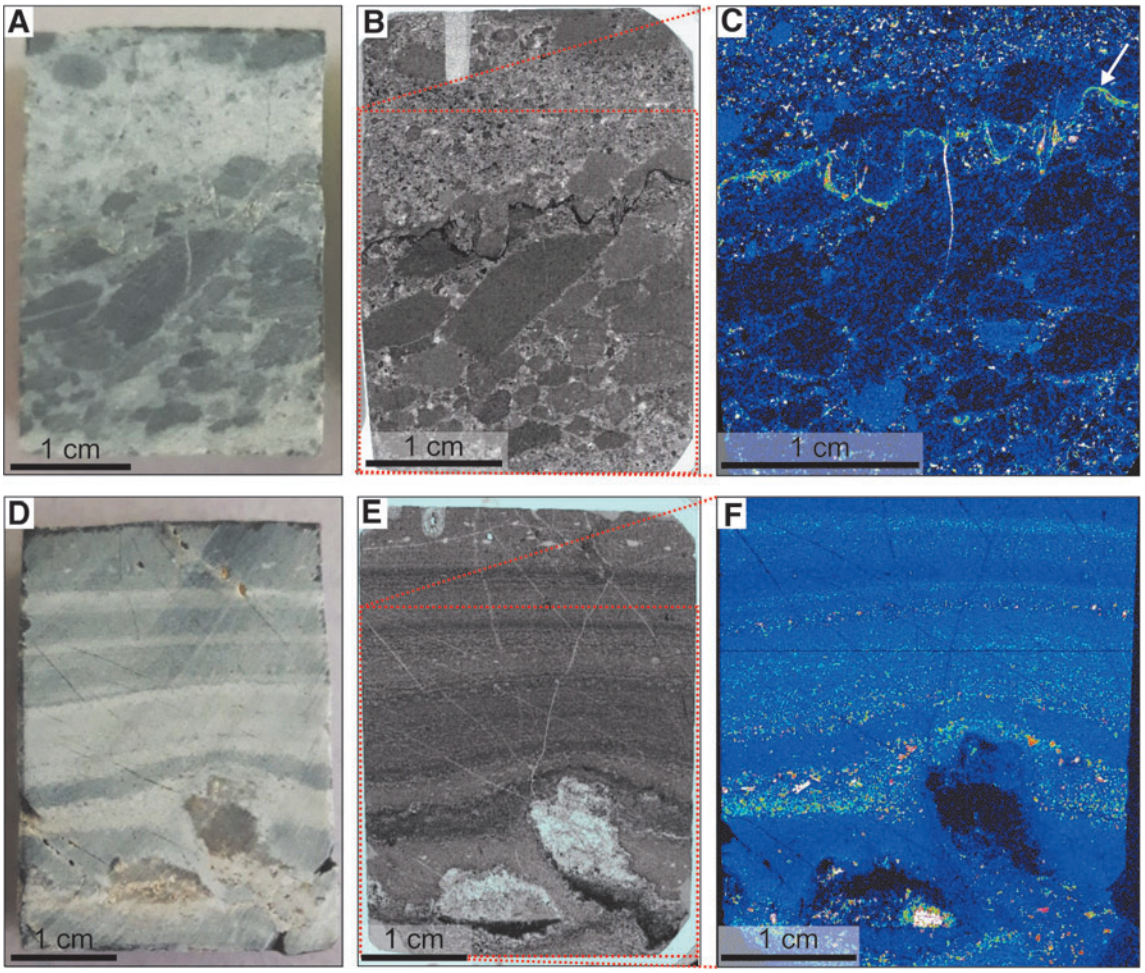

FIG. 4. **(A, D)** Photographs of the slabs from which thin sections 00AU39c and 00AU40b were prepared, respectively. **(B, E)** Image mosaics of thin sections 00AU39c and 00AU40b (Nikon Eclipse Ti microscope) with red dotted box corresponding to the images shown in **(C, F)**, respectively. Note that light gray layers observed with the naked eye in **(E)** appear darker under the optical microscope whereas dark gray layers appear brighter. **(C, F)** X-ray fluorescence spectroscopy maps of potassium showing the distribution of this element related to the alteration phases of the volcanic protoliths throughout the samples (concentration varies between low [dark blue] and high [white], with white arrow in **C** indicating a potassium-enriched horizontal stylolite).

A deposit of pumice is intercalated between a coarse-grained layer and a fine-grained layer and is composed of rounded pumice fragments ≥1 cm in size, enriched in silica. The base of the pumice is sometimes enriched in black deposits composed of crystals of anatase (Fig. 4E).

3.1.3. Mineralogical characterization. Different types of volcanic grains were observed and described by optical microscopy and Raman spectroscopy in samples 00AU39 and 00AU40 (Fig. 5 and Table 1). All volcanic grains are embedded in a mineral matrix mostly composed of silica and volcanic dust, and they have been altered and replaced by secondary alteration minerals before being almost completely silicified. Two types of alteration may affect volcanic grains. The first is morphological alteration due to corrosion and mechanical processes, causing the edges of

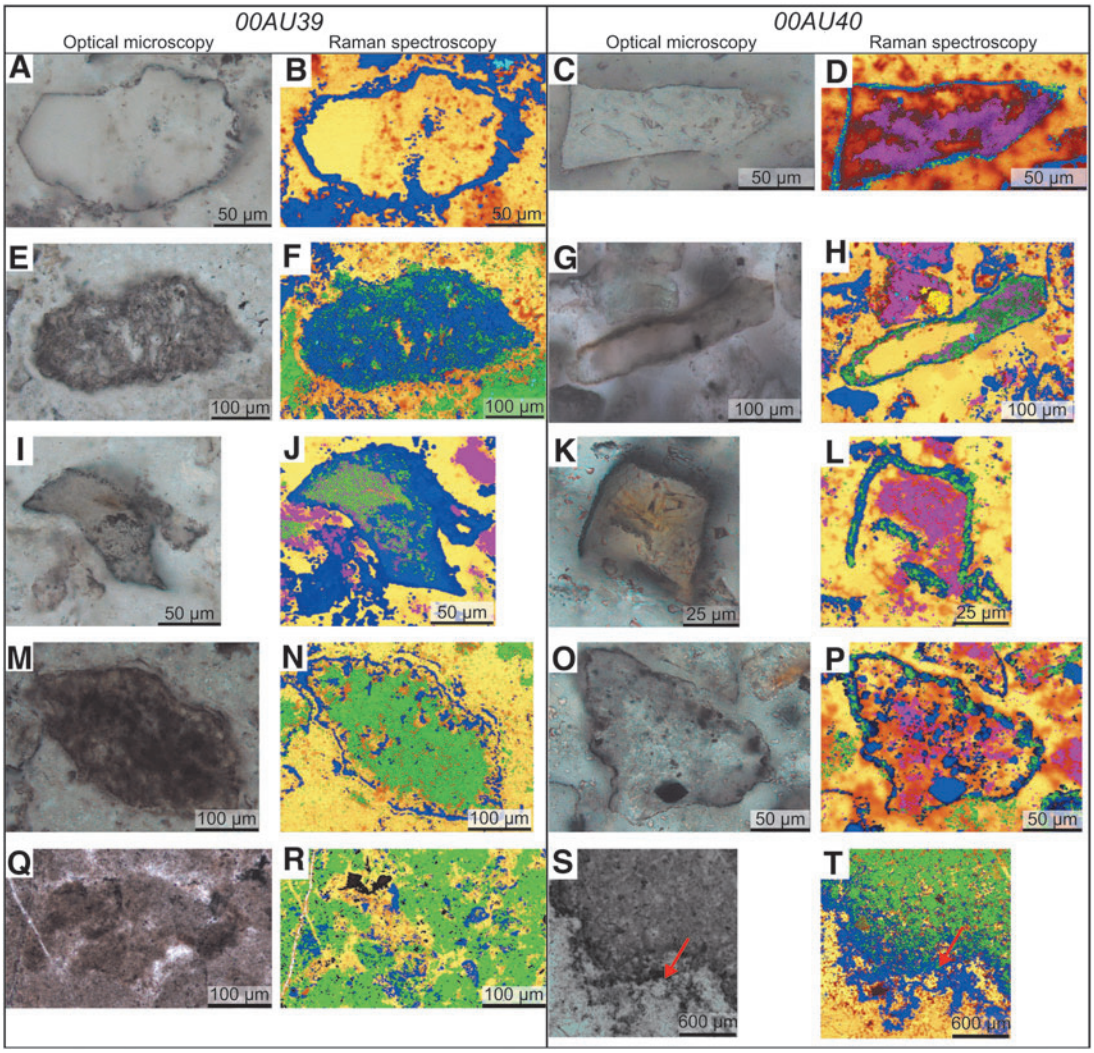

FIG. 5. Optical images showing different grain types in transmitted light (left) and in Raman maps (right) for samples 00AU39 (left column) and 00AU40 (right column). In Raman maps, yellow/orange = quartz; dark blue = anatase; light blue = rutile, fuchsia = hydromuscovite; pale yellow = tourmaline; green = CM (kerogen). **(A, B)** Light-colored volcanic glass, with angular to subrounded edges composed of anatase, and replaced by quartz. **(C, D)** Light-colored volcanic glass, with angular to subangular edges composed of anatase and a small amount of carbonaceous matter, and replaced by quartz and hydromuscovite. **(E, F)** Pumice fragment, brown in color, curved-shape and rounded edges, replaced by anatase, composed of light inclusions of quartz, and carbonaceous matter located around the edges and inside the inclusions. **(G, H)** Feldspar, yellow to orange in color, elongated rod-like habit, angular to rounded edges, surrounded by anatase and rutile, replaced by quartz and hydromuscovite, and coated with carbonaceous matter. **(I, J)** Amphibole/pyroxene, brown-green in color, high relief, angular to subrounded edges composed of anatase, replaced by hydromuscovite, and coated with anatase and carbonaceous matter. **(K, L)** Amphibole/pyroxene, light brown-orange in color, high relief, angular to subrounded edges composed of anatase and carbonaceous matter, and replaced by quartz and hydromuscovite. **(M, N)** Multiphase volcanic rock fragment coated with a dark brownish deposit and a curved-shape (corresponding to carbonaceous matter on the Raman map), and rounded edges composed of anatase. **(O, P)** Light-colored multiphase volcanic rock fragment, with rounded edges composed of anatase and carbonaceous matter, replaced by quartz and hydromuscovite, and coated with anatase. **(Q, R)** Silica-dust gel of light to dark brown in color, crossed by veins of silica, and mostly composed of quartz, anatase and carbonaceous matter. **(S, T)** Silica-dust gel of dark brown in color, underlined by anatase, and mostly composed of quartz and carbonaceous matter (a silica spherule is indicated by a red arrow). CM = carbonaceous matter.

Table 1. Summary of the Characteristics of the Different Structures Found in the Samples Using Optical Microscopy and Raman Spectroscopy

Category of volcanic grains	*Size*	*Morphology*	*Color*	*Pseudomorphs*	*Protolith*	*Other specificities*
Category 1 (Fig. 5A–D)	100–200 μm	Rectangular, angular (± rounded) edges	Light-colored (almost transparent)	Quartz ± hydromuscovite, anatase	Volcanic glass	/
Category 2 (Figs. 4E and 5E–F)	100–200 μm (close[a]) Several mm (far[a])	Curved, rounded edges	Dark brown (close) White (far)	Microcrystalline quartz ± hydromuscovite, anatase	Pumice	Light inclusions (close)
Category 3 (Fig. 5G–H)	50–200 μm (width) by several μm (length)	Tabular/ elongated, angular (± rounded) edges	Pink, white, or yellow	Hydromuscovite and/or quartz, anatase	Feldspars	May be found in pairs
Category 4 (Fig. 5I–L)	25–100 μm	Irregular, angular (± rounded) edges	Brown-green, light brown, dark brown, or bluish	Quartz and/or hydromuscovite, anatase	Amphiboles or pyroxenes	Strong relief
Category 5 (Fig. 5M–P)	Variable	Irregular or curved, rounded (rarely angular) edges	Light to dark-colored	Quartz and/or hydromuscovite, anatase	Multiphase volcanic rock fragments	/
Category 6 (Fig. 5Q–T)	<1 cm (close) Few mm (far)	Pebbles-like (close) Laminations (far)	Light to dark brown	Microcrystalline quartz	Silica-dust gel	Silica spherules (far)

[a]Close/far = sometimes we observe some differences between the sample close to the hydrothermal source and the sample far from it that are specified with a mention (close or far) in brackets.

the volcanic particles to become either embayed or more rounded, respectively. The second is mineralogical alteration, particularly pseudomorphosis, that is, mineral replacement by chemical substitution with preservation of the primary structure (appearance and dimensions). In the Kitty's Gap Chert, most volcanic clasts were diagenetically altered to clays (*e.g.*, smectite or illite) before being replaced by hydromuscovite, a metamorphic phase, and outlined by Ti-oxides (anatase and rutile).

Volcanic grains can be divided into six categories defined by their size, morphology, color, and protolithic origin. Category 1 corresponds to optically light-colored (and almost transparent) volcanic glass protoliths generally 100–200 μm in size, with a rectangular shape and often angular edges (less commonly with rounded edges; Fig. 5A–D). Category 2 comprises pumice protoliths that differ in appearance between the samples. In sample 00AU39 close to the hydrothermal source, pumice fragments are about a 100 μm in size, with a curved shape and rounded edges, dark brown in color with light inclusions composed of microcrystalline quartz, and always coated with anatase. Further from the hydrothermal source in sample 00AU40, they are of millimeter to centimeter size, with a curved shape and rounded edges, white in color, and always coated with deposits of anatase, which sometimes underline the bottom of the pumice by forming a large very dark deposit (Figs. 4E and 5E, F).

Category 3 corresponds to tabular or elongated feldspar protoliths 50–200 μm in width and >200 μm in length, with angular edges (sometimes rounded if mechanically corroded), and light colored (pink, white or yellow). They may also be associated in pairs (Fig. 5G, H). In sample 00AU40, far from the hydrothermal source, these grains are mostly found in dark gray laminations enriched in anatase. Category 4 is made of amphibole or pyroxene protoliths 25–100 μm in size, of irregular shape with often angular edges, brown-green, light brown, dark brown, or bluish in color, with a strong relief, and with an identical aspect in analyzed polarized light. Their surfaces can be completely coated with anatase (Fig. 5I–L). Category 5 are multiphase volcanic rock fragments that constitute the majority of the volcanic grains found in the samples. They probably represent volcanic rock (basaltic or rhyolitic) fragments. The multiphase volcanic rock fragments are variable in size, often of unrecognizable or curved shape with rounded structure (more rarely angular to rounded), light to dark-colored, and sometimes completely coated with anatase (Fig. 5M, P).

Category 6: In addition to the volcanic grains described earlier, a mixture of microcrystalline quartz (originally silica gel) and fine-grained volcanic dust that forms a silica-dust gel composite occurs frequently in the samples. It appears dark to the naked eye and light to dark brown under the microscope. In sample 00AU39, the silica-dust gel forms pebble-like structures (<1 cm) that are clearly distinct from the silica matrix and the volcanic clasts. In sample 00AU40, the silica-dust gel forms dark colored laminations a few millimeters thick that are distinct from light-colored laminations and have numerous siliceous spherules of volcanic origin (Fig. 5Q–T).

All the categories of grains described earlier are present in both samples, particularly in the light gray zones, except pebbles that are only found in sample 00AU39, near the main hydrothermal vein. Other minerals were also

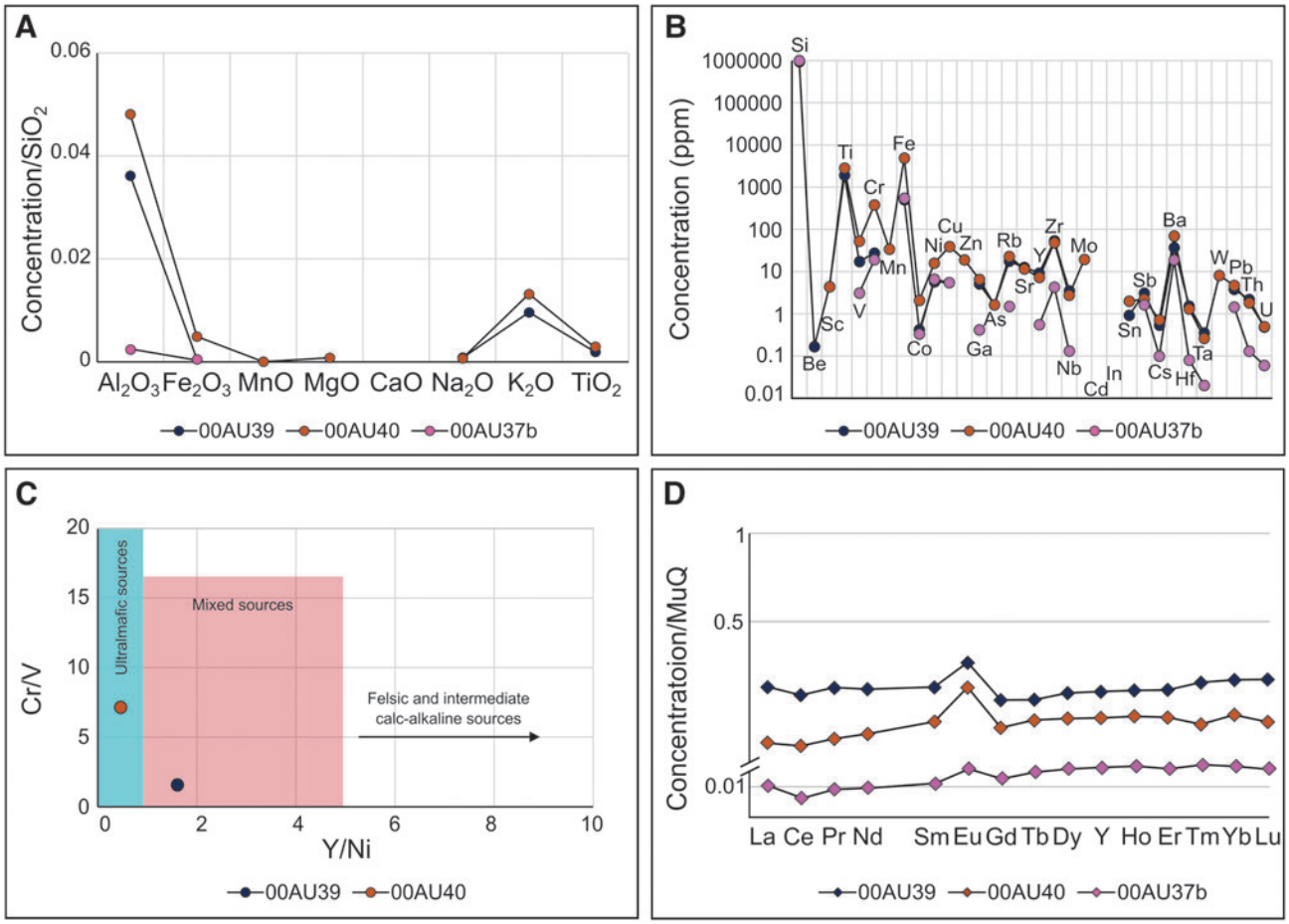

FIG. 6. **(A)** ICP-OES analyses of major element concentrations normalized to SiO_2 in bulk samples 00AU39 (blue), 00AU40 (orange), and 00AU37b (pink). **(B)** Extended ICP-MS major and trace element concentrations (ppm) of the same samples (modified after Hickman-Lewis et al., 2020b). **(C)** Bulk ICP-MS results of Cr/V versus Y/Ni for samples 00AU39 and 00AU40 (modified after Hickman-Lewis et al., 2020b). **(D)** MuQ-normalized bulk ICP-MS measurements of REE + Y in the samples. ICP-OES = inductively coupled plasma optical emission spectrometry; MS = mass spectrometry; MuQ = Mud from Queensland; REE, rare earth elements.

identified, but only one specimen of each has been found in either sample, hence not representative of most of the grains found in the chert samples. A single barite crystal was identified in sample 00AU39: it has a cubic structure with a size of $\sim 50\,\mu m^2$, slightly colored yellow, with a strong relief, two families of 90° cleavage, and a tunnel on one side, and is coated with small red and yellow pyrite grains. A tourmaline crystal was also identified in sample 00AU40, adjacent to a feldspar grain, with a size of $85 \times 125\,\mu m$, blue-green colored, and mostly altered to hydromuscovite (Fig. 5G, H).

3.1.4. Geochemical characterization. Bulk ICP-OES and ICP-MS analyses of powdered rock samples were used to estimate the bulk geochemistry of the rocks with the objective of reconstructing characteristics of the local paleoenvironment (Fig. 6 and Table 2).

The sample extracted directly from the hydrothermal vein (00AU37b) is almost pure SiO_2 (>99%), with relatively low contents of Al_2O_3 (0.26%) and Fe_2O_3 (0.05%; Fig. 6A). The other two samples (00AU39 and 00AU40) are also enriched in SiO_2 (90–95%), but have relatively higher contents of Al_2O_3 (3.6–4.8%) and K_2O (0.9–1.3%), which reflects a higher volcanogenic input, a higher degree of metasomatism (diagenetic or metamorphic process during which minerals are replaced by others following the circulation of fluids in the rock), and/or the increase in clay content and relatively low contents in Fe_2O_3 (<0.5%), TiO_2 (<0.3%), and Na_2O (<0.1%; Fig. 6A).

The extended ICP-MS major and trace element compositions of samples indicate that the silica vein is relatively poor in all elements compared with the other samples,

TABLE 2. ELEMENTAL ANOMALIES CALCULATED FROM BULK INDUCTIVELY COUPLED PLASMA-MASS SPECTROMETRY ANALYSES

Bulk	*00AU39*	*00AU40*	*00AU37b*
$(Pr/Yb)_{MuQ}$	0.93	0.80	0.54
Y/Ho	25.84	25.72	25.00
$(Ce/Ce^*)_{MuQ}$	0.92	0.98	0.81
$(Eu/Eu^*)_{MuQ}$	1.28	1.34	1.27
$(La/La^*)_{MuQ}$	0.98	1.05	1.12
$(Y/Y^*)_{MuQ}$	0.99	0.99	1.00
$(Gd/Gd^*)_{MuQ}$	0.95	0.92	0.83

MuQ = Mud from Queensland.

except for Sb and Ba, and some transition metals such as Cr, Fe, Co, Ni, and Cu that may have been supplied by hydrothermal fluids or by the degradation of basaltic rocks (Fig. 6B). The sample near the hydrothermal vein (00AU39) shows the following trend (>10 ppm): Ti>Fe>Zr>Ba> Cr>Rb, V>Sr, whereas the sample further from the source (00AU40) has (>10 ppm): Fe>Ti>Cr>Ba>Mn>V>Zr> Cu>Rb>Mo, Zn>Ni>Sr. Sample 00AU40 is particularly enriched in several transition metals, including V, Cr, Mn, Fe, Co, Ni, Cu, Zn, Mo, and W, and other metals (Sn, Ba) relative to sample 00AU39 (Fig. 6B). The bulk sample MuQ-normalized REE + Y characteristics are slightly enriched in HREE [with a low $(Pr/Yb)_{MuQ}$ ratio], indicating moderately strong seawater influence for all samples (Fig. 6D and Table 2). However, sample 00AU39 has a slightly elevated LREE concentration that resulted in a flatter signature, which indicates a more significant terrigenous input. Y/Ho ratios are sub-chondritic (Y/Ho <27) in all samples, ranging between 25.0 and 25.8.

Ce anomalies are slightly negative (0.81–0.92) in samples 00AU37b and 00AU39 and negligible (0.98) in sample 00AU40. Eu anomalies are weakly positive (1.27–1.34) in all samples. La/La^*_{MuQ}, Y/Y^*_{MuQ}, and Gd/Gd^*_{MuQ} are negligible (0.98–1.12, 0.99–1.00 and 0.92–0.95, respectively), except for the slightly negative Gd anomaly in sample 00AU37b (0.83). Plots of Cr/V against Y/Ni from bulk ICP-MS results were used to determine the chemistry of the protoliths from which the samples were derived; these indicate that sample 00AU40 is derived from the erosion of ultramafic protoliths, whereas sample 00AU39 is sourced from mixed mafic and felsic rocks (Fig. 6C).

In situ LA-ICP-MS analyses performed on samples 00AU39 and 00AU40 (Supplementary Fig. S1) indicate major element composition similar to the bulk analyses: $SiO_2>Al_2O_3>K_2O$. However, we observed that most of the areas of interest relatively enriched in SiO_2 (86–99%) are generally depleted in Al_2O_3 (<11%) and K_2O (<4%), whereas areas relatively poor in SiO_2 (55–77%) are enriched in Al_2O_3 (17–35%) and K_2O (4.5–9%); thus, the silica content is inversely proportional to the aluminum and potassium contents. *In situ* LA-ICP-MS results were also used to reconstruct the paleoenvironment conditions at a local scale using REE + Y composition (Fig. 7 and Table 3).

MuQ-normalized REE + Y characteristics of sample 00AU39 (Fig. 7A and Table 3a) vary between a high enrichment in LREE compared with HREE with high $(Pr/Yb)_{MuQ}$, which indicates a significant terrigenous input and a typical seawater pattern of HREE>LREE with low $(Pr/Yb)_{MuQ}$. Y/Ho ratios are sub-chondritic (22.3–25.6) to super-chondritic (27.0–30.1) except for a very low ratio

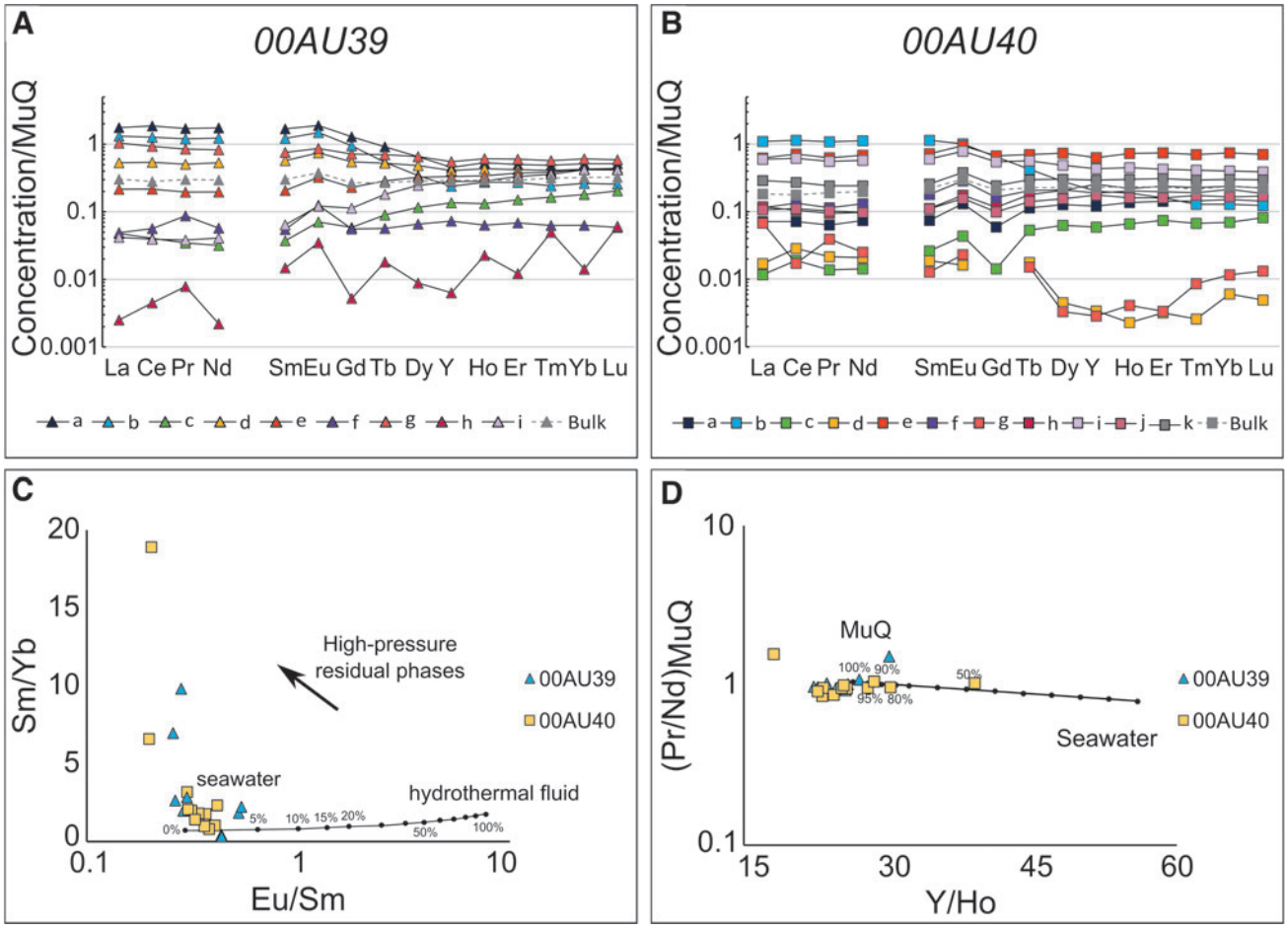

FIG. 7. **(A, B)** *In situ* LA-ICP-MS results (solid lines) compared with bulk ICP-MS (dashed lines), showing MuQ-normalized REE + Y composition in samples 00AU39 and 00AU40. **(C, D)** *In situ* LA-ICP-MS and bulk ICP-MS data plotted against the hydrothermal fluid–seawater and MuQ–seawater mixing lines. **(C, D)** are plotted after methods described in Gourcerol et al. (2016); modified after Hickman-Lewis et al. (2020b). LA = laser ablation.

Table 3. Elemental Anomalies Calculated from *In Situ* Laser Ablation-Inductively Coupled Plasma-Mass Spectrometry Analyses

	a	*B*	*c*	*d*	*e*	*f*	*g*	*h*	*i*		
(a) 00AU39											
$(Pr/Yb)_{MuQ}$	3.33	4.56	0.19	1.19	0.46	1.38	1.39	0.56	0.09		
Y/Ho	22.28	22.71	27.01	24.57	25.43	30.11	23.64	7.30	25.60		
$(Ce/Ce^*)_{MuQ}$	1.11	1.09	1.08	1.12	1.12	0.43	1.07	0.16	1.10		
$(Eu/Eu^*)_{MuQ}$	1.38	1.60	1.37	1.33	1.38	2.19	1.17	2.11	1.31		
$(La/La^*)_{MuQ}$	1.07	1.16	1.18	1.15	1.11	0.25	1.16	0.03	1.26		
$(Y/Y^*)_{MuQ}$	0.88	0.87	0.96	0.96	0.93	1.11	0.91	0.36	0.91		
$(Gd/Gd^*)_{MuQ}$	1.15	1.33	0.85	1.01	0.89	0.97	0.99	0.30	0.87		
Hydrothermal influence	0%	0%	0.75%	0.15%	0.3%	2%	0%	2.5%	0.75%		
Continental influence	100%	100%	98%	100%	100%	85%	100%	100%	100%		
	a	*b*	*c*	*d*	*e*	*f*	*g*	*h*	*i*	*j*	*k*
(b) 00AU40											
$(Pr/Yb)_{MuQ}$	0.42	8.49	0.20	3.57	0.84	0.53	3.40	0.40	1.38	0.62	0.81
Y/Ho	23.17	27.90	23.29	39.01	22.69	24.35	18.13	30.25	25.20	28.55	25.40
$(Ce/Ce^*)_{MuQ}$	1.31	1.10	1.43	1.29	1.24	1.34	0.28	1.14	1.16	1.02	1.12
$(Eu/Eu^*)_{MuQ}$	1.49	1.23	1.26	0.85	1.33	1.50	1.64	1.32	1.33	1.28	1.39
$(La/La^*)_{MuQ}$	1.52	1.09	0.91	0.74	1.18	1.32	0.70	1.32	1.16	0.93	1.19
$(Y/Y^*)_{MuQ}$	0.87	1.15	0.84	1.25	0.86	0.94	0.76	1.11	0.99	1.10	0.96
$(Gd/Gd^*)_{MuQ}$	0.59	1.09	0.33	0.00	0.94	0.81	0.00	0.75	0.94	0.74	0.85
Hydrothermal influence	0.55%	0%	0.4%	0%	0.15%	0.3%	0.7%	0.3%	0.15%	0.15%	0.25%
Continental influence	100%	95%	100%	48%	100%	100%	100%	82%	100%	92.5%	100%

(7.30) in the silica vein (h). Most areas of interest have a slight positive anomaly in Ce (1.07–1.12), whereas some (dark grain, f and silica vein, h) have a strong negative Ce anomaly (0.16–0.43). All areas of interest show a positive anomaly in Eu, ranging between 1.17 and 2.19. La/La^*_{MuQ}, Y/Y^*_{MuQ}, and Gd/Gd^*_{MuQ} range from negative to positive (0.25–1.26, 0.87–1.11, and 0.85–1.33, respectively), except the silica vein (h) with strongly La, Y, and Gd anomalies (0.03, 0.36, and 0.30, respectively).

MuQ-normalized REE + Y measurements of sample 00AU40 (Fig. 7B and Table 3b) show two types of pattern, that is, a relative enrichment in LREE relative to HREE with high $(Pr/Yb)_{MuQ}$ (continental pattern) and a relative enrichment in HREE relative to LREE with low $(Pr/Yb)_{MuQ}$ (seawater pattern). The Y/Ho ratios are sub-chondritic (18.1–25.4) to super-chondritic (27.9–39.0). Almost all areas of interest have a slight positive anomaly in Ce (1.02–1.43), but only the pumice fragment (g) has a strong negative anomaly (0.28). All areas of interest show a positive anomaly in Eu, ranging between 1.23 and 1.64, except the chalcedony layer (d) with a negative anomaly (0.84). La/La^*_{MuQ} and Y/Y^*_{MuQ} range from negative to positive (respectively, 0.70–1.52 and 0.76–1.25), but Gd/Gd^*_{MuQ} is mostly slightly negative (0.33–1.09), including the chalcedony layer (d) and the pumice fragment (g), which features no Gd anomaly.

Mixing line diagrams show that samples are slightly influenced by hydrothermal fluids (Fig. 7C) and relatively strongly by continental inputs (Fig. 7D). Sm/Yb versus Eu/Sm indicates a very low hydrothermal influence (≤2.5%) for all areas of interest. $(Pr/Nd)_{MuQ}$ versus Y/Ho suggests that the influence of seawater was greater in sample 00AU40, especially for areas (b), (j), (h), and (d) (5–52% seawater influence). Only the dark grain (f) in sample 00AU39 exhibits a greater influence of seawater (15%).

In summary, the geochemistry of the areas of interest in the rock samples is representative of very local geochemical conditions that may differ from those of the bulk sample:

- Areas of interest in samples 00AU39 and 00AU40 are either enriched in LREE compared with HREE, reflecting terrigenous inputs, or enriched in HREE compared with LREE, attributed to seawater inputs;
- Y/Ho ratios vary from sub-chondritic (<27) to super-chondritic (>27) in all samples, most of which are closer to the sub-chondritic values of bulk samples;
- Ce anomalies are slightly positive in most areas of all samples, with some areas having very strong negative Ce anomalies;
- Eu anomalies are positive in all samples;
- La and Y anomalies range from negative to positive for most of the areas in both samples, except the silica vein in 00AU39 with strongly negative La and Y anomalies;
- Gd anomalies are variable between the samples, ranging from negative to positive in sample 00AU39 (except the silica vein with strong Gd negative anomaly), and slightly negative in sample 00AU40 (including two structures without Gd anomaly).

3.2. Investigating the carbonaceous matter

In the following, we present detailed, *in situ* physical and geochemical characterization of the carbonaceous matter to further characterize the diversity of the kerogenous phase, as well as the distribution of carbonaceous matter at multiple scales (microscopic and nanoscopic scales) in the chert samples.

3.2.1. Physical characterization and distribution at the microscopic scale. Despite the small amount of organic carbon in the volcanoclastic sediments of the Kitty's Gap Chert, carbonaceous matter could be detected using Raman microspectroscopy, especially at the surface of volcanic particles and in the silica-dust gel matrix in samples 00AU39 and 00AU40 (Figs. 5 and 8A–D). The Raman spectrum of the carbonaceous matter typically shows two bands at ca. 1350 cm^{-1} and ca. 1600 cm^{-1} corresponding to the D1 (disordered) and G+D2 (graphite and disordered) bands; these characteristics are consistent with mature kerogen (Fig. 8E) (Beyssac *et al.*, 2002a, 2002b). Based on the work of Kouketsu *et al.* (2014), it is possible to estimate the maximal temperature undergone by the carbonaceous matter to about 350°C.

Nevertheless, we observed notable variations in the distribution of the carbonaceous matter, depending on the sample, the nature of the volcanic clasts, and the degree of mineralogical and/or morphological alteration. Generally, carbonaceous matter is located on volcanic clasts with rounded edges (morphological alteration) and/or replaced by mineral phases, such as hydromuscovite and anatase (mineralogical alteration). In samples 00AU39 and 00AU40, the most altered volcanic glass, pumice, feldspars, amphiboles/pyroxenes, and multiphase volcanic rock fragments are richer in carbonaceous matter, which is frequently associated with hydromuscovite and anatase on the surfaces and edges of volcanic clasts, and sometimes completely replaces the volcanic protoliths (Fig. 5E–P).

In sample 00AU40, we also observed a small amount of carbonaceous matter intermixed with hydromuscovite at the surfaces of volcanic clasts and with anatase at the edges of the less altered volcanic glass, amphiboles/pyroxenes, and multiphase volcanic rock fragments (Fig. 5C, D). Carbonaceous matter is also a ubiquitous component of the silica-dust gel matrix, where it may co-occur with crystals of anatase, rutile, and hydromuscovite (Fig. 5Q–T).

3.2.2. Physical characterization and distribution at the nanoscopic scale. The nanostructure and crystallography of the carbonaceous matter in the chert samples were studied using STEM and high-resolution (HR)-TEM analysis of 100 nm-thick FIB sections (Fig. 9 and Supplementary Figs. S2 and S3). In samples 00AU39 and 00AU40, we observed different types of structure of carbonaceous matter, including coatings around volcanic clasts (Fig. 9A), isolated spherical to elliptical particles (Fig. 9A–D), elongated structures (Fig. 9E, F), and diffuse clouds. Two degrees of crystallinity of carbonaceous matter can also be distinguished in the chert samples: amorphous (Fig. 9A, B, E, F) and crystallized (graphitized) carbonaceous matter, the latter presenting an onion-shaped structure (Fig. 9C, D).

The distribution of the carbonaceous matter varies with the protolith and alteration of the volcanic grains, but it is frequently associated with hydromuscovite (presenting a sheet-like structure with interplanar distances of ca. 10 and 20 Å, corresponding to the b and c axes of hydromuscovite,

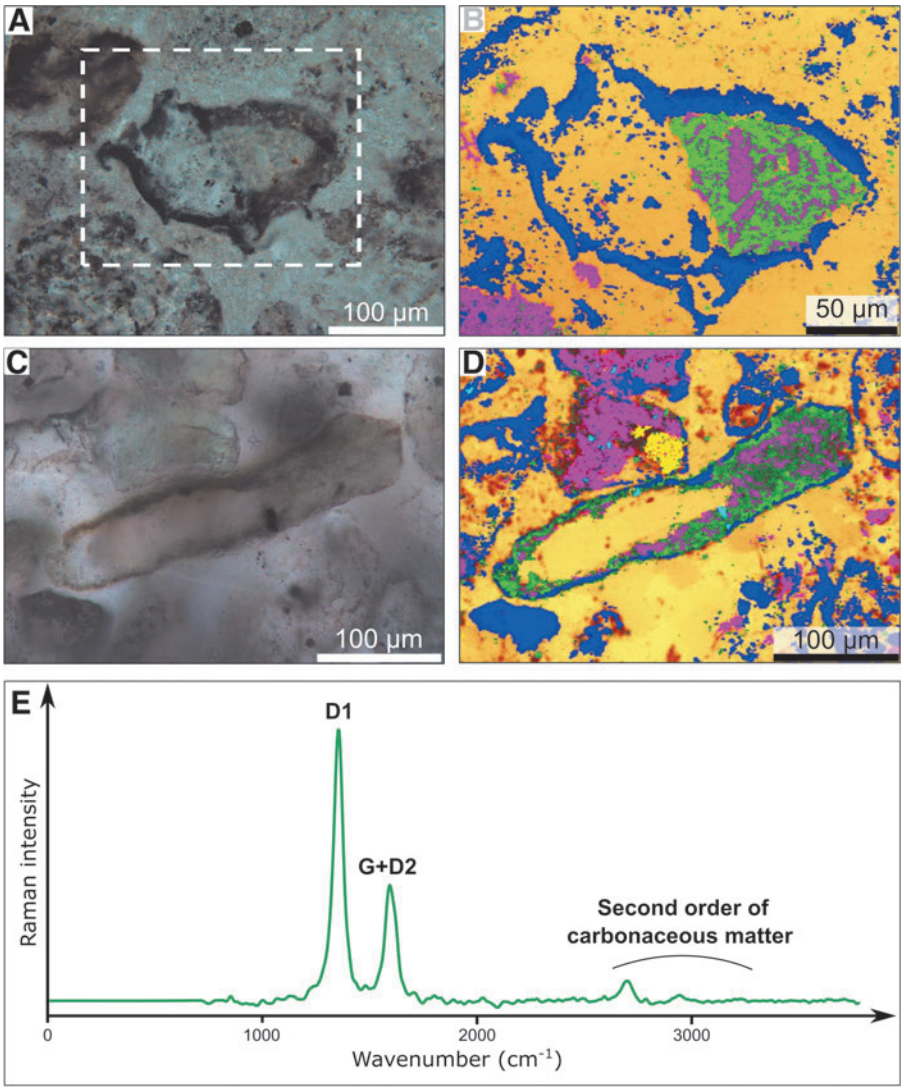

FIG. 8. Raman maps of two volcanic grains in samples 00AU39 and 00AU40, and average Raman spectrum of the CM. **(A)** Transmitted light optical image of a volcanic grain in sample 00AU39. White dashed box indicates the region for which the Raman map in **(B)** is given. **(B)** Raman compositional map of the same grain with quartz in yellow/orange, anatase in dark blue, hydromuscovite in fuchsia and CM in green. Scan size: $240 \times 180\,\mu m$. **(C)** Transmitted light optical image of a feldspar in sample 00AU40. **(D)** Raman compositional map of the same grain with quartz in yellow/orange, anatase in dark blue, rutile in light blue, hydromuscovite in fuchsia, tourmaline in pale yellow, and CM in green. Scan size: $350 \times 250\,\mu m$. **(E)** Average Raman spectrum of the CM showing the two main bands at $\sim 1350\,cm^{-1}$ (D1 band) and $\sim 1600\,cm^{-1}$ (G+D2 band). The second-order Raman signal of CM is also visible between 2500 and $3500\,cm^{-1}$.

respectively, *e.g.*, Supplementary Fig. S3F) in microcrystals of feldspars of a few micrometers in length or located at the edges of microcrystalline quartz polygons of 2–3 µm in diameter, more rarely associated with microcrystals of anatase of <1 µm in diameter at the edges of volcanic grains (Supplementary Fig. S2C, G).

In sample 00AU39, carbonaceous matter was not observed in the well-preserved, weakly altered (to hydromuscovite) volcanic glass (Fig. 5A, B). Nevertheless, it was observed to be associated with other structures in the sample, for example, in a pumice fragment (Fig. 5E, F), as coatings around microcrystals of feldspars (Supplementary Fig. S2A, E), and as diffuse clouds mixed with hydromuscovite and nanocrystals of a heavy element (possibly a transition metal element, such as zirconium; Supplementary Fig. S2B, F). It was also observed in amphibole/pyroxene (Fig. 5I, J), where it forms elongated structures (Fig. 9E), and in a more diffuse manner where it completely replaces the grain (the carbon is homogenous on the EDX map), but forming distinct particles at the edges of the grain where it appears as coatings around anatase (Supplementary Fig. S2C, G) or as inclusions in microcrystals of feldspars. The carbonaceous matter is ubiquitous in the silica-dust gel matrix (Fig. 9C and Supplementary Fig. S2D, H), located at the edges of quartz polygons (bottom right in Fig. 5E, F), and also occurs in the silica matrix surrounding volcanic protoliths as isolated particles (Fig. 9A), often coated with a thick silica crust (Fig. 9B) or as coatings around microcrystals of felspars (Fig. 9A).

In sample 00AU40, carbonaceous matter rarely occurs in association with volcanic glass, at the edges of quartz polygons (Supplementary Fig. S3A) or intermixed with anatase at the edges of volcanic glass (Supplementary Fig. S3B). Instead, the carbonaceous matter is more frequently observed with other structures in the sample, for example, in feldspar, as coatings around microcrystals of feldspars or as inclusions in microcrystals of feldspars, sometimes at the edges of quartz polygons, and in the silica-dust gel matrix, where it is mostly located at the edges of quartz polygons (Supplementary Fig. S3C), as inclusions in microcrystals of feldspars, or as coatings around microcrystals of feldspars (Fig. 9F and Supplementary Fig. S3D–F), and even as isolated particles (Fig. 9D). The silica matrix surrounding volcanic protoliths also displays some carbonaceous matter at the edges of quartz polygons or as coatings around microcrystals of feldspars.

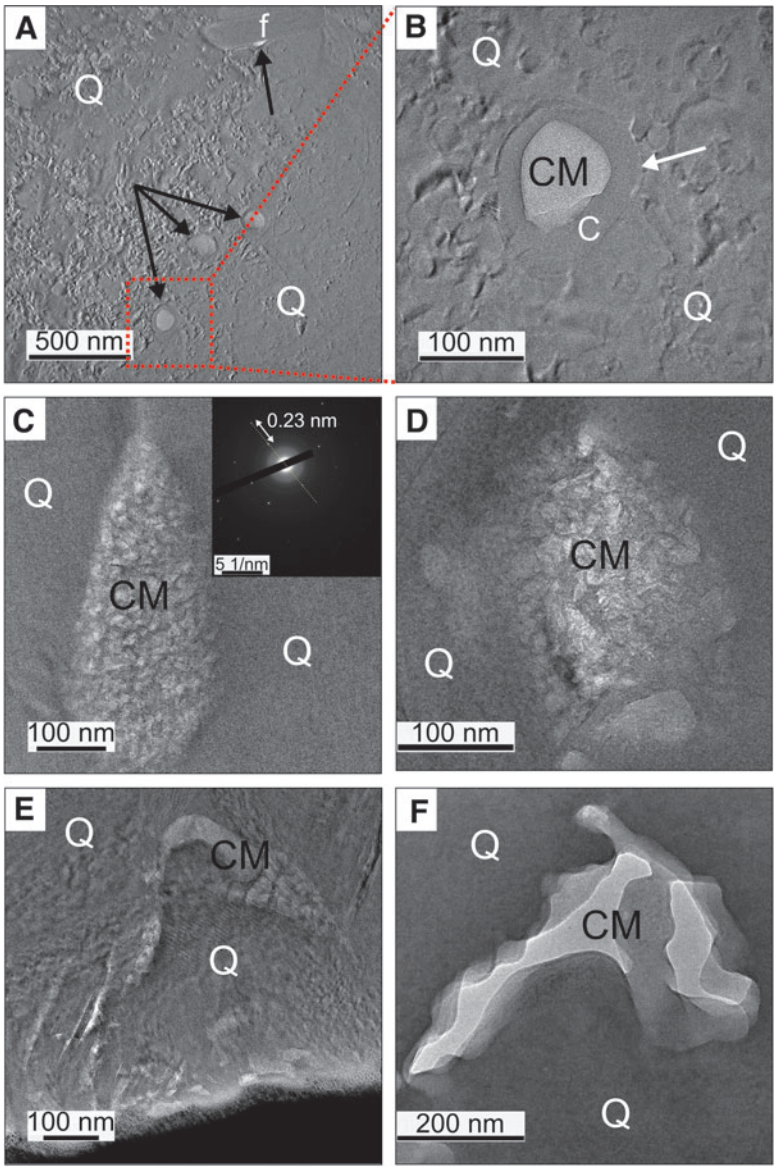

FIG. 9. HR-TEM images of FIB sections from samples 00AU39 and 00AU40. **(A)** Isolated spherical particles of CM and amorphous CM coating a microcrystal of feldspar (f) in the silica matrix of sample 00AU39, with black arrows showing the CM and red dotted box indicating the area corresponding to the image displayed in **(B)**. **(B)** Isolated spherical particle of amorphous CM surrounded by a thick silica crust (c). **(C, D)** Isolated elliptical particles of graphitized CM with an onion-shape structure in the silica-dust gel matrix of samples 00AU39 and 00AU40. Inset in **(C)** represents the diffraction pattern of graphitized CM with an interplanar distance of ~2.3 Å. The interplanar distance in the right image was determined from the plot profile command of ImageJ software and gives ~3.5 Å, corresponding to graphitized carbon (Derenne et al., 2008). **(E, F)** Elongated structures of amorphous CM in amphibole/pyroxene of sample 00AU39 and in a microcrystal of feldspar in the silica-dust gel matrix of sample 00AU40, respectively. In all images, the volcanic grains are embedded in a microcrystalline quartz (Q). FIB = focused ion beam; HR-TEM = high-resolution transmission electron microscopy.

3.2.3. Elemental composition of the carbonaceous matter. μPIXE was used to map the distribution of trace elements, in particular transition metals, associated with carbonaceous matter in several ROIs in samples 00AU39 and 00AU40 (Figs. 10 and 11 and Supplementary Figs. S4 and S5 and Supplementary Tables S2 and S3). Analyses were performed on the edges and interiors of several volcanic clasts (*e.g.*, volcanic glass, pumice, multiphase volcanic rock fragments) to provide average elemental concentrations, which were then compared within clasts and with the average elemental concentrations of the silica matrix adjacent to the clasts.

In sample 00AU39, volcanic glass (Supplementary Fig. S4A) shows significant enrichments (>150%) with respect to the adjacent silica matrix (Supplementary Fig. S4B) in seven biofunctional elements: Cl, Ca, V, Cr, Zn, As, and Sr. In addition, Fe is moderately enriched (100–150%) relative to the matrix. On the other hand, P, S, Co, Ni, and Cu are depleted (<100%) relative to the matrix. Average elemental concentrations in volcanic glass follow the trend: P>Ca>Fe>Cl>Cr>V>S>Sr>Co>*Cu*>*As*>*Zn*. Elements listed in italics were mapped and are present but at concentrations below 10 ppm, precluding their direct quantification.

The edges of volcanic glass (Supplementary Fig. S4C) exhibit significant enrichment (>150%) with respect to their interior in seven biofunctional elements: P, S, Ni, Cu, Zn, As, and Mo. Ca, Fe, Co, and Sr are moderately enriched (100–150%), whereas Cl, V, and Cr are depleted (<100%) relative to their interiors. Average elemental concentrations in the edges of volcanic glass follow the trend: P>Ca>–Fe>S>Cl>Cr>Mo>Sr>Co>Cu>*As*>*Ni*>*Zn*.

Pumice fragments (Fig. 10 and Supplementary Fig. S4A) are enriched (>150%) with respect to the matrix (Supplementary Fig. S4B) in seven biofunctional elements: Ca, Cr, Fe, Co, Ni, As, and Sr, whereas P is moderately enriched (100–150%), and S, Cl, V, Cu, Zn, and Mo are depleted (<100%). Average elemental concentrations in the pumice follow the trend: P>Ca>Fe>Cr>Cl>Co>Sr>As>*Ni*>*Mo*. The edges of the pumice (Supplementary Fig. S4C) are enriched (>150%) in P, S, and Cu, and moderately enriched (ca. 100%) in Ca, but are depleted (<100%) in Cl, Cr, Fe, Co, Ni, As, Sr, and Mo with respect to their interior. Average

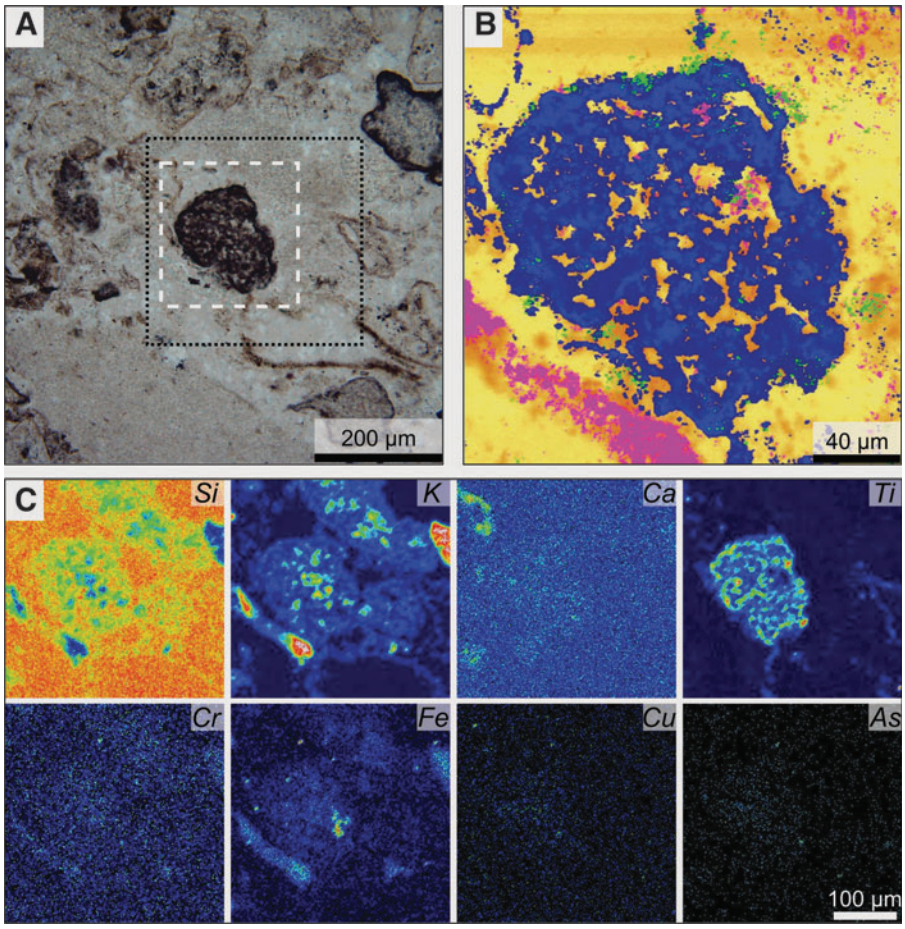

FIG. 10. Correlated optical microscopy, Raman, and µPIXE characterization of a pumice fragment in sample 00AU39. **(A)** Transmitted light optical image of a pumice fragment. White dashed box and black dotted box indicate the regions for which the Raman map in **(B)** and elemental maps in **(C)** are given, respectively. **(B)** Raman compositional map of the same grain with quartz in yellow/orange, anatase in dark blue, hydromuscovite in fuchsia, and CM in green. Scan size: 200 × 210 µm. **(C)** Elemental maps corresponding to elemental enrichments in the pumice and additional adjacent volcanic clasts. Scan size of the area analyzed with PIXE: 350 × 350 µm (black = low concentration, white = high concentration). µPIXE = microscale proton-induced X-ray emission.

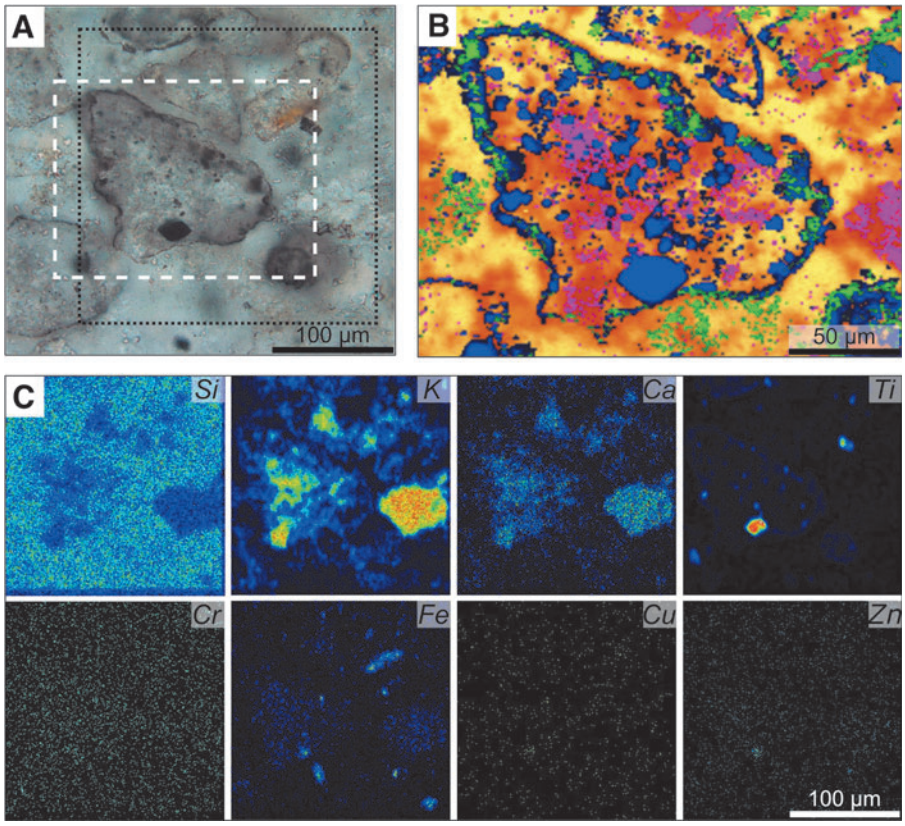

FIG. 11. Correlated optical microscopy, Raman and µPIXE characterization of a multiphase volcanic rock fragment in sample 00AU40. **(A)** Transmitted light optical image of a multiphase volcanic rock fragment. White dashed box and black dotted box indicate the regions for which the Raman map in **(B)** and elemental maps in **(C)** are given, respectively. **(B)** Raman compositional map of the same grain with quartz in yellow/orange, anatase in dark blue, hydromuscovite in fuchsia, and CM in green. Scan size: 220 × 160 µm. **(C)** Elemental maps corresponding to elemental enrichments in the multiphase volcanic rock fragment and additional adjacent volcanic clasts. Scan size of the area analyzed with PIXE: 200 × 200 µm (black = low concentration, white = high concentration).

elemental concentrations in the edges of the pumice follow the trend: P>Ca>Fe>S>Cr>Co>Sr>*As*>*Cu*.

Multiphase volcanic rock fragments poorly coated with carbonaceous matter (Supplementary Fig. S4A) exhibit significant enrichment (>150%) with respect to the matrix (Supplementary Fig. S4B) in 12 biofunctional elements: P, S, Cl, Ca, V, Cr, Fe, Co, Zn, As, Sr, and Mo, whereas Ni and Cu are depleted (<100%). Average elemental concentrations in these volcanic clasts follow the trend: P>Ca>–Fe>S>Cr>V>Cl>Sr>Co>Zn>*Mo*>*As*, *Cu*. The edges of these volcanic clasts (Supplementary Fig. S4C) are enriched (>150%) in Cl, Ni, and Mo, and moderately enriched (100–150%) in Cr, Fe, and Cu, but are depleted (<100%) in P, S, Ca, V, Co, Zn, As, and Sr with respect to their interior. Average elemental concentrations in the edges of these volcanic clasts follow the trend: P>Fe>Ca>Cr>Cl>S>Co>–Mo>Sr>*Ni*, *Cu*>*As*>*Zn*.

Multiphase volcanic rock fragments well coated with carbonaceous matter (Supplementary Fig. S4A) are significantly enriched (>150%) with respect to the matrix (Supplementary Fig. S4B) in seven biofunctional elements: S, V, Cr, Fe, As, Sr, and Mo. In addition, P and Co are moderately enriched (100–150%), whereas Ca, Cu, and Zn are depleted (<100%). Average elemental concentrations in these volcanic clasts follow the trend: Fe>P>Ca>S>V>Cr>–Mo>Sr>Zn>Co>As. The edges of these volcanic clasts (Supplementary Fig. S4C) are enriched (>150%) in P, Cr, Co, and Cu, and moderately enriched (100–150%) in Mo but are depleted (<100%) in S, Ca, V, Fe, Zn, As, and Sr with respect to their interior. Average elemental concentrations in the edges of these volcanic clasts follow the trend: P>Fe>Ca>S>Cr>Mo>Co>As>*Zn*>*Cu*.

The silica-dust gel matrix was also analyzed and shows significant enrichment with respect to the average elemental concentrations in the matrix (>150%) in eight biofunctional elements: S, Cl, Ca, Cr, Ni, Cu, Zn, and As, whereas P, Fe, and Co are moderately enriched (100–150%), and V, Sr, and Mo are depleted (<100%). Average elemental concentrations in the silica-dust gel matrix follow the trend: P>Ca>Fe>S>Cl>Cr>Cu>Zn>Co>Ni>Sr>*As*>*Mo*.

In sample 00AU40, volcanic glass (Supplementary Fig. S5A) shows significant enrichment (>150%) with respect to the adjacent silica matrix (Supplementary Fig. S5B) in eight biofunctional elements: S, Ca, V, Cr, Fe, Co, As, and Sr. In addition, Cu and Zn are moderately enriched (100–150%) relative to the matrix. On the other hand, P and Ni are depleted (<100%) relative to the matrix. Average elemental concentrations in volcanic glass follow the trend: Fe>Ca>S>V>Cr>Sr>Co>*Zn*, *Cu*>*As*. The edges of volcanic glass (Supplementary Fig. S5C) exhibit significant enrichment (>150%) with respect to their interior in only two biofunctional elements: Cu and Zn. Co and As are moderately enriched (100–150%), whereas S, Ca, V, Cr, Fe, and Sr are depleted (<100%) relative to their interiors. Average elemental concentrations in the edges of volcanic glass follow the trend: Fe>Ca>Cr>Sr>Co>Cu>Zn>*As*.

Multiphase volcanic rock fragments poorly coated with carbonaceous matter (Fig. 11 and Supplementary Fig. S5A) exhibit significant enrichments (>150%) with respect to the matrix (Supplementary Fig. S5B) in seven biofunctional elements: Ca, V, Cr, Fe, Zn, Sr, and Mo. In addition, S is moderately enriched (100–150%), whereas P, Co, Ni, Cu, and As are depleted (<100%). Average elemental concentrations in these volcanic clasts follow the trend: Fe>–Ca>V>S>Sr>Cr>Mo>Zn>Co>*Cu*>*Ni*. The edges of these volcanic clasts (Supplementary Fig. S5C) are enriched (>150%) in P and Ni, and moderately enriched (100–150%) in Cu, whereas S, Ca, V, Cr, Fe, Co, Zn, and Sr are depleted (<100%) with respect to their interior. Average elemental concentrations in the edges of these volcanic clasts follow the trend: P>Fe>Ca>V>Cr>Sr>Ni>*Co*, *Cu*>*Zn*.

Multiphase volcanic rock fragments well coated with carbonaceous matter (Supplementary Fig. S5A) are significantly enriched (>150%) with respect to the matrix (Supplementary Fig. S5B) in six biofunctional elements: P, Ca, V, Fe, Cu, and Zn. In addition, Co and As are moderately enriched (100–150%), whereas Sr is depleted (<100%). Average elemental concentrations in these volcanic clasts follow the trend: P>Fe>Ca>V>Cu>Co>Zn>*As*.

3.2.4. Molecular composition of the carbonaceous matter. DUV fluorescence microimaging (Telemos) and microspectroscopy (Polypheme) were used to identify and map aromatic compounds and minerals in ROIs in samples 00AU39 and 00AU40 (Figs. 12 and 13 and Supplementary Fig. S6). Microimaging of sample 00AU39 (Supplementary Fig. S6A, B) documents heterogeneity in aromatic compounds (spectral range from 329 to 351 nm), aromatic compounds mixed with hydromuscovite (352–388 nm), and anatase (420 to 480 nm); specifically, aromatic compounds are often spatially correlated with hydromuscovite. Spectral images (Fig. 12) confirmed the presence of aromatic compounds with main fluorescent emissions at 310 and 340 nm (Fig. 12B, C) (Ménez *et al.*, 2018).

In particular, the volcanic dust-rich matrix is slightly-to-highly enriched in aromatics exhibiting two bands at 310 and 340 nm or 340 and 360 nm (the band at 340 nm is generally more prevalent). For the other structures of interest in the sample, we observed variations in the relative concentrations of aromatics and the positions of their main bands: volcanic glass is relatively enriched in aromatics with two bands at 310 and 340 nm (Fig. 12B); amphibole/pyroxene is slightly enriched with only one band at 345 nm; some multiphase volcanic rock fragments show a high enrichment with two bands at 310 and 340 nm, whereas other multiphase volcanic rock fragments are not particularly enriched in aromatics. Other fluorescent signals have also been detected in the sample, including a major band at 415–420 nm with shoulders at 430–435 and 460–465 nm (Fig. 12B–D); these features correspond to mineral phases, in particular hydromuscovite and anatase (Gaft *et al.*, 2015).

Microimaging of sample 00AU40 (Supplementary Fig. S6C, D) shows a wider variety in aromatic compounds (spectral ranges from 329 to 351 nm), aromatic compounds mixed with hydromuscovite (352–388 nm), aromatic compounds mixed with hydromuscovite and anatase (spectral ranges from 412 to 438 nm, and from 420 to 480 nm), and anatase mixed with other metallic oxides (499–529 nm); again, aromatic compounds are often correlated with hydromuscovite. Spectral images (Fig. 13) clearly indicate the presence of aromatic compounds with one main fluorescent emission at 340–345 nm (Fig. 13B, C) (Ménez *et al.*, 2018). In particular, disseminated volcanic particles in the silica

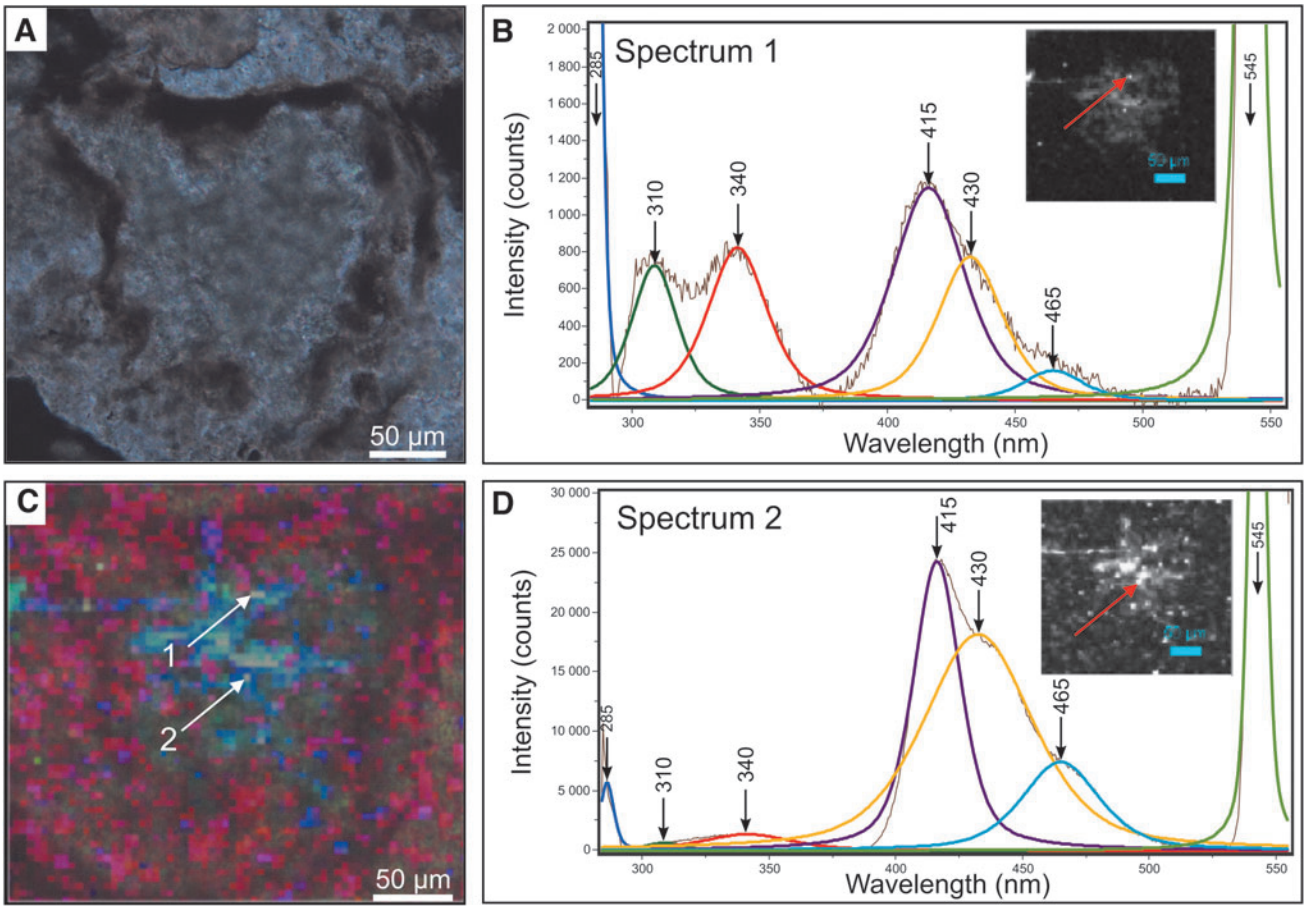

FIG. 12. DUV fluorescence map and spectra within a volcanic glass particle in sample 00AU39. **(A)** Transmitted light optical image of volcanic glass altered to anatase at the edges (brown color) and hydromuscovite in the interior (gray color). **(B)** Spectrum of aromatic compounds (main bands at 310 and 340 nm) mixed with mineral phases (main bands at 415, 430, and 465 nm); inset shows a map corresponding to the fluorescent emission at 340 nm. **(C)** RGB composite (red = 300–320 nm, green = 325–370, blue = 375–450 nm). White arrows indicate the pixels from which the spectra shown in **(B, D)** have been extracted. Scan size: 290 × 265 µm. **(D)** Spectrum of mineral phases (main bands at 415, 430, and 465 nm); inset shows a map corresponding to the fluorescent emission at 415 nm. DUV = deep-ultraviolet.

matrix are slightly to highly enriched in aromatics with a band at 340–345 nm (or sometimes two bands at 310 and 340 nm).

Some variation in the relative concentrations of aromatics and the positions of their main bands is observed in the other structures: some multiphase volcanic rock fragments are moderately to strongly enriched in aromatics with a band at 340 nm (Fig. 13B), whereas the silica-dust gel matrix often shows a high enrichment in aromatics with either one band at 340–345 nm with a shoulder at 325 nm or two bands at 310 and 340–345 nm (the band at 340–345 nm is generally more intense). Other fluorescent signals have also been detected in the sample, including a main band at 410–415 nm (Fig. 13B), with rare shoulders at 390 and 430 nm, corresponding to mineral phases, in particular hydromuscovite and anatase (Gaft *et al.*, 2015).

Transmission FTIR mapping and spectra were used to further characterize the molecular composition of the carbonaceous matter in samples 00AU39 and 00AU40, focusing on the aliphatic C–H stretching compounds within the wavenumber range 2800–3040 cm^{-1}, and the aromatic/alkenic compounds within the wavenumber range 1300–1800 cm^{-1} (Figs. 14 and 15 and Supplementary Figs. S7 and S8 and Supplementary Table S4). In the aliphatic C–H stretching region (2800–3040 cm^{-1}; Fig. 14), both samples exhibit bands at 2855 cm^{-1} (symmetrical CH_2 stretching), 2870 cm^{-1} (symmetrical CH_3 stretching), 2925 cm^{-1} (asymmetrical methylene CH_2 stretching), and 2960 cm^{-1} (asymmetrical end-methyl CH_3 stretching). Sample 00AU40 shows more intense absorbance (two to five orders of magnitude) in the aliphatic C-H stretching region with respect to sample 00AU39. In the aromatic/alkenic region (1300–1800 cm^{-1}; Supplementary Fig. S8), both samples exhibit a weak band at 1360 cm^{-1} (CH_3); weak bands at 1440 and 1470 cm^{-1} (C–H stretching with a contribution from aromatic ring stretching); a weak band at 1545 cm^{-1} (potential C–H and N–H in amide II); weak bands at 1650 cm^{-1} (highly conjugated C = O), 1705 cm^{-1} (C = O and COOH), 1720 cm^{-1} (C = O and COOH; >C = O ester stretch), and 1735 cm^{-1} (>C = O ester stretch) attributed to carbonyl and carboxyl groups; and intense bands at 1495, 1525, 1610, 1680, 1795, and 1875 cm^{-1} interpreted as Si–O. The intensity and diversity of bands in the aromatic/alkenic region is higher in sample 00AU39 with respect to sample 00AU40.

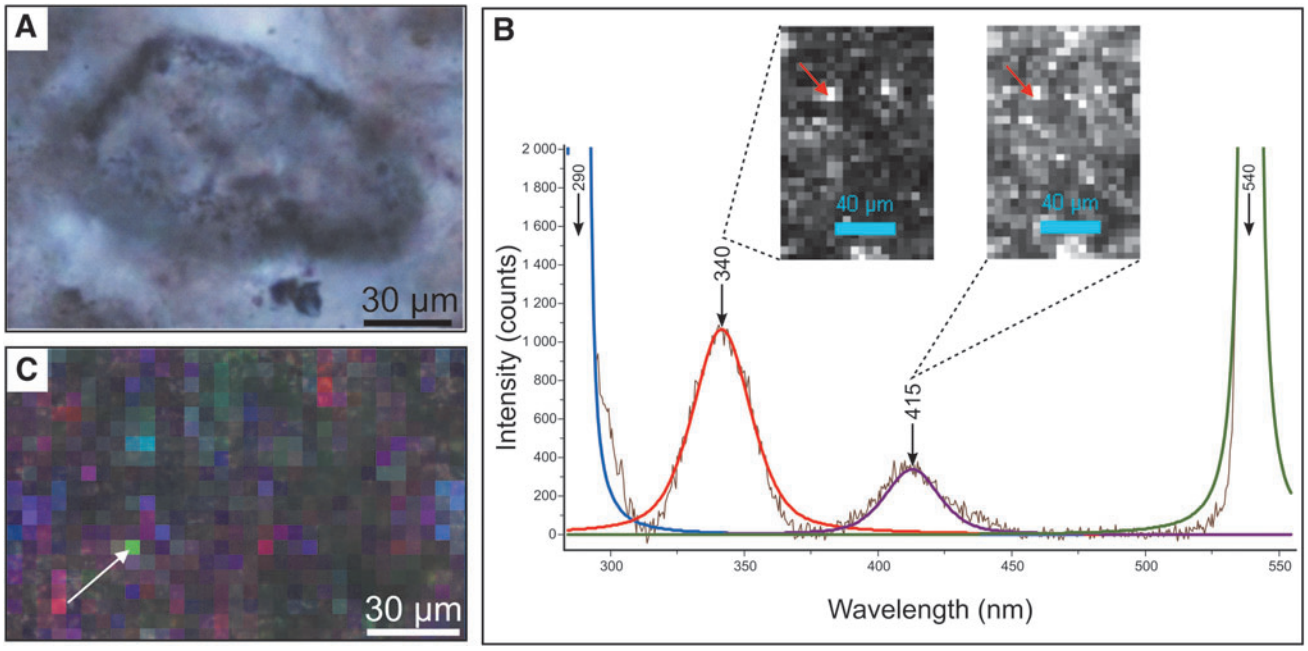

FIG. 13. DUV fluorescence map and spectrum within a multiphase volcanic rock fragment in sample 00AU40. **(A)** Transmitted light optical image of a multiphase volcanic rock fragment altered to anatase at the edges (dark color). **(B)** Spectrum of aromatic compounds (main band at 340 nm) and mineral phases (main band at 415 nm); inset shows maps corresponding to the fluorescent emissions at 340 and 415 nm, respectively. **(C)** RGB composite (red = 300–320 nm, green = 325–370, blue = 375–450 nm). White arrow indicates the pixel from which the spectrum shown in **(B)** and has been extracted. Scan size: 150 × 95 µm.

FTIR maps illustrating the distribution of organics and minerals in both samples are shown in Fig. 15. In sample 00AU39, volcanic glass is rich in hydromuscovite (–OH), with some aromatics (C–H) located in the heart of the grain. Multiphase rock fragments (Fig. 15A–L) show slight spatial and spectral variations: generally, they contain high concentrations in aromatics (C–H; Fig. 15C, D), and variable concentrations in aliphatics (CH_2 and CH_3; Fig. 15J, K) and other functional groups (C = O, COOH…; Fig. 15G–I), which are mainly concentrated in the heart of the grains. Most of the grains are silicified (Si–O; Fig. 15E, F) and show evidence of alteration to hydromuscovite (represented by proxy as –OH; Fig. 15L).

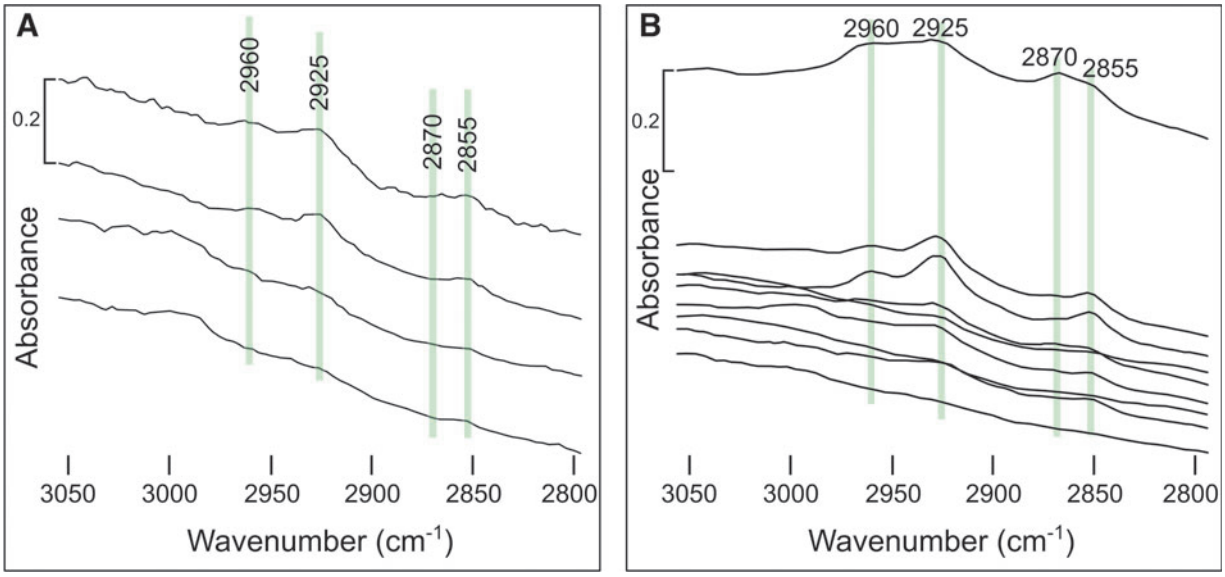

FIG. 14. Transmission FTIR absorbance spectra in the range 2800–3050 cm^{-1}. **(A)** Transmission FTIR absorbance spectra of four volcanic grains coated with CM in sample 00AU39. **(B)** Transmission FTIR absorbance spectra of five volcanic grains coated with CM (including two spectra extracted from the same two grains) and of the silica-dust gel matrix (the lowermost spectrum, characterized by the weakest absorbance and an absence of spectral features) in sample 00AU40. FTIR = Fourier transform infrared.

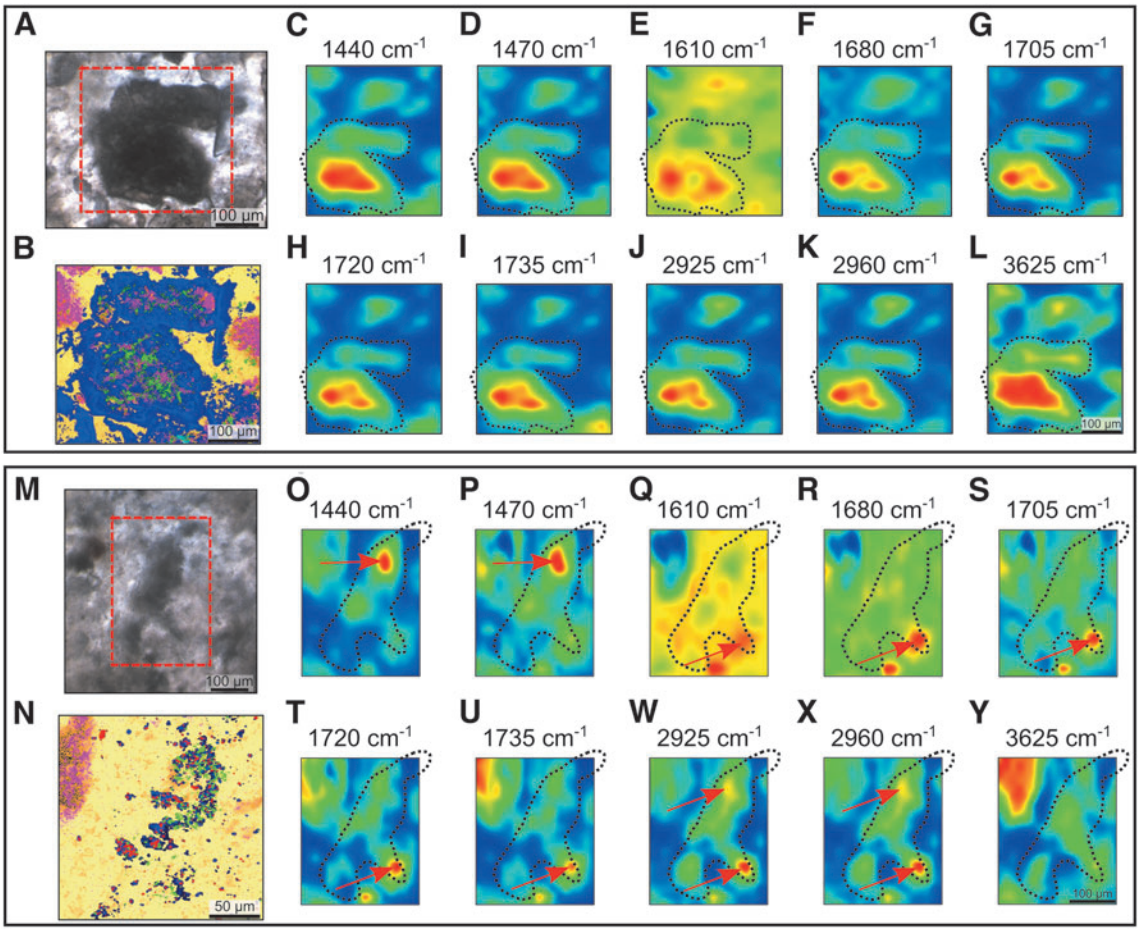

FIG. 15. FTIR microspectroscopy of diverse compounds extracted from specific bands in spectra from samples 00AU39 and 00AU40. **(A, M)** Transmitted light photomicrographs and **(B, N)** Raman compositional maps of two multiphase volcanic rock fragments in samples 00AU39 and 00AU40, respectively, with quartz in yellow, anatase in dark blue, rutile in light blue/red, hydromuscovite in fuchsia, and CM in green and red dashed box indicating the region for which the FTIR maps are given. Scan sizes of Raman maps: 400 × 350 µm and 200 × 200 µm for samples 00AU39 and 00AU40, respectively. FTIR maps of **(C, D, O, P)** C–H stretching with a contribution from aromatic ring stretching with main bands at 1440 and 1470 cm^{-1}; **(E, F, Q, R)** Si–O with main bands at 1610 and 1680 cm^{-1}; **(G, H, I, S, T, U)** carbonyl and carboxyl groups with main bands at 1705 (C = O, COOH), 1720 (C = O, COOH; >C = O ester) and 1735 cm^{-1} (>C = O ester stretch); **(J, K, W, X)** aliphatic C–H stretching with main bands at 2925 (asymmetrical methylene CH_2 stretching) and 2960 cm^{-1} (asymmetrical end-methyl CH_3 stretching); **(L, Y)** –OH with a main peak at 3625 cm^{-1}. Scan sizes of the areas analyzed with FTIR: 360 × 340 µm and 270 × 300 µm for samples 00AU39 and 00AU40 (dark blue = low concentration, red = high concentration).

In sample 00AU40, volcanic glass is very rich in –OH, rich in C–H, with some aliphatics, but shows a lesser concentration of certain functional groups (especially the >C = O ester stretch), which are instead relatively concentrated in the adjacent matrix. Multiphase rock fragments (Fig. 15M–Y) present more variations according to their nature and/or their degree of alteration: some grains are particularly rich in aromatics, especially at their edges, whereas others have interiors richer in aromatics (or more sporadically throughout the grains; Fig. 15O, P). Some grains are relatively rich in aliphatics (Fig. 15W, X), and other functional groups (Fig. 15S–U), which are either mostly concentrated in the interior of the grains or more sporadically distributed throughout. Some grains are highly silicified (Fig. 15Q, R), whereas others are silica-poor; and their –OH concentration (as a proxy for phyllosilicates) is variable (Fig. 15Y). The silica-dust gel matrix is enriched in –OH and Si–O, with some areas exhibiting increased concentrations of aromatics, aliphatics, and/or other functional groups.

In summary, chemical analyses demonstrate that the organic compositions differ between samples 00AU39 and 00AU40:

- Based on PIXE results, volcanic clasts in sample 00AU39 are enriched in 11 biofunctional elements relative to the adjacent silica matrix, in particular in Cr>>As>S>Fe>V>Sr>Ca>Cl>Co>Mo>P, whereas most of the volcanic clasts in sample 00AU40 are enriched in 7 biofunctional elements relative to the adjacent silica matrix, in particular in V>>Zn>Cr>S>Ca>Fe>As.
- Most of the edges of volcanic clasts in sample 00AU39 are enriched in 4 biofunctional elements relative to

their interior, in particular in Cu>>S>Ni>Mo, except the edges of volcanic glass, which are enriched in 11 biofunctional elements; in contrast, most of the edges of the volcanic clasts in sample 00AU40 are enriched in only 3 biofunctional elements relative to their interior, in particular in P>>Ni>Cu.

- The silica-dust gel matrix in sample 00AU39 is enriched in 11 biofunctional elements relative to the average matrix, in particular in Ni>As>Zn>Cl>Cr>Cu>S>Ca>P>Fe>Co.
- The carbonaceous matter in the samples comprises both aromatic and aliphatic functional groups:
  - In Raman spectroscopy, the signal of carbonaceous matter displays a large disorder band.
  - In DUV fluorescence, aromatic compounds were detected based on signals at 310 and 340 nm in sample 00AU39, but only at 340–345 nm in sample 00AU40;
  - In FTIR, absorbance features consistent with aromatic compounds at 1360 cm^{-1} (CH_3); 1440 and 1470 cm^{-1} (C–H stretching); 1545 cm^{-1} (C–H and N–H in amide II); 1650, 1705, 1720, and 1735 cm^{-1} (carbonyl and carboxyl groups) were identified in both samples, but the intensity and diversity of the bands are higher in sample 00AU39;
  - In FTIR, aliphatics were identified at 2855 cm^{-1} (symmetrical CH_2), 2870 cm^{-1} (symmetrical CH_3; very weak intensity), 2925 cm^{-1} (asymmetrical CH_2), and 2960 cm^{-1} (asymmetrical CH_2) in both samples, but the intensity of the bands is higher in sample 00AU40 (two to five orders of magnitude more intense);
  - FTIR analysis of volcanic glass in sample 00AU39 contains –OH associated with some aromatics, whereas the volcanic glass in sample 00AU40 is more enriched in –OH associated with more aromatics (C–H) and some aliphatics, but little enriched in certain functional groups (in particular, the >C=O ester stretch);
  - FTIR analysis of multiphase volcanic rock fragments in sample 00AU39 contain high concentrations of aromatics and variable concentrations of aliphatics and other functional groups (*e.g.*, C=O, COOH) that are mainly located in the interior of particles, whereas volcanic rock fragments in sample 00AU40 contain variable concentrations of aromatics, aliphatics, and other functional groups that are located either at the edges or in the interior of particles;
  - FTIR analysis of the silica-dust gel matrix in sample 00AU40 shows that it is particularly rich in –OH and Si–O with some heterogeneously distributed aromatics, aliphatics, and other functional groups.
- In DUV, signals attributed to mineral phases (in particular, hydromuscovite and anatase) were also detected at 415–420 nm with shoulders at 430–435 and 460–465 nm in sample 00AU39, whereas they are detected at 410–415 nm with rare shoulders at 390 and 430 nm in sample 00AU40.

4. Discussion

4.1. Paleoenvironmental reconstruction

Documentation of the paleodepositional environment of the silicified volcanic sediments of the Kitty's Gap Chert through sedimentology, petrology, mineralogy, and geochemistry is of crucial importance in demonstrating habitability for microbial life (Table 4 and Supplementary Table S1). Contextualizing the regional and local paleoenvironment of potential biosignatures is a key first step to establishing their syngenicity and biogenicity and may be used to evaluate the eventual influence of early diagenesis on biosignature preservation potential (Brasier *et al.*, 2002).

Field observations, microscopic and spectroscopic analyses, and bulk and *in situ* geochemical data indicate that the environment of deposition was a volcano-sedimentary basin (de Vries, 2004; Westall *et al.*, 2006, 2011; de Vries *et al.*, 2010) dominated by the influence of seawater and, to a lesser extent, by hydrothermalism (Orberger *et al.*, 2006). The samples were extracted from a sedimentary lens characteristic of well-developed channel-filling features and lateral accretionary bedding indicative of regular flooding and sand deposition (Figs. 1D and 2) (de Vries, 2004; de Vries *et al.*, 2010). Primary sedimentary structures observed throughout the sedimentary lens, in particular micro-ripples, flaser-linsen bedding, and undulating lamination occurring at the top (of which the chert sample 00AU40 is part), reflect the deposition of sediments under shallow water conditions, in a channel environment influenced by tides (Fig. 2D) (de Vries, 2004; Westall *et al.*, 2006; de Vries *et al.*, 2010).

Despite their similar microlithic textures, samples 00AU39 and 00AU40 exhibit different sedimentary structures. Sample 00AU39 from close to the hydrothermal vein comprises homogenous dark pebbles of fine volcanic dust (<20 μm) mixed with silica, surrounded by a coarse-grained material consisting of poorly sorted volcanic particles (50–500 μm; Fig. 4A, B). The pebbles were probably eroded from a chemical deposit of lightly consolidated silica gel and volcanic dust by more energetic conditions (waves, tides, or the injection of hydrothermal fluids and gases connected to the active volcanic system) during the deposition of the lower layers of the sediments (de Vries *et al.*, 2010; Cas *et al.*, 2011). Sample 00AU40, taken from an overlying sedimentary layer further away from the hydrothermal system, exhibits a lower part with cross- and flaser-linsen bedding indicating wave and tidal reworking. This is separated by an intraformational erosional horizon composed of centimeter-size pumice fragments reflecting explosive volcanism from overlying parallel laminations of sandy ash fall, alternating with layers of fine volcanic dust mixed with silica gel that formed in a dynamically quiet environment (Fig. 4D, E) (Westall *et al.*, 2006, 2011).

The Kitty's Gap Chert was influenced by hydrothermal activity, as indicated by micro- to macro-scale veining and brecciation (Figs. 3 and 4). The hydrothermal vein of sample 00AU37b shows a smooth, glassy texture where millimeter light veins are composed of microcrystalline quartz and cross a homogenous black chert matrix (Fig. 3). Silica veins in sample 00AU39 are composed of coarse-grained quartz and are lined with flakes of sericite, a very fine-grained variety of muscovite that is a secondary alteration mineral that forms under slightly acidic conditions (Orberger *et al.*, 2006).

The compositions of the protoliths (volcanic glass, pumice, feldspars, amphiboles, etc.) are interpreted to reflect the erosion of the underlying and surrounding volcanic rocks and ashfall, as well as their rapid alteration to

Table 4. Summary of the Characteristics of the Depositional Paleoenvironment of the Silicified Volcanic Sediments of the Kitty's Gap Chert

	00AU39 (close to hydrothermal vein, lowermost sedimentary layer)	*00AU40 (further from hydrothermal vein, overlying sedimentary layer)*
Sedimentology (field observations)	• Silicified volcanoclastic sediments located in a lenticular structure • Conglomerate composed of fine dark pebbles in a sandy matrix	• Silicified volcanoclastic sediments located in a lenticular structure • Heterolithic chert composed of finer dark and coarser light laminations • Sedimentary structures such as micro-ripples and flaser-linsen bedding typical of a shallow water, channel environment influenced by tides
Petrology (macroscopic, optical and XRF)	• Volcanic protoliths (volcanic glass, feldspar, biotite…) embedded in a microlithic matrix • Homogeneous dark pebbles composed of fine dust particles <20 μm in size mixed with silica and rare protoliths, surrounded by light-colored sandy material composed of volcanic protoliths of 50–500 μm in size replaced by silica and hydromuscovite • Silica veins from <100 μm up to a few millimeters crossing the chert sample, and consisting of coarse-grained quartz and flakes of sericite lining the veins	• Volcanic protoliths (volcanic glass, feldspar, biotite…) embedded in a microlithic matrix • Cross-bedded, sandy volcanic sediments overlain by parallel-bedded ashfall comprising coarse, light-colored laminations of 50–500 μm volcanic protoliths replaced by silica and hydromuscovite, alternating with darker, fine grained silica gel/volcanic dust-rich layers • These layers are separated by a subaerial deposit composed of rounded pumice fragments of >1 cm • Silica veins from <100 μm up to a few millimeters crossing the chert sample
Mineralogy (optical and Raman)	• Identified volcanic protoliths include volcanic glass, pumice, feldspars, amphiboles (or pyroxenes), and multiphase volcanic rock fragments; in addition to the volcanic grains, silica-dust gel composed of microcrystalline quartz and fine-grained volcanic dust occurs as dark pebbles • A barite crystal associated with pyrite was also observed	• Identified volcanic protoliths include volcanic glass, pumice, feldspars, amphiboles (or pyroxenes), and multiphase volcanic rock fragments; in addition to the volcanic grains, silica-dust gel composed of microcrystalline quartz and fine-grained volcanic dust occurs as dark laminations including silica spherules • A tourmaline crystal was also observed
Geochemistry (ICP-OES/MS and LA-ICP-MS)	• The samples are mostly composed of SiO_2 (90–95%), Al_2O_3 (<5%), and K_2O (<2%) • Sample 00AU39 is less enriched in transition metals than sample 00AU40 • Cr/V versus Y/Ni indicates mixed sources (mafic and felsic) for the origin of volcanic sediments • Identification of a moderately strong seawater pattern with a slight enrichment in HREE over LREE (+ slight enrichment in LREE), sub-chondritic Y/Ho ratio, slight negative Ce anomaly, positive Eu anomaly, and negligible La, Y, and Gd anomalies in bulk sample • *In situ* analyses indicate typical seawater and continental patterns, sub-chondritic to super-chondritic ratios, mostly slight positive Ce anomalies (rare strong negative Ce anomalies in a few analyses), positive Eu anomalies, and negative to positive La, Y, and Gd anomalies	• The samples are mostly composed of SiO_2 (90–95%), Al_2O_3 (<5%), and K_2O (<2%) • Sample 00AU40 is more enriched in transition metals (V, Cr, Mn, Fe, Co, Ni, Cu, Zn…) compared with sample 00AU39 • Cr/V versus Y/Ni indicates an ultramafic source for the origin of volcanic sediments • Identification of a moderately strong seawater pattern with a slight enrichment in HREE over LREE, sub-chondritic Y/Ho ratio, negligible Ce anomaly, positive Eu anomaly, and negligible La, Y, and Gd anomalies in bulk sample • *In situ* analyses indicate typical seawater and continental patterns, sub-chondritic to super-chondritic ratios, mostly slight positive Ce anomalies (strong negative Ce anomaly in the pumice), positive Eu anomalies, and negative to positive La, Y, and Gd anomalies

HREE = heavy rare earth elements; ICP-OES = inductively coupled plasma optical emission spectrometry ; LA, laser ablation; LREE, light rare earth elements; MS = mass spectrometry ; XRF = X-ray fluorescence.

hydromuscovite and anatase during diagenesis and their intense silicification during deposition and earliest diagenesis (Figs. 5 and 6A and Table 1) (Orberger *et al.*, 2006; Westall *et al.*, 2006, 2011).

However, the volcanic protoliths of the sediments differ between the samples; the volcanic sediments in sample 00AU40 were mostly derived from the weathering of volcanogenic substrates of mafic (basaltic) composition, whereas those in sample 00AU39 were sourced from mixed mafic and felsic materials, as evidenced by Cr/V versus Y/Ni plots (Fig. 6D). The mafic to ultramafic origin of sediments in 00AU40 is also demonstrated by their enrichment in many transition metals, including V, Cr, Mn, Fe, Co, Ni, Cu, and Zn relative to 00AU39 (Fig. 6B). Rare-earth elements plus yttrium (REE+Y) plots normalized to MuQ are appropriate methods by which the relative contributions of

different chemical fluid reservoirs to Archean sediments may be distinguished (Bau and Dulski, 1996; Kamber *et al.*, 2005; Gourcerol *et al.*, 2015). Bulk analyses of the Kitty's Gap Chert (Fig. 6C and Table 2) show an overall continental signature as demonstrated by the sub-chondritic Y/Ho ratios of both samples and the relatively elevated LREE concentration of sample 00AU39, although slight enrichment in HREE over LREE indicates that there were also marine inputs.

Slight negative Ce anomalies in samples 00AU37b and 00AU39 imply slight oxidizing conditions. Eu-positive anomalies in all samples suggest a hydrothermal influence. *In situ* analyses carried out in samples 00AU39 and 00AU40 (Fig. 7 and Table 3) are generally similar to those of the bulk analyses, although small-scale variations, depending on the areas of interest analyzed, were also identified. In particular:

- The silica matrix and in the dark grain of sample 00AU39 are enriched in LREE over HREE, reflecting a terrigenous input, whereas the silica-dust gel matrix and silica vein show a typical seawater pattern (HREE>LREE);
- Different laminations in sample 00AU40 show variations between dominantly continental (LREE>HREE) and marine (HREE>LREE) deposition;
- Y/Ho ratios vary from sub-chondritic to super-chondritic in all samples, most of which are closer to the sub-chondritic values of bulk samples that are indicative of non-marine waters inputs, that is, these may have been sourced from either the hydrothermal vein or continental input from riverine flux into the tidal channel;
- Ce anomalies are slightly positive in most analyses, which implies anoxic water that is consistent with the anoxic seawater during the Archean (Kasting, 1991), whereas only a few have very strong negative Ce anomalies (in particular the dark grain and the silica vein in sample 00AU39, and the pumice fragment in sample 00AU40) that is characteristic of oxidizing conditions that may arise from the radiolysis of H_2O in the very shallow environment, as well as phase separation of hydrothermal fluids under high pressure exiting in the shallow environment (Nakamura and Takai, 2014).

4.2. Biosignatures associated with the carbonaceous matter

Westall *et al.* (2006) documented different modes of occurrence of carbonaceous matter in the Kitty's Gap Chert (Supplementary Fig. S9). In addition to those associated with the purported microfossils, they identified detrital carbonaceous fragments that comprise (1) amorphous oval to subrounded grains up to 10 μm in size that, at times, incorporated small, submicron-scale, mineral particles (Westall *et al.*, 2006, their fig. 4a), and (2) fragments of fibrous organic matter with attached, ribbed filaments (Westall *et al.*, 2006, their fig. 4d), similar to other unattached, ribbed filaments occurring in the same sample (Westall *et al.*, 2006, their fig. 7). The latter were interpreted as detrital fragments of phototrophic microbial mats formed in the vicinity of the infilling tidal channel and broken up by mechanical processes during tides and/or storms. Their analyses of the carbonaceous matter included Raman and HR-TEM observations of the extracted carbonaceous residue, as well as stepped combustion analyses of the carbonaceous residue extracted from individual, mm-thick horizons within the sample.

The results of these analyses show that the bulk carbonaceous matter (kerogen) has a mature Raman signature consistent with the age and metamorphic history of the rock and is therefore syngenetic with sediment formation, whereas stepped combustion documented $\delta^{13}C$ values of $-25.9‰$ to $-27.8‰$ consistent with microbial fractionation.

In addition to this morphological and organo-geochemical evidence for potential microbial life forms (Westall *et al.*, 2006, 2011), the characterization of the carbonaceous matter in silicified volcanic sediments of the Kitty's Gap Chert through *in situ* physical and geochemical analyses, as well as its distribution at multiple scales, is essential for identifying biosignatures and evaluating its biogenicity (Table 5 and Supplementary Table S1).

4.2.1. Demonstration of the biogenicity of the carbonaceous matter

4.2.1.1. Metallomics. Trace metal element enrichment in cells may reflect a combination of various processes, such as the selection of chemical elements for specific cellular needs (Fraústo Da Silva and Williams, 2001; Williams and Fraústo Da Silva, 2003), recovery and storage of elements in extracellular polymers as a response to toxicity (Czajka *et al.*, 1997; Hickman-Lewis *et al.*, 2019), or chelation of chemical elements to degraded organic components after the death of microbes (Gibson, 1984; Schultze-Lam *et al.*, 1996; Orange *et al.*, 2011).

Metals are bio-essential to all life in various concentrations and fulfil diverse biological functions. Indeed, they operate as structural elements and catalytic centers in metalloproteins and metalloenzymes involved in virtually all cellular functions, including DNA and RNA synthesis, respiration and photosynthesis, electron transport and detoxification (Fraústo Da Silva and Williams, 2001; Williams and Fraústo Da Silva, 2003; Zerkle, 2005; Rickaby, 2015; Robbins *et al.*, 2016; Moore *et al.*, 2017).

Under exceptional preservation conditions, such enrichments can be conserved in the preserved carbonaceous remains of cells and may be termed the paleo-metallome; the presence and relative concentrations of specific elements—both in isolation and in association—may be used to infer aspects of the metabolic landscape of the microbial biome (Hickman-Lewis *et al.*, 2020a).

We used μPIXE analyses to map the distribution of trace elements, in particular transition metals (V, Cr, Fe, Co, Ni…) and other elements (P, S, Cl, Ca…) of biological importance, associated with the carbonaceous matter in sedimentary rocks of the Kitty's Gap Chert (Figs. 10 and 11 and Supplementary Figs. S4 and S5 and Supplementary Tables S2 and S3). Generally, most of the volcanic clasts where carbonaceous matter was detected with Raman spectroscopy are enriched in biofunctional elements with respect to the adjacent silica matrix. In particular, the volcanic clasts are enriched in Cr>>S>V>As>Ca>Fe>Zn>Co>Mo>Cl relative to the matrix, but we observed some variations depending on the degree of alteration of the volcanic clasts. The more altered and carbon-coated,

Table 5. Summary of the Characteristics of the Carbonaceous Matter in the Kitty's Gap Chert

	00AU39 (close to hydrothermal vein, lowermost sedimentary layer)	*00AU40 (further from hydrothermal vein, overlying sedimentary layer)*
Microstructure (optical and Raman)	• Carbonaceous films around volcanic clasts • The Raman spectrum of carbonaceous matter has two bands at $\sim 1350\,cm^{-1}$ (disordered) and $\sim 1600\,cm^{-1}$ (graphite+disordered) typical of a mature kerogen	• Carbonaceous films around volcanic clasts • The Raman spectrum of carbonaceous matter has two bands at $\sim 1350\,cm^{-1}$ (disordered) and $\sim 1600\,cm^{-1}$ (graphite+disordered) typical of a mature kerogen
Microscale distribution (optical and Raman)	• Often located in volcanic clasts having experienced morphological and/or mineralogical alteration, and ubiquitous in the silica-dust gel matrix • Often mixed with hydromuscovite and anatase (more rarely with rutile), or completely replaces the volcanic protoliths	• Often located in volcanic clasts having experienced morphological and/or mineralogical alteration, and ubiquitous in the silica-dust gel matrix • Often mixed with hydromuscovite and anatase (more rarely with rutile), or completely replaces the volcanic protoliths • In sample 00AU40, the carbonaceous matter is also found in small quantity in volcanic clasts with less alteration
Nanostructure (TEM/STEM)	• Coatings, isolated spherical to elliptical particles, elongated structures, diffuse clouds	• Coatings, isolated spherical to elliptical particles, elongated structures, diffuse clouds
Crystallography (TEM/STEM)	• Amorphous and graphitized (onion-shaped structure) carbonaceous matter	• Amorphous and graphitized (onion-shaped structure) carbonaceous matter
Nanoscale distribution (TEM/STEM)	• Often in inclusions and around microcrystals of feldspars, or located at the edges of microcrystalline quartz polygons (more rarely found in association with microcrystals of anatase)	• Often in inclusions and around microcrystals of feldspars, or located at the edges of microcrystalline quartz polygons (more rarely found in association with microcrystals of anatase)
Elemental composition (PIXE)	• Average absolute concentrations of biofunctional elements in volcanic clasts follow the trend: P>Ca>Fe>S>Cl>Cr>V>Sr>Co>Mo>Zn>*As*>*Cu*>*Ni* • Most volcanic clasts are enriched in 8–12 biofunctional elements (Cr, As, S, Fe, V, Sr, Ca, Cl…) relative to the adjacent silica matrix • Average absolute concentrations of biofunctional elements in edges of the volcanic clasts follow the trend: P>Fe>Ca>S>Cr>Cl>Mo>Co>Sr>*As*>*Cu*>*Ni*>*Zn* • Most of the edges of the volcanic clasts are enriched in only 4–6 biofunctional elements (Cu, S, Ni, Mo…) relative to their interior, except the edges of volcanic glass that are enriched in 11 biofunctional elements (Ni, Mo, S, Cu, As, Zn, P, Co, Ca, Fe, Sr) • Average absolute concentrations of biofunctional elements in the silica-dust gel matrix follow the trend: P>Ca>Fe>S>Cl>Cr>Cu>Zn>Co>Ni>Sr>*As*>*Mo* • The silica-dust gel matrix is enriched in 11 biofunctional elements (Ni, As, Zn, Cl, Cr, Cu, S, Ca, P, Fe, Co) relative to the average matrix	• Average absolute concentrations of biofunctional elements in volcanic clasts follow the trend: Fe>Ca>P>V>S>Cr>Sr>Co>Zn>Mo>*Cu*>*As*>*Ni* • Most volcanic clasts are enriched in 8–10 biofunctional elements (V, Zn, Cr, S, Ca, Fe, As, Co…) relative to the adjacent silica matrix • Average absolute concentrations of biofunctional elements in edges of the volcanic clasts follow the trend: P>Fe>Ca>Cr>V>Sr>Co>*Ni*>*Cu*>*Zn*>*As* • Most of the edges of the volcanic clasts are enriched in only 3–4 biofunctional elements (P, Ni, Cu…) relative to their interior
Molecular composition (DUV)	• The aromatic compounds show two main fluorescent peaks at 310 and 340 nm, and the minerals one main fluorescent peak at 415–420 nm and shoulders at 430–435 and 460–465 nm • The aromatic compounds are often mixed with mineral phases (hydromuscovite and anatase)	• The aromatic compounds show one main fluorescent peak at 340–345 nm, and the minerals one main fluorescent peak at 410–415 nm with rare shoulders at 390 and 430 nm • The aromatic compounds are often mixed with mineral phases (hydromuscovite and anatase)
Molecular composition (FTIR)	• Identification of bands at $2855\,cm^{-1}$ (symmetrical CH_2 stretching), $2870\,cm^{-1}$ (symmetrical CH_3 stretching), $2925\,cm^{-1}$	• Identification of bands at $2855\,cm^{-1}$ (symmetrical CH_2 stretching), $2870\,cm^{-1}$ (symmetrical CH_3 stretching), $2925\,cm^{-1}$

(*continued*)

TABLE 5. (CONTINUED)

	00AU39 (close to hydrothermal vein, lowermost sedimentary layer)	*00AU40 (further from hydrothermal vein, overlying sedimentary layer)*
	(asymmetrical methylene CH_2 stretching), and 2960 cm^{-1} (asymmetrical end-methyl CH_3 stretching) in the aliphatic C–H stretching region (2800–3040 cm^{-1}) • Identification of a weak band at 1360 cm^{-1} (CH_3); weak bands at 1440 and 1470 cm^{-1} (C–H stretching); a weak band at 1545 cm^{-1} (C–H and N–H in amide II); and weak bands at 1650, 1705, 1720, and 1735 cm^{-1} (carbonyl and carboxyl groups) in the aromatic/alkenic region (1300–1800 cm^{-1}) • Sample 00AU39 shows more intense and diverse bands in the aromatic/alkenic region with respect to sample 00AU40 • Volcanic glass is rich in –OH with some aromatics, whereas multiphase volcanic rock fragments contain high concentrations of aromatics and variable concentrations of aliphatics and other functional groups	(asymmetrical methylene CH_2 stretching), and 2960 cm^{-1} (asymmetrical end-methyl CH_3 stretching) in the aliphatic C–H stretching region (2800–3040 cm^{-1}) • Sample 00AU40 shows more intense bands (two to five orders of magnitude) in the aliphatic C-H stretching region with respect to sample 00AU39 • Identification of a weak band at 1360 cm^{-1} (CH_3); weak bands at 1440 and 1470 cm^{-1} (C-H stretching); a weak band at 1545 cm^{-1} (C–H and N–H in amide II); and weak bands at 1650, 1705, 1720, and 1735 cm^{-1} (carbonyl and carboxyl groups) in the aromatic/alkenic region (1300–1800 cm^{-1}) • Volcanic glass is very rich in –OH, rich in aromatics with some aliphatics, but is depleted in certain functional groups, whereas multiphase volcanic rock fragments contain variable concentrations of aromatics, aliphatics, and other functional groups; the silica-dust gel matrix is particularly enriched in –OH and Si–O with some heterogeneously distributed aromatics, aliphatics, and other functional groups

DUV = deep-ultraviolet; FTIR = Fourier transform infrared; PIXE = proton-induced X-ray emission ; STEM = scanning transmission electron microscopy; TEM = transmission electron microscopy.

multiphase volcanic rock fragments show more enrichment in many transition metals and other biofunctional elements than the less altered volcanic glass fragments in both samples, for instance.

The edges of the volcanic clasts were only enriched in some biofunctional elements with respect to the carbonaceous matter in the more altered interiors. When compared against the matrix, the carbonaceous matter-enriched silica-dust gel matrix shows enrichment in almost all the biofunctional elements (except V, Sr and Mo). In general, trace elements such as Cr, V, As, or Co are particularly enriched in carbonaceous matter (Supplementary Figs. S4 and S5), and their co-occurrence reinforces a potential biological origin (Hickman-Lewis *et al.*, 2020a), whereas other trace elements such as P, Cl, Ca, or Fe are probably mostly associated with hydromuscovite (cf. Orberger *et al.*, 2006). We note that phyllosilicates, featuring finely laminated structures and negatively charged surfaces, tend to attract and improve the preservation potential of organic matter (Summons *et al.*, 2011); similar relationships between organic matter and phyllosilicates in the Kitty's Gap Chert (Westall *et al.*, 2015b) can likely explain the association of phosphorus with phyllosilicates observed by Orberger *et al.* (2006).

The Archean carbonaceous matter studied here recurrently concentrates a specific range of trace elements relevant to prokaryotic metallomes (Zerkle, 2005; Liermann *et al.*, 2007; Dupont *et al.*, 2010; Cameron *et al.*, 2012; Rickaby, 2015), including V, Mn, Fe, Co, Ni, Cu, Zn, Mo, and W in both samples. This concurs with our hypothesis that elements required for the flourishing of prokaryotic life were present within the elemental budget of the local environment and suggests that elemental enrichments associated with the carbonaceous matter reflects the preserved metallomes of microbial cells that produced the carbonaceous matter in the Kitty's Gap samples. Study of the biofunctional elements that constitute metallomes also informs us about the possible metabolisms of microorganisms during the Paleoarchean. The range of $\delta^{13}C$ values obtained in the Kitty's Gap Chert by Westall *et al.* (2006) is consistent with multiple metabolic processes, including co-existing sulfur and sulfate reduction, methanogenesis, and anoxygenic photosynthesis. The essential transition metals used by prokaryotes generally follow: Fe>>Zn>Mn>>Co, Cu, Mo>>Ni>W, V (Zerkle, 2005).

Iron is almost universally required by life, for the transport of oxygen, the catalysis of electron transfer reactions, nitrogen fixation or DNA synthesis, and is involved in all of the metabolisms mentioned earlier (Zerkle, 2005; Jelen *et al.*, 2016; Moore *et al.*, 2017). The other transition metals (Zn, Co, Cu, Mo, Ni, and V) are also essential for microbial life, in particular for metalloenzymes, and are required for the growth of some methanogens, in particular, Ni and Mo (Williams and Fraústo Da Silva, 2003; Zerkle, 2005; Jelen *et al.*, 2016; Robbins *et al.*, 2016; Moore *et al.*, 2017).

In contrast, the use of copper and molybdenum in the Paleoarchean is unlikely due to their insolubility in the reducing ocean (their bioavailability increased with ocean oxygenation) (Zerkle, 2005), and manganese and tungsten were not detected in the samples using μPIXE. The other biofunctional elements are phosphorus and sulfur, which are part of the essential elements for all living organisms

(CHNOPS), chlorine and calcium that are part of the essential cations for most living organisms, and chromium, arsenic, and strontium, which are trace elements that can be used by some species (metabolisms based on Cr or As) (Rickaby, 2015; Jelen *et al.*, 2016; Robbins *et al.*, 2016; Sforna *et al.*, 2022).

The localized presence of vanadium in association with other bio-functional elements may suggest the presence of nitrogen- or methane-cycling organisms, as proposed for similarly ancient carbonaceous materials in sediments from the Barberton Greenstone Belt (Hickman-Lewis *et al.*, 2020a). However, we are aware of the ability of EPS with its plethora of functional groups to trap metals and cannot exclude the possibility of metal enrichment being due to this process, particularly seeing as chemolithotrophs are known to produce vast amounts of EPS (Orell *et al.*, 2017; van Wolferen *et al.*, 2018).

4.2.1.2. Molecular composition. The detection of organic molecules and mapping of their distribution using DUV fluorescence and FTIR documented the presence of aromatic and aliphatic compounds. In DUV fluorescence datasets, the presence of one- or two-ring aromatic organic compounds is suggested by the identification of fluorescent bands at 310 and 340–345 nm (Figs. 12B and 13B) (Razzell Hollis *et al.*, 2023; Sharma *et al.*, 2023). We also identified other bands in the region ca. 400–500 nm that correspond to mineral phases (especially, hydromuscovite and anatase; Figs. 12B–D and 13B).

The different fluorescence signals observed between the two samples in the regions of aromatic compounds and minerals could be attributed to different organic compound contents and a different mineralogy (Mlewski *et al.*, 2018), respectively, the cause of which can be explained by different degrees of degradation undergone by the rocks having affected the preservation of the structure of organic compounds and minerals. In addition, aromatic compounds were often intermixed with hydromuscovite and anatase (Figs. 12A, C and 13A–C and Supplementary Fig. S6), corroborating observations made with Raman spectroscopy and TEM. This can be explained by microbial colonization of the most altered volcanic grains (Dong *et al.*, 2022) or binding of carbonaceous matter (by biofilms with microbial EPS) with mineral phases following the death of the microorganisms (Gibson, 1984; Schultze-Lam *et al.*, 1996; Orange *et al.*, 2011) before silicification and lithification of sediments (Westall *et al.*, 2011, 2015b).

We note, however, that the association of mantle carbon with clays has been documented in martian meteorites (Steele *et al.*, 2012, 2016, 2018). Nevertheless, there are consistent and multiple indications that, in the case of the Kitty's Gap sediments, microbial life was active and that the organic matter interleaved with the phyllosilicate layers is likely to be of biogenic origin. In FTIR, the aliphatic C–H stretching region (ca. 2800–3040 cm^{-1}; Fig. 14) and the aromatic/alkenic region (ca. 1300–1800 cm^{-1}; Supplementary Fig. S8) contain information relevant to biological compounds, in particular spectral features of specific functional groups related to the cell that enable characterization of fossilized biopolymers (Benning *et al.*, 2004; Igisu *et al.*, 2009, 2018). In our samples, the aliphatic/aromatic ratios generally remain uniformly low (Supplementary Fig. S7), reflecting the degree of aromaticity of the carbonaceous matter, which usually increases with metamorphic grade (Rouzaud and Oberlin, 1989; Bustin *et al.*, 1995).

Based on the Raman spectra, we determined that the Kitty's Gap samples experienced moderate grade metamorphism (about 350°C), thus explaining the mainly aromatic nature of the carbonaceous matter. However, while the position of the bands is similar for the two samples, their intensity varies. Indeed, we observed more intense aliphatic bands for sample 00AU40 and more intense and diverse aromatic bands for sample 00AU39. More intense bands in the aliphatic C–H stretching region in sample 00AU40 indicate a better preservation of these organic compounds, whereas more intense bands in the aromatic/alkenic region along with less intense bands in the aliphatic C–H stretching region in sample 00AU39 are consistent with the degradation of aliphatic molecules, probably due to a combination of many factors, such as the proximity to a hydrothermal source, diagenetic phenomena, and/or mechanical processes that lead to changes or degradation of carbonaceous matter.

The combined elemental and molecular compositions of the organic matter associated with altered volcanic particles and the silica-dust gel matrix strongly support the biogenic origin of the organic matter in the samples investigated. To evaluate the composition of the fossilized biopolymers, we calculated the CH_2/CH_3 and CH_3/CH_2 ratios in both samples (Supplementary Table S4). CH_2/CH_3 ratios range from ca. 1.1 to 2 in sample 00AU39 and from ca. 0.9 to 1.7 in sample 00AU40, indicating aliphatic biopolymers with relatively short, highly branched membrane lipids composed of five to six to seven to eight alkanes (saturated hydrocarbons consisting of C and H linked with single bonds). These characteristics are tentatively interpreted as isoprenoid chains that form archaeal membranes (Lin and Ritz, 1993; Igisu *et al.*, 2006, 2009, 2012, 2018; Hickman-Lewis *et al.*, 2020c). All CH_3/CH_2 ratios in samples fall within the range of those of extant prokaryotes and vary between ca. 0.5 and 0.9 in sample 00AU39 and between ca. 0.6 and 1.1 in sample 00AU40. These values are consistent with both bacterial and archaeal origins (Igisu *et al.*, 2009, 2018). Nevertheless, values higher than 0.8 suggest a potentially stronger input from archaeal membrane lipids, indicating an Archaea-dominated community (Igisu *et al.*, 2012).

A similar study was made of similarly ancient (3.47–3.33 Ga) microbial mats from volcanic sediments from the Barberton Greenstone Belt in South Africa (Hickman-Lewis *et al.*, 2020c). Our results from the Kitty's Gap Chert are very comparable to those of the Middle Marker horizon, for the aliphatic molecules. The Middle Marker Chert has CH_2/CH_3 ratios that vary between ca. 0.8 and 1.3, indicating short, highly branched chains of five to six alkanes, and CH_3/CH_2 ratios between ca. 0.8 and 1.2, all indicating a strong and likely dominant contribution from archaeal cell material.

4.2.2. Syngenicity of the carbonaceous matter

4.2.2.1. Microscale distribution and maturity of the carbonaceous matter with Raman spectroscopy. The Kitty's Gap Chert was rapidly silicified, thereby preserving the morphological and geochemical characteristics of the carbonaceous matter with high fidelity (Westall *et al.*, 2006, 2011, 2015b). Westall *et al.* (2006) observed carbonaceous

coccoidal structures interpreted as the microbial remains of chemolithotrophs in these horizons. Chemolithotrophic microorganisms use energy from redox reactions at the surface of rocks and minerals for their metabolism and are, therefore, obliged to form epilithic (surface-attached) colonies over the surface of lithic particles (Nakamura and Takai, 2014), which degrade into kerogen with time (Beyssac *et al.*, 2002a, 2002b; Foucher *et al.*, 2015).

Raman spectra obtained on carbonaceous matter in the studied samples show that it has undergone some graphitization, but is mostly amorphous, as indicated by the more intense D1 (disordered carbon) relative to the D2+G (graphite and disordered carbon) band, despite some specific locations showing a more intense D2+G band (Fig. 8E) (Foucher *et al.*, 2015). The thermal maturity (300–400°C) of the carbonaceous matter is similar to that of the host rock (Kisch and Nijman, 2004), strongly supporting its syngenicity (Westall *et al.*, 2006; Foucher *et al.*, 2015). Raman maps documented the distribution of the carbonaceous matter, which is localized on the surface of the volcanic grains and in the silica-dust gel matrix (Figs. 5 and 8A–D). More precisely, we found that carbonaceous matter is preferentially associated with volcanic grains that have undergone the greatest degree of alteration, either mechanical alteration (grains with increasingly rounded edges) and/or mineralogical alteration (grains replaced by hydromuscovite and anatase), as well as in smaller quantities on some of the less altered volcanic grains. The direct association of the carbonaceous matter with the particles, their surfaces, and the silica-dust gel matrix, as well as its mature Raman signature, demonstrate that it formed at the same time as the original sediments and is, therefore, syngenetic. Further, no evidence for secondary mobilization of carbonaceous materials, either through fractures and along planes of weakness in the rock (Rasmussen *et al.*, 2021) or through pyrobitumen formation processes (Rasmussen and Buick, 2000), has been identified in any studied samples.

The carbonaceous matter around volcanic grains may represent either a macromolecular conditioning film made up of organic macromolecules of biological origin (*e.g.*, proteins or exopolymers) that were adsorbed onto the surface of volcanic grains after a few minutes of immersion of a surface (Bhagwat *et al.*, 2021), or epilithic microbial biofilms composed of silicified coccoidal microorganisms embedded in an exopolymeric monolayer on the surface of volcanic minerals (Westall *et al.*, 2006, 2011, 2015b). The colonization of volcanic substrates (rocks and dust) by microbes provides them with advantageous protection against challenging external conditions (UV, abrasion by water, wind, etc.) by creating micro-environments favorable to the survival and development of certain microbial communities (Westall *et al*., 2011, 2015b; Dong *et al.*, 2022). Minerals are also crucial sources of nutrients (bioessential elements needed for microbial growth and metabolism) and energy (electron acceptor/donors and electrical conductors to facilitate extracellular electron transfer; Dong *et al.*, 2022; Westall *et al.*, 2011, 2015b) for chemolithotrophic microorganisms.

Volcanic dust (<20 μm), notably, presents a greater surface area than coarser volcanic grains (>50 μm), making energy and nutrients more readily accessible to microorganisms. Small colonies of interpreted fossil microbes and EPS are common in the silica-dust gel, which is also an environment favorable for the preservation of microbial matter (Westall *et al.*, 2015a; McMahon *et al.*, 2018), thus explaining the ubiquity of the carbonaceous matter.

4.2.2.2. Correlation of the carbonaceous matter using TEM, scanning electron microscopy, and optical microscopy. The carbonaceous matter in the Kitty's Gap Chert presents various morphologies at the nanoscale. Several structures of carbonaceous matter have been observed in TEM in the form of (1) coatings around volcanic grains; (2) isolated spherical to elliptical particles; (3) elongated structures; and (4) diffuse clouds. Based on the other datasets presented here, we can interpret the potential origins of some of these structures.

The coatings (Fig. 9A and Supplementary Figs. S2 and S3) probably represent the carbonaceous films observed at a larger scale around volcanic clasts (see section 4.2.2.1. *Microscale distribution and maturity of the carbonaceous matter with Raman spectroscopy*). However, abiotic carbonaceous films could theoretically also develop on aqueously submerged surfaces (*e.g.*, in seawater, conditioning films of hydrocarbons are formed on surfaces within a few minutes of immersion). Our investigations described earlier document multiple lines of evidence for a biological origin. The elongated structures (Fig. 9E, F and Supplementary Fig. S3) are probably the degraded remnants of EPS-rich microbial biofilms, similar to those observed with scanning electron microscopy (SEM) by Westall *et al.* (2006, 2011) (Supplementary Fig. S9).

The diffuse clouds (Supplementary Fig. S2) that exhibit a brown color and irregular shape in optical microscopy (Fig. 5M) probably represent highly degraded volcanic protoliths that were coated with microbial biomass. The isolated spherical to elliptical particles (Fig. 9A–D and Supplementary Figs. S2 and S3) are more intriguing. They could be ''free-floating'' detrital carbonaceous particles that represent chemotrophic microbial biomass supplied with nutrients (such as Cr, Co, Ni and Cu) by the hydrothermal fluids, as identified by Westall *et al.* (2015b) in the Kitty's Gap and Josefsdal Cherts, or particles of insoluble carbonaceous matter similar to those found in interplanetary dust particles and meteorites (Westall *et al.*, 2015b).

The carbonaceous matter in the Kitty's Chert presents two types of nanostructure: (1) amorphous carbon and (2) crystallized (graphitized) carbon. Amorphous carbonaceous matter was identified in numerous different structures (coatings, isolated spherical to elliptical particles, elongated, EPS-like matter; Fig. 9A, B, E, F), whereas graphitized carbonaceous matter was identified only in isolated particles within the silica-dust gel matrix, where it presents an onion-shaped nanostructure (Fig. 9C, D). We hypothesize that the amorphous carbonaceous matter corresponds to the degraded remains of microorganisms in sediments. However, finely disseminated microbial remains may also be mixed with an abiotic carbonaceous matter derived from different sources (hydrothermal, meteoritic, atmospheric, etc.) (Sephton, 2002; Lindsay *et al*., 2005; Ceburnis *et al.*, 2011; Gourier *et al.*, 2019). Given that there is a generally invisible background influx of extraterrestrial carbonaceous matter arriving continually on Earth (Maurette *et al.*, 2000;

Maurette, 2006) and Mars (Eigenbrode *et al.*, 2018) and that this influx is modelled to have been higher during the Hadean and Paleoarchean (Maurette, 2006), it is likely that a similar invisible extraterrestrial component is present in most terrestrial sediments.

Mixing of this extraterrestrial component with sediments before silicification and metamorphism (300–400°C) would dilute the extraterrestrial signal, rendering it impossible to distinguish except in exceptional circumstances (Gourier *et al.*, 2019).

On the other hand, the graphitized carbonaceous matter obviously has a different origin. Westall *et al.* (2006, 2015b) noted carbonaceous fragments in the Kitty's Gap Chert that were clearly detrital in origin (Supplementary Fig. S9). Some of them had a filamentous aspect, with attached ''floating'' striated filaments that the authors interpreted as fragments of phototrophic microbial mats. Others had a solid, sub-rounded appearance and were more resistant to erosion, suggesting a different origin. It is likely that these solid, eroded, detrital particles are those observed here in TEM with an onion-like nanostructure that exhibits a more graphitized texture, as evidenced by the measured interplanar distance of ca. 3.5 Å in carbonaceous matter, corresponding to graphitized carbon (Derenne *et al.*, 2008). We hypothesize that these fragments may be of mantle origin. Having experienced high temperatures in the mantle (<1000°C) (Mathez, 1987) and having been eroded from volcanic rocks, this kind of organic particle should be readily distinguishable from carbonaceous matter formed at the surface of Earth by other processes (*e.g.*, biogenic).

The nanoscopic carbonaceous matter is often distributed as inclusions and coatings around microcrystals of feldspar (Fig. 9A and Supplementary Figs. S2 and S3), intimately mixed with hydromuscovite sheets (ca. 10 and 20 Å interplanar distances between crystal planes), localized at the edges of microcrystalline quartz polygons (Supplementary Fig. S3A, C), or more rarely found at the edges of volcanic grains associated with microcrystals of anatase (Supplementary Figs. S2 and S3).

The association of carbonaceous matter and hydromuscovite is not surprising because phyllosilicates are known to play a role in preventing the degradation of organic matter due to intercalation within the interlayer spaces of phyllosilicates (Summons *et al*., 2011; Keil and Mayer, 2014). The presence of carbonaceous matter at the edges of the quartz polygons could be explained by the displacement of pre-existing organic matter (*e.g.,* microbial biomass) due to Ostwald ripening of the microcrystalline quartz during lithification of the silica cement (Hickman-Lewis *et al.*, 2018, 2020a).

Indeed, the quartz microcrystals present in the sediments of the Kitty's Gap Chert originated from silica that resulted mainly from Paleoarchean seawater saturated with silica intermixed with porewater silica produced by devitrification of the volcanic detrital grains. The enriched porewater silica then polymerized to form a silica gel matrix cement around the volcanic grains before recrystallizing into quartz after diagenesis and then metamorphism (Westall *et al.*, 2023). The ubiquitous presence of microcrystalline silica in the samples confirms the rapid and pervasive lithification of sediments as a mechanism for the preservation of organics. One outstanding issue is the fact that we could not visualize the individual fossilized cells reported by Westall *et al.* (2006, 2011) by electron microscopy. This may be due to a number of reasons. In particular, the SEM observations document a preponderance of generic EPS embedding the fine-grained volcanic dust/silica (Supplementary Fig. S9B) matrix rather than actual cells (Supplementary Fig. S9C–E). When present, the cells generally occur in very small groups of only a few individuals (Supplementary Fig. S9C) covering an area of only a few square micrometers. Rarely, larger groups of cells up to 10 or more square micrometers in areal extent are preserved (Supplementary Fig. S9D, E). These associations are interpreted as monolayers of cells, generally already slightly degraded (and flattened) when fossilized, resulting in thicknesses of a few 100 nm. Their sporadic distribution and subtle traces, often slightly displaced by the growth of microcrystalline quartz, result in very thin layers of organic matter between quartz crystals, possibly similar to the structure shown in Supplementary Fig. S3C. Further, their diffuse distribution precludes detection in thin section, so it is difficult to be certain that the accumulations of carbonaceous matter chosen for FIB preparation represents microbial biomass. These reflections underline the difficulties in determining the biogenicity of small and sporadically distributed microorganisms, such as these interpreted chemolithotrophs, and further investigations may be required to confirm the biogenicity of the fossilized cells.

4.3. The Kitty's Gap sediments as functional analogues for returned martian sediments

The Kitty's Gap Chert is proposed as an analogue of martian materials from the period of time during which conditions at the surface of Mars are considered to have been habitable (Noachian–Late Noachian; McKay and Stoker, 1989), and from which we could potentially find fossilized traces of life similar to those observed in Archean sediments (Table 6). The Kitty's Gap Chert is more precisely considered as a ''functional analogue'' because it has characteristics more or less similar to those observed or expected in martian rocks (Foucher *et al.*, 2021). Indeed, the volcanic sediments have a similar origin (mainly mafic sediments). The sediments were deposited in a shallow water environment under wave/wind agitation or in static water, influenced to varying degrees by hydrothermal activity. Sediments in Gale and Jezero craters on Mars were also partially formed under standing bodies of water and in shallow water depths (lakes). Recently, evidence for ripples has been found in Gale Crater sediments, similar to the wave ripples exhibited by the Kitty's Gap Chert (https://www.nasa.gov/feature/jpl/nasa-s-curiosity-finds-surprise-clues-to-mars-watery-past, February 8, 2023).

Likely evidence for hydrothermal activity was detected by the Spirit rover at Home Plate in Gusev Crater (Ruff and Farmer, 2016). Although no traces of hydrothermal activity have yet been detected in either Jezero or Gale Crater, the very volcanic nature of their basement rocks and the magmatic origin of certain formations within makes it highly plausible that hydrothermal activity was associated with their eruption. Perseverance has documented the aqueous alteration of Jezero basalts (Farley *et al.*, 2022; Scheller *et al.*, 2022), and aqueous alteration of fine-grained volcanic

Table 6. Comparison of the Kitty's Gap Chert and Associated Biosignatures Compared with Martian Rocks in Jezero Crater of Similar Age (~3.5-Ga-Old) and the Potential Traces of Life They Could Contain (Modified After Westall et al., 2015b)

	Kitty's Gap Chert	*Martian rocks in Jezero Crater (Simon et al., 2023)*
Rock age	• Paleoarchean (3.45 Ga)	• Noachian period (>3.6 Ga)
Depositional environment	• Shallow water, tidal basin	• Lacustrine to fluvial
Sediment composition	• Mainly basaltic sediments (mafic to ultramafic), some more evolved sediments (rhyolitic)	• Mainly basaltic sediments, some more evolved volcanics (andesite)
Matrix	• Silica	• Secondary minerals such as phyllosilicates, salts, and sulfates (with a potential amorphous or nanocrystalline silica phase)
Primary minerals	• Volcanic glass, pumice, feldspar, amphibole, pyroxene…	• Pyroxene, olivine, feldspar
Diagenetic alteration minerals	• Volcanic grains altered to phyllosilicates and anatase, secondary hydrothermal minerals (microcrystalline quartz, barite, pyrite…)	• Volcanic grains altered to phyllosilicates (Fe-Mg smectite), salts, carbonates, sulfates, phosphates, iron oxides…
Source of fluids	• Mix of seawater, hydrothermal, and continental (riverine) inputs	• Lacustrine input, potential hydrothermal input related to volcanic activity
Habitable environment	• pH acidic-neutral (partly alkaline); anaerobic with micro amounts of abiotic O_2; moderate-high temperatures (~50–70°C); metal-rich (V, Cr, Mn, Fe, Co, Ni…)	• pH neutral (possibly partly acidic and partly alkaline); anaerobic (possibly micro amount of abiotic O_2); generally low temperatures (possibly higher with hydrothermalism); metal-rich (Cr, Mn, Fe…)
Origin of organics	• Biological, hydrothermal, mantle, atmospheric (aerosols from volcanic ashes or sea spray), extraterrestrial	• Certainly extraterrestrial, mantle, and atmospheric (aerosols from volcanic ashes), possibly biological and hydrothermal
Preservation of organics	• Rapid silicification	• Entombment by cementing phyllosilicates, salts, and/or sulfates
Type of microorganisms	• Anaerobic chemolithotrophs, chemoorganotrophs, phototrophs	• Environment consistent with physicochemical requirements of anaerobic chemolithotrophs, chemoorganotrophs (in the vicinity of hydrothermal activity), and phototrophs
Energy source for microbes	• Redox reactions of inorganic (mineral) or organic (dead biological) materials; photons	• Redox reactions of inorganic (mineral) or organic (dead biological) materials if there was life; photons
Distribution of microbes	• At the surface of volcanic clasts (chemolithotrophs), in particular associated with hydromuscovite and anatase; ubiquitous in the silica-dust gel matrix; in subaerial deposits where pumice is embedded (phototrophs)	• At the surface of volcanic clasts (if chemolithotrophs and chemoorganotrophs existed); in the phyllosilicate/salt/sulfate (amorphous silica?) matrix; on the surface of bedding planes (if phototrophs existed)
Raman spectral signature	• Raman spectra of the carbonaceous matter characterized by two bands at ~1350 and 1600 cm^{-1}, typical of a kerogen	• Low abundances of organics, only a possible G band (~1600 cm^{-1}) were detected
Morphological biosignatures	• Cells, colonies, EPS forming carbonaceous films around volcanic clasts (coatings, elongated structures), carbonaceous clots (isolated spherical to elliptical particles), filaments, diffuse clouds	• Cells, colonies, EPS-forming carbonaceous films, carbonaceous clots, filaments, diffuse clouds if cementation was rapid; MISS (Noffke, 2015; Noffke, 2009)
Metabolic biosignatures	• Carbon isotopic composition ranging from −26‰ to −30‰	• Restrictive negative carbon isotopic composition
Elemental biosignatures	• Carbonaceous matter coating the volcanic clasts concentrates the following trace elements: P>Fe>Ca>S>V>Cr>Cl>Sr>Co>Mo>Zn>*Cu*>*As*>*Ni*; the carbonaceous matter located at the edges of the volcanic clasts concentrates the following trace elements: P>Fe>Ca>Cr>S>Cl>V>Mo>Sr>Co>*Cu, Ni*>*As*>*Zn*; the silica-dust gel matrix is enriched in P>Ca>Fe>S>Cl>Cr>Cu>Zn>Co>Ni>Sr>*As*>*Mo*	• Concentration of trace transition metals used by prokaryotes in volcanic minerals, such as Fe, Zn, Mn, Co, Cu, Mo, Ni, and other bioessential elements (CHNOPS…)

(*continued*)

Table 6. (Continued)

	Kitty's Gap Chert	*Martian rocks in Jezero Crater (Simon et al., 2023)*
Molecular biosignatures	• Aliphatic/aromatic ratios relatively low • Aromatic compounds at ~310 and 340–345 nm in DUV • Aliphatic compounds at ~2855, 2870, 2925, and 2960 cm^{-1} in FTIR • CH_2/CH_3 ratios ranging from ~0.9 to 2 (relatively short, highly branched aliphatic biopolymers) • CH_3/CH_2 ratios ranging from ~0.5 to 1.1 (mixed to Archea-dominated community)	• Aliphatic/aromatic ratios could be variable • Better detection of aromatic compounds if the biological remains have undergone impact metamorphism/better preservation and detection of aliphatic compounds if the biological remains have not been subjected to impact metamorphism • Detection of one- and two or more-ring aromatic molecules (Razzell Hollis et al., 2023)

EPS = extracellular polymeric substances; MISS = microbially induced sedimentary structures.

sediments in Gale Crater has also been documented (Mangold *et al.*, 2019). Thus, the similarities between the early terrestrial volcanic sediments and their martian counterparts are very strong.

The main difference between the Kitty's Gap Chert and similar volcanic sedimentary rocks on Mars is that the former was pervasively and very rapidly silicified. A similar diagenetic process apparently took place at Home Plate (Ruff and Farmer, 2016) but has not yet been identified elsewhere on Mars. Nevertheless, this is a minor point in the sense that it is the nature of the sediments, their environment of deposition, and the nature of their microbial inhabitants that is important for use as an astrobiological analogue (cf. Foucher *et al.*, 2021; Hickman-Lewis *et al.*, 2022b).

On Mars, whereas cells may have been entombed by cementing materials in the matrix (clays, salts), it is more likely that the organic remains of microbes would have been preserved as generic heterogeneous biomass or EPS, which could have been equally entombed by the matrix cement, in particular, between clay sheets (although this has not yet been demonstrated) or possibly within hydrated silica (Tarnas *et al.*, 2019). In addition, despite the great age of the locations investigated *in situ* on Mars (>3.6 Ga), primary organic matter would not have undergone the degree of metamorphism to which similar-aged sediments on Earth have been subjected through plate tectonics, although impact metamorphism is probable in many localities on Mars.

It would, therefore, be possible to find both well-preserved and very graphitized organic matter. Despite these differences in preservation and degradation, the carbonaceous composition of the fossilized remains of microbes, associated with specific morphological, metabolic, elemental, and molecular characteristics in the Kitty's Gap Chert, can be considered as good analogue biosignatures for astrobiological investigations in martian rocks.

The Mars 2020 mission is performing *in situ* analyses with the Perseverance rover and collecting samples, including potentially interesting samples for the search for traces of life, to be returned to Earth to perform more in-depth analyses in laboratories (Farley *et al.*, 2020). Such samples are being chosen based on their sedimentological characteristics, as well as the presence of organic matter detected *in situ* in direct association with its mineralogical context using the SHERLOC (Beegle *et al.*, 2020) and PIXL (Allwood *et al.*, 2021) instruments. The former uses UV resonance Raman and native deep UV fluorescence spectroscopy to document and map the distribution of carbonaceous matter, whereas the second is an XRF spectrometer that acquires high spatial resolution observations of rock and regolith chemistry. Our Kitty's Gap Chert study has demonstrated how arduous the determination of the biogenicity of organic matter in volcanic sediment samples can be, even in well-equipped terrestrial laboratories. *In situ* analysis on Mars can produce tantalizing and highly promising information.

For definitive demonstrations of biogenicity, however, the samples will need to be analyzed in terrestrial laboratories with state-of-the-art instrumentation as shown herein. Terrestrial environments analogous to Jezero crater sedimentary sequences have been studied using rover-like instrumentation (Azua-Bustos, 2023), showing that it is very difficult to identify organic materials and biosignatures within; this again outlines the importance of MSR. The selection of martian samples for return to Earth will also need to consider the spatio-temporal stresses between the moment of the selection and analysis (approximately a decade), as well as the launch from Mars and the landing on Earth that can induce, for example, disarticulation and breaking apart of poorly consolidated samples within the sample tube. Analysis of the samples in terrestrial laboratories must also take into consideration planetary protection concerns, for example, the sterilization of the samples. As explained by Velbel *et al.* (2022), ''targeted investigations using analogs of MSR Campaign-relevant returned-sample types should be undertaken to fill knowledge gaps about sterilization effects on important scientific measurements.'' As such, it would be informative to follow the proposed sterilization processes of Velbel *et al.* (2022) on terrestrial Mars analogues, including dry heating under two temperature regimes: 180°C for 3 h and 250°C for 30 min. However, it is important to note that such heat treatments would probably not affect the Kitty's Gap Chert samples since they were naturally exposed to higher temperatures consistent with their degree of metamorphism, but this is not the case for potential martian organic matter.

In addition, the inherently limited quantity of samples available must be considered in the development of any analytical protocol. Analyses carried out in the laboratory will, however, enable the use of techniques impossible to employ *in situ* on Mars but must be as non-invasive and non-destructive as possible to extract a maximum of qualitative and quantitative data from a minimum volume of

sample (Hickman-Lewis *et al.*, 2022b). Considering the caveat cited earlier, we propose a list of analyses to be performed to maximize the detection of microfossils in martian samples where a limited amount of material samples is available, organizing these analyses according to their potential alteration effect on the samples (the first techniques being essential to decide whether one continues to analyze the samples with more invasive/destructive techniques):

- Optical microscopy: non-invasive technique to study the mineralogy of rocks and the alteration of minerals, identify potential morphological biosignatures, and contextualize and select ROI for subsequent analyses;
- Raman spectroscopy: non-invasive technique to identify and localize carbonaceous matter related to possible remains of microfossils and provide the mineralogical context of potential biosignatures;
- Laboratory and synchrotron-based techniques such as FTIR and DUV-luminescence spectroscopies: non-invasive techniques to identify the molecular composition of the carbonaceous matter;
- SEM/TEM-EDX: micro-invasive technique to observe individual microstructures and textures and map major elements possibly associated with carbonaceous matter and (bio)minerals;
- μPIXE: micro-invasive technique (high analysis energy) to map the distribution of trace metals in the carbonaceous matter.

Most methods listed here are non-invasive during the analyses of samples, but they may require the preparation of samples (*e.g.*, preparation of thin sections or polished sections for optical microscopy or Raman spectroscopy; acid attack or metallic coating for SEM; extraction of FIB sections for TEM), which irreversibly leads to the destruction of samples and possibly the loss of information (*e.g.*, textural and structural information). Further, we recommend that each of the methodologies proposed for MSR analyses as listed earlier should be evaluated in light of whether the proposed sterilization protocol (cf. Velbel *et al.*, 2022) will have negative effects on sample integrity or the preservation of putative organic and inorganic biosignatures within to determine which suite of techniques will yield important information for life detection.

5. Conclusions and a Proposal for a Martian Sample Analysis Protocol

The paleoenvironment of the Kitty's Gap Chert was documented using sedimentological, petrological, mineralogical, and geochemical characterization. These analyses revealed that the sedimentary rocks of the Kitty's Gap Chert were deposited in a shallow-water, semi-enclosed tidal basin influenced by the erosion of landmasses of volcanic origin and hydrothermal fluids. The paleoenvironment of the Kitty's Gap Chert was, therefore, metal-rich, thermophilic, slightly acidic (although, at times, partly alkaline), and supplied with chemical fluids derived from different reservoirs. The studied samples were, therefore, habitable for microbial life during the Paleoarchean.

The carbonaceous matter associated with putative degraded remains of fossilized microorganisms was studied with morphological, elemental, and molecular analyses; its distribution was characterized at multiple scales, confirming its biological origin. In particular, the elemental and molecular composition and nanostructure of carbonaceous matter can be used as complementary biosignatures. Carbonaceous matter generally coats volcanic clasts and is ubiquitous in the volcanic dust, characteristics that support the previous interpretation of chemolithotrophic microorganisms.

The carbonaceous matter is characterized by excess concentrations of biologically useful transition elements, such as Cr, V, As, Fe, Zn, and Co relative to other parts of the volcanic clasts and the matrix, both of which are poor in carbonaceous matter. This trace metal budget could be an indication about the possible microbial metabolisms present during the deposition of the Kitty's Gap Chert, such as sulfur and possibly sulfate reduction (although there was little sulfate in the Paleoarchean oceans), or methanogenesis. Alternatively, it may represent chelation of metals to the abundant microbial EPS characteristic of chemolithotrophic microorganisms.

The molecular composition of the carbonaceous matter reveals variations in aromatic and aliphatic compounds, reflecting significant preservation of biomolecular diversity in the Kitty's Gap Chert despite their great age. The CH_2/CH_3 and CH_3/CH_2 ratios suggest a mixed community composed of Bacteria and Archaea, with potential dominance by the latter. Our results confirmed the biogenicity of the amorphous carbonaceous matter in the Kitty's Gap Chert, as well as the presence of a detrital carbonaceous matter component characterized by a higher, more graphitized maturity, that may be of mantle origin. We were also able to confirm the syngenicity of the carbonaceous matter.

Comparison of the microfossil-like carbonaceous structures revealed previously by SEM with those investigated herein using petrological thin sections and FIB sections allowed us to verify the presence of EPS and graphitized detrital particles. On the other hand, incontrovertible identification of the microorganisms observed by SEM proved to be more difficult, likely due to their extremely delicate and probably subtle appearance in thin section. This underlines the challenges that will be faced if returned martian samples contain similar traces of chemotroph-like microorganisms. Further work will be needed to address this aspect.

The very simple nature of the fossilized life forms in the Kitty's Gap Chert and the shallow, volcanic and hydrothermal, aqueous environment in which they formed, make such sediments excellent functional analogues for martian sediments. Such sediments could be used in the elaboration of procedural protocols for searching for traces of fossilized life in samples returned from Mars. An example of such a protocol for the analysis of sedimentary samples is given next:

- Macroscopic observations and imaging of structures (bedding, laminations, fractures, veining, stylolites, orientation of the clasts, brecciation, deformation, redox fronts, concretions, secondary mineral precipitation, etc.) and textures (grain size, grain roundness, sorting, etc.) in sub-samples extracted from the core samples collected by the Perseverance rover. These details will contribute to the evaluation of habitability already assessed at the sampling sites on Mars and will provide additional information related to the preservation of

potential biosignatures (also note that half of each sample will be set aside for future analysis with more advanced technology, some of which may not yet have been invented);

- On each subsample taken for analysis, the following information will be needed:
  - Mineralogical identification and analysis of alteration features (diagenetic, post-diagenetic, shock, etc.). This information can be obtained using optical microscopy coupled with Raman and/or IR spectroscopy, for example;
  - Documentation of the distribution of carbonaceous matter, and verification of its association with mineral grains or vein features using spectral techniques, such as Raman and IR;
  - Documentation of any (microscopically) visible microstructures and textures of potentially biogenic origin (microfossils, biofilms, filaments, EPS, etc.) using high-resolution microscopic observations, such as SEM or TEM;
  - Mapping of elements (major to trace) associated with the carbonaceous matter and identification of (bio)minerals using elemental spectroscopy (techniques such as μPIXE, EDX, and fluorescence spectroscopy);
  - Identification of the molecular composition of the carbonaceous matter using methods such as synchrotron-based FTIR and DUV-luminescence spectroscopy.

Combining a range of techniques that yield complementary datasets at different spatial scales will represent the most appropriate means of characterizing putative biosignatures in returned martian samples while carefully addressing the potential non-biological processes by which such features could have formed. Finally, it will also be necessary to consider the effects of sterilization processes that will be applied to returned martian samples to comprehensively understand their effects on putative biosignatures within rock samples.

Acknowledgments

The authors acknowledge Sylvain Janiec (ISTO-CNRS, Orléans, France) and Cédric Demeurie (Thin Section Lab, Toul, France) for the preparation of thin sections, and David Troadec (IEMN-CNRS, Villeneuve d'Ascq, France) for the production of FIB sections. They are grateful to Julian Gentile (University of Montpellier) for help with sample characterization of two thin sections with optical microscopy and Raman spectroscopy. They thank Audrey Saul-dubois for technical help with FIB section analyses using the JEOL ARM200 CFEG TEM/STEM (MACLE facility, ICMN-CNRS, Orléans, France), and Fabienne Warmont with FIB section analyses using the PHILIPS CM20 TEM/STEM (ICMN-CNRS, Orléans, France). They also thank Frédéric Jamme for technical assistance with sample analyses using DUV fluorescence spectroscopy at DISCO beamline, Solenn Réguer for technical assistance with samples analyses using XRF spectroscopy at DiffAbs beamline (Synchrotron SOLEIL, Saint-Aubin, France), and Wren Montgomery for assistance with FTIR sample analysis at the NHM London. S.P. thanks the Institut National de la Santé et de la Recherche Médicale.

Authors' Contributions

L.C., F.F., and F.W. conceived the research. F.W. collected samples. L.C., F.F., K.H.L, S.S., J.J., M.R., G.C., S.P., B.G., and F.W. performed the experiments. L.C. processed and analyzed the data. L.C. wrote the paper, with contributions from all authors.

Author Disclosure Statement

No competing financial interests exist.

Funding Information

This research was funded by the Centre National de la Recherche Scientifique (CNRS), the Centre National d'Etudes Spatiales (CNES), the University of Orléans, and the UK Space Agency (Grant No. ST/V00560X/1 to Keyron Hickman-Lewis). This project has benefited from the expertise and the facilities of the Platform MACLE–CVL, which was co-funded by the European Union and Centre-Val de Loire Region (FEDER), and from the AIFIRA facility, financially supported by the CNRS, the University of Bordeaux, and the Région Nouvelle Aquitaine. FIB experiments were supported by the French RENATECH network, the CPER Hauts de France project IMITECH, and the Métropole Européenne de Lille. DUV and XRF experiments were supported by Synchrotron SOLEIL (Projects Nos. 99210115, 20211055 and 20220200). FTIR analyses at the NHM London were supported by Europlanet 2024 RI (Grant No. 871149).

Supplementary Material

Supplementary Data

References

Allwood AC, Kamber BS, Walter MR, *et al*. Trace elements record depositional history of an early Archean stromatolitic carbonate platform. *Chem Geol* 2010;270(1–4):148–163; doi: 10.1016/j.chemgeo.2009.11.013

Allwood AC, Hurowitz JA, Clark BC, *et al.* The PIXL Instrument on the Mars 2020 Perseverance Rover. In: *52nd Lunar and Planetary Science Conference;* 2021. Available from: https://www.hou.usra.edu/meetings/lpsc2021/pdf/1591.pdf [Last accessed: December 6, 2023].

Azua-Bustos A. Dark microbiome and extremely low organics in Atacama fossil delta unveil Mars life detection limits. *Nat Commun* 2023;14(1):808; doi: 10.1038/s41467-023-36172-1

Barberet P, Jouve J, Sorieul S, *et al.* AIFIRA: A light ion beam facility for ion beam analysis and irradiation. *Eur Phys J Plus* 2021;136(1):67; doi: 10.1140/epjp/s13360-020-01045-9

Bau M and Dulski P. Distribution of yttrium and rare-earth elements in the Penge and Kuruman iron-formations, Transvaal Supergroup, South Africa. *Precambrian Res* 1996; 79(1–2):37–55; doi: 10.1016/0301-9268(95)00087-9

Beegle LW, Bhartia R, DeFlores L, *et al.* The SHERLOC Investigation on the Mars 2020 Rover. In: *51st Lunar and Planetary Science Conference*; 2020; p. 2081. Available from: https://www.hou.usra.edu/meetings/lpsc2020/pdf/2081.pdf [Last accessed: December 6, 2023].

Benison KC, Bosak T, Clark BC, *et al*. Biosignature potential and possible environmental indicators of sulfate-rich rocks from Hogwallow Flats and Yori Pass, Jezero Crater

Delta Front, Mars. In: *54th Lunar and Planetary Science Conference*; 2023. Available from: https://www.hou.usra.edu/meetings/lpsc2023/pdf/2570.pdf [Last accessed: May 31, 2023].

Benning LG, Phoenix VR, Yee N, *et al.* Molecular characterization of cyanobacterial silicification using synchrotron infrared micro-spectroscopy. *Geochim Cosmochim Acta* 2004;68(4):729–741; doi: 10.1016/S0016-7037(03)00489-7

Beyssac O, Goffé B, Chopin C, *et al.* Raman spectra of carbonaceous material in metasediments: A new geothermometer. *J Metamorph Geol* 2002a;20(9):859–871; doi: 10.1046/j.1525-1314.2002.00408.x

Beyssac O, Rouzaud J-N, Goffé B, *et al.* Graphitization in a high-pressure, low-temperature metamorphic gradient: A Raman microspectroscopy and HRTEM study. *Contrib Mineral Petrol* 2002b;143(1):19–31; doi: 10.1007/s00410-001-0324-7

Bhagwat G, O'Connor W, Grainge I, *et al*. Understanding the fundamental basis for biofilm formation on plastic surfaces: Role of conditioning films. *Front Microbiol* 2021;12:687118; doi: 10.3389/fmicb.2021.687118

Bibring J-P, Langevin Y, Mustard JF, *et al.* Global mineralogical and aqueous Mars history derived from OMEGA/Mars Express Data. *Science* 2006;312(5772):400–404; doi: 10.1126/science.1122659

Bost N, Westall F, Ramboz C, *et al.* Missions to Mars: Characterisation of Mars analogue rocks for the International Space Analogue Rockstore (ISAR). *Planet Space Sci* 2013; 82–83:113–127; doi: 10.1016/j.pss.2013.04.006

Brasier MD, Green OR, Jephcoat AP, *et al.* Questioning the evidence for Earth's oldest fossils. *Nature* 2002;416(6876): 76–81; doi: 10.1038/416076a

Brasier MD, Antcliffe J, Saunders M, *et al*. Changing the picture of Earth's earliest fossils (3.5–1.9 Ga) with new approaches and new discoveries. *Proc Natl Acad Sci U S A* 2015; 112(16):4859–4864.

Bustin RM, Ross JV, Rouzaud J-N. Mechanisms of graphite formation from kerogen: Experimental evidence. *Int J Coal Geol* 1995; doi: 10.1016/0166-5162(95)00002-U

Cameron V, House CH, Brantley SL. A first analysis of metallome biosignatures of hyperthermophilic Archaea. *Archaea* 2012;2012:1–12; doi: 10.1155/2012/789278

Cas R, Giordano G, Balsamo F, *et al.* Hydrothermal Breccia textures and processes: Lisca Bianca Islet, Panarea Volcano, Aeolian Islands, Italy. *Econ Geol* 2011;106(3):437–450; doi: 10.2113/econgeo.106.3.437

Ceburnis D, Garbaras A, Szidat S, *et al.* Quantification of the carbonaceous matter origin in submicron marine aerosol by ^{13}C and ^{14}C isotope analysis. *Atmos Chem Phys* 2011;11(16): 8593–8606; doi: 10.5194/acp-11-8593-2011

Cockell CS, Balme M, Bridges JC, *et al*. Uninhabited habitats on Mars. *Icarus* 2012;217(1):184–193; doi: 10.1016/j.icarus.2011.10.025

Cosmidis J, Templeton AS. Self-assembly of biomorphic carbon/sulfur microstructures in sulfidic environments. *Nat Commun* 2016;7(1):12812; doi: 10.1038/ncomms12812

Criouet I, Viennet J-C, Jacquemot P, *et al.* Abiotic formation of organic biomorphs under diagenetic conditions. *Geochem Perspect Lett* 2021;16:40–46; doi: 10.7185/geochemlet.2102

Czajka DR, Lion LW, Shuler ML, *et al.* Evaluation of the utility of bacterial extracellular polymers for treatment of metal-contaminated soils: Polymer persistence, mobility, and the influence of lead. *Water Res* 1997;31(11):2827–2839; doi: 10.1016/S0043-1354(97)00129-2

de Vries ST. *Early Archaean Sedimentary Basins: Depositional Environment and Hydrothermal Systems.* Faculty of Geosciences, Utretcht University: The Netherlands; 2004.

de Vries ST, Nijman W, Wijbrans JR, *et al.* Stratigraphic continuity and early deformation of the central part of the Coppin Gap Greenstone Belt, Pilbara, Western Australia. *Precambrian Res* 2006;147(1–2):1–27; doi: 10.1016/j.precamres.2006.01.004

de Vries ST, Nijman W, de Boer PL. Sedimentary geology of the Palaeoarchaean Buck Ridge (South Africa) and Kittys Gap (Western Australia) volcano-sedimentary complexes. *Precambrian Res* 2010;183(4):749–769; doi: 10.1016/j.precamres.2010.09.005

Derenne S, Robert F, Skrzypczak-Bonduelle A, *et al.* Molecular evidence for life in the 3.5 billion year old Warrawoona Chert. *Earth Planet Sci Lett* 2008;272(1–2):476–480; doi: 10.1016/j.epsl.2008.05.014

Des Marais DJ. Exploring Mars for evidence of habitable environments and life. *Proc Am Philos Soc* 2010;154(4): 23056860; doi: http://www.jstor.org/stable/23056860

Des Marais DJ, Nuth JA, Allamandola LJ, *et al*. The NASA Astrobiology Roadmap. *Astrobiology* 2008;8(4):715–730; doi: 10.1089/ast.2008.0819

Dong H, Huang L, Zhao L, *et al.* A critical review of mineral–microbe interaction and co-evolution: Mechanisms and applications. *Natl Sci Rev* 2022;9(10):nwac128; doi: 10.1093/nsr/nwac128

Dupont CL, Butcher A, Valas RE, *et al*. History of biological metal utilization inferred through phylogenomic analysis of protein structures. *Proc Natl Acad Sci U S A* 2010;107(23): 10567–10572; doi: 10.1073/pnas.0912491107

Eigenbrode JL, Summons RE, Steele A, *et al.* Organic matter preserved in 3-billion-year-old mudstones at Gale Crater, Mars. *Science* 2018;360(6393):1096–1101; doi: 10.1126/science.aas9185

Farley K, Stack K. *Mars 2020 Initial Reports.* Mars 2020 Science Team, California Institute of Technology; 2023. Available from: https://pds-geosciences.wustl.edu/m2020/urn-nasa-pds-mars2020_sample_dossier/initial_reports/initial_reports_volume2.pdf [Last accessed: July 23, 2023].

Farley KA, Williford KH, Stack KM, *et al.* Mars 2020 Mission overview. *Space Sci Rev* 2020;216(8):142; doi: 10.1007/s11214-020-00762-y

Farley KA, Stack KM, Shuster DL, *et al.* Aqueously altered igneous rocks sampled on the floor of Jezero Crater, Mars. *Science* 2022;377(6614):eabo2196; doi: 10.1126/science.abo2196

Foucher F, Ammar M-R, Westall F. Revealing the biotic origin of silicified Precambrian carbonaceous microstructures using Raman spectroscopic mapping, a potential method for the detection of microfossils on Mars: Revealing the biotic origin of silicified carbonaceous microstructures. *J Raman Spectrosc* 2015;46(10):873–879; doi: 10.1002/jrs.4687

Foucher F, Guimbretière G, Bost N, *et al.* Petrographical and mineralogical applications of Raman mapping. In: *Raman Spectroscopy and Applications*. (Maaz K. ed.) InTech: Rijeka; 2017; pp 163–180.

Foucher F, Hickman-Lewis K, Hutzler A, *et al.* Definition and use of functional analogues in planetary exploration. *Planet Space Sci* 2021;197:105162; doi: 10.1016/j.pss.2021.105162

Fraústo Da Silva JJR, Williams RJP. *The Biological Chemistry of the Elements: The Inorganic Chemistry of Life.* Oxford University Press: Oxford, United Kingdom; 2001.

Freissinet C, Glavin DP, Mahaffy PR, *et al.* Organic molecules in the Sheepbed Mudstone, Gale Crater, Mars: Detection of

organics in martian sample. *J Geophys Res Planets* 2015; 120(3):495–514; doi: 10.1002/2014JE004737

Gaft M, Reisfeld R, Panczer G. *Modern Luminescence Spectroscopy of Minerals and Materials.* Springer: Berlin, Heidelberg; 2015.

García-Ruiz JM, Hyde ST, Carnerup AM, *et al.* Self-assembled silica-carbonate structures and detection of ancient microfossils. *Science* 2003;302(5648):1194–1197; doi: 10.1126/science.1090163

García-Ruiz JM, Melero-García E, Hyde ST. Morphogenesis of self-assembled nanocrystalline materials of barium carbonate and silica. *Science* 2009;323(5912):362–365; doi: 10.1126/science.1165349

Gibson DT. *Microbial Degradation of Organic Compounds*. Marcel Dekker, Inc.: New York; 1984.

Gourcerol B, Thurston PC, Kontak DJ, *et al*. Interpretations and implications of LA ICP-MS analysis of chert for the origin of geochemical signatures in banded iron formations (BIFs) from the Meadowbank Gold Deposit, Western Churchill Province, Nunavut. *Chem Geol* 2015;410:89–107; doi: 10.1016/j.chemgeo.2015.06.008

Gourcerol B, Thurston PC, Kontak DJ, *et al*. Depositional setting of Algoma-type banded iron formation. *Precambrian Res* 2016;281:47–79; doi: 10.1016/j.precamres.2016.04.019

Gourier D, Binet L, Calligaro T, *et al.* Extraterrestrial organic matter preserved in 3.33 Ga sediments from Barberton, South Africa. *Geochim Cosmochim Acta* 2019;258:207–225; doi: 10.1016/j.gca.2019.05.009

Gratuze B. Obsidian characterization by laser ablation ICP-MS and its application to prehistoric trade in the Mediterranean and the Near East: Sources and distribution of obsidian within the Aegean and Anatolia. *J Archaeol Sci* 1999;26(8):869–881; doi: 10.1006/jasc.1999.0459

Gratuze B. Glass Characterization Using laser ablation-inductively coupled plasma-mass spectrometry methods. In: *Recent Advances in Laser Ablation ICP-MS for Archaeology.* (Dussubieux L, Golitko M, Gratuze B. eds) Springer Berlin Heidelberg: Berlin, Heidelberg; 2016; pp 179–196.

Grotzinger JP, Gupta S, Malin MC, *et al*. Deposition, exhumation, and paleoclimate of an ancient lake deposit, Gale Crater, Mars. *Science* 2015;350(6257):aac7575; doi: 10.1126/science.aac7575

Gueriau P, Réguer S, Leclercq N, *et al*. Visualizing mineralization processes and fossil anatomy using synchronous synchrotron X-ray fluorescence and X-ray diffraction mapping. *J R Soc Interface* 2020;17(169):20200216; doi: 10.1098/rsif.2020.0216

Hickman-Lewis K, Cavalazzi B, Foucher F, *et al.* Most ancient evidence for life in the Barberton Greenstone Belt: Microbial mats and biofabrics of the ~3.47 Ga Middle Marker Horizon. *Precambrian Res* 2018;312:45–67; doi: 10.1016/j.precamres.2018.04.007

Hickman-Lewis K, Gautret P, Arbaret L, *et al*. Mechanistic morphogenesis of organo-sedimentary structures growing under geochemically stressed conditions: Keystone to proving the biogenicity of some Archaean stromatolites? *Geosciences* 2019;9(8):359; doi: 10.3390/geosciences9080359

Hickman-Lewis K, Cavalazzi B, Sorieul S, *et al.* Metallomics in deep time and the influence of ocean chemistry on the metabolic landscapes of Earth's earliest ecosystems. *Sci Rep* 2020a;10(1):4965; doi: 10.1038/s41598-020-61774-w

Hickman-Lewis K, Gourcerol B, Westall F, *et al*. Reconstructing Palaeoarchaean microbial biomes flourishing in the presence of emergent landmasses using trace and rare earth element systematics. *Precambrian Res* 2020b;342:105689; doi: 10.1016/j.precamres.2020.105689

Hickman-Lewis K, Westall F, Cavalazzi B. Diverse communities of Bacteria and Archaea flourished in Palaeoarchaean (3.5–3.3 Ga) microbial mats. *Paleontology* 2020c;63(6): 1007–1033; doi: 10.1111/pala.12504

Hickman-Lewis K, Cavalazzi B, Giannoukos K, *et al.* Advanced two- and three-dimensional insights into Earth's oldest stromatolites (ca. 3.5 Ga): Prospects for the search for life on Mars. *Geology* 2022a;51(1):33–38; doi: 10.1130/G50390.1

Hickman-Lewis K, Moore KR, Hollis JJR, *et al. In situ* identification of Paleoarchean biosignatures using colocated Perseverance rover analyses: Perspectives for in situ Mars Science and Sample Return. *Astrobiology* 2022b;22(9):1143–1163; doi: 10.1089/ast.2022.0018

Igisu M, Nakashima S, Ueno Y, *et al.* In situ infrared microspectroscopy of ~850 million-year-old prokaryotic fossils. *Appl Spectrosc* 2006;60(10):1111–1120; doi: 10.1366/000370206778664707

Igisu M, Ueno Y, Shimojima M, *et al.* Micro-FTIR spectroscopic signatures of bacterial lipids in proterozoic microfossils. *World Summit Anc Microsc Foss* 2009;173(1):19–26; doi: 10.1016/j.precamres.2009.03.006

Igisu M, Takai K, Ueno Y, *et al.* Domain-level identification and quantification of relative prokaryotic cell abundance in microbial communities by micro-FTIR spectroscopy. *Environ Microbiol Rep* 2012;4(1):42–49; doi: 10.1111/j.1758-2229.2011.00277.x

Igisu M, Ueno Y, Takai K. FTIR microspectroscopy of carbonaceous matter in ~3.5 Ga seafloor hydrothermal deposits in the North Pole Area, Western Australia. *Prog Earth Planet Sci* 2018;5(1):85; doi: 10.1186/s40645-018-0242-1

Jelen BI, Giovannelli D, Falkowski PG. The role of microbial electron transfer in the coevolution of the biosphere and geosphere. *Annu Rev Microbiol* 2016;70(1):45–62; doi: 10.1146/annurev-micro-102215-095521

Kamber BS, Greig A, Collerson KD. A new estimate for the composition of weathered young upper continental crust from alluvial sediments, Queensland, Australia. *Geochim Cosmochim Acta* 2005;69(4):1041–1058; doi: 10.1016/j.gca.2004.08.020

Kasting JF. Box models for the evolution of atmospheric oxygen: An update. *Glob Planet Change* 1991;5(1–2):125–131; doi: 10.1016/0921-8181(91)90133-H

Keil RG, Mayer LM. Mineral matrices and organic matter. In: *Treatise on Geochemistry.* (Holland HD, Turekian KK. eds.) Elsevier: Amsterdam; 2014; pp 337–359.

Kisch HJ, Nijman W. Metamorphic grade from K-micas in the metasediments of the Pilbara and Barberton Greenstone Belts. In: *Field Forum on Processes on the Early Earth, Kaapvaal Craton, South Africa* (Reimold WU, Hofmann A, eds.) Johannesburg, University of Witwatersrand; 2004; pp 47–48.

Kouketsu Y, Mizukami T, Mori H, *et al.* A new approach to develop the Raman carbonaceous material geothermometer for low-grade metamorphism using peak width. *Isl Arc* 2014; 23(1):33–50; doi: 10.1111/iar.12057

Lawrence MG, Kamber BS. The behaviour of the rare Earth elements during estuarine mixing—Revisited. *Mar Chem* 2006;100(1–2):147–161; doi: 10.1016/j.marchem.2005.11.007

Lawrence MG, Greig A, Collerson KD, *et al.* Rare Earth element and yttrium variability in south east Queensland Waterways. *Aquat Geochem* 2006;12(1):39–72; doi: http://link.springer.com/10.1007/s10498-005-4471-8

Liermann LJ, Hausrath EM, Anbar AD, *et al.* Assimilatory and dissimilatory processes of microorganisms affecting metals in the environment. *J Anal At Spectrom* 2007;22(8):867; doi: 10.1039/b705383e

Lin R, Ritz GP. Studying individual Macerals using Ir microspectrometry, and implications on oil versus gas/condensate proneness and ''low-rank'' generation. *Org Geochem* 1993; 20(6):695–706; doi: 10.1016/0146-6380(93)90055-G

Lindsay JF, Brasier MD, McLoughlin N, *et al.* The problem of deep carbon—An Archean paradox. *Precambrian Res* 2005; 143(1–4):1–22; doi: 10.1016/j.precamres.2005.09.003

MacRae CM, Wilson NC. Luminescence database I—Minerals and materials. *Microsc Microanal* 2008;14(2):184–204; doi: doi:10.1017/S143192760808029X

Mangold N, Dehouck E, Fedo C, *et al.* Chemical alteration of fine-grained sedimentary rocks at Gale Crater. *Icarus* 2019; 321:619–631; doi: 10.1016/j.icarus.2018.11.004

Mathez EA. Carbonaceous matter in mantle xenoliths: Composition and relevance to the isotopes. *Geochim Cosmochim Acta* 1987;51(9):2339–2347; doi: 10.1016/0016-7037(87)90288-2

Maurette M. *Micrometeorites and the Mysteries of Our Origins*. Springer: Berlin, Heidelberg; 2006.

Maurette M, Duprat J, Engrand C, *et al.* Accretion of neon, organics, CO2, nitrogen and water from large interplanetary dust particles on the early Earth. *Planet Space Sci* 2000;48(11):1117–1137; doi: 10.1016/S0032-0633(00)00086-6

McKay CP, Stoker CR. The early environment and its evolution on Mars: Implication for life. *Rev Geophys* 1989;27(2):189; doi: 10.1029/RG027i002p00189

McMahon S, Bosak T, Grotzinger JP, *et al*. A field guide to finding fossils on Mars. *J Geophys Res Planets* 2018;123(5): 1012–1040; doi: 10.1029/2017JE005478

Meadows V, Graham H, Abrahamsson V, *et al.* Community report from the biosignatures standards of evidence workshop. *arXiv Preprint* 2022;2022:arXiv221014293.

Ménez B, Pisapia C, Andreani M, *et al*. Abiotic synthesis of amino acids in the recesses of the oceanic lithosphere. *Nature* 2018;564(7734):59–63; doi: 10.1038/s41586-018-0684-z

Millan M, Williams AJ, Mcadam AC, *et al.* Sedimentary organics in Glen Torridon, Gale Crater, Mars: Results from the SAM instrument suite and supporting laboratory analyses. *J Geophys Res Planets* 2022;127(11):e2021JE007107; doi: 10.1029/2021JE007107

Mlewski EC, Pisapia C, Gomez F, *et al.* Characterization of pustular mats and related *Rivularia*-rich laminations in oncoids from the Laguna Negra Lake (Argentina). *Front Microbiol* 2018;9:996; doi: 10.3389/fmicb.2018.00996

Moore EK, Jelen BI, Giovannelli D, *et al.* Metal availability and the expanding network of microbial metabolisms in the Archaean Eon. *Nat Geosci* 2017;10(9):629–636; doi: 10.1038/ngeo3006

Nakamura K, Takai K. Theoretical constraints of physical and chemical properties of hydrothermal fluids on variations in chemolithotrophic microbial communities in seafloor hydrothermal systems. *Prog Earth Planet Sci* 2014;1(1):5; doi: 10.1186/2197-4284-1-5

Neveu M, Hays LE, Voytek MA, *et al.* The ladder of life detection. *Astrobiology* 2018;18(11):1375–1402; doi: 10.1089/ast.2017.1773

Noffke N. The criteria for the biogeneicity of microbially induced sedimentary structures (MISS) in Archean and younger, sandy deposits. *Earth Sci Rev* 2009;96(3):173–180; doi: 10.1016/j.earscirev.2008.08.002

Noffke N. Ancient sedimentary structures in the <3.7 Ga Gillespie Lake Member, Mars, that resemble macroscopic morphology, spatial associations, and temporal succession in terrestrial microbialites. *Astrobiology* 2015;15(2):169–192; doi: 10.1089/ast.2014.1218

Orange F, Disnar J-R, Westall F, *et al*. Metal cation binding by the hyperthermophilic microorganism, Archaea *Methanocaldococcus jannaschii*, and its effects on silicification. *Palaeontology* 2011;54(5):953–964; doi: 10.1111/j.1475-4983.2011.01066.x

Orberger B, Rouchon V, Westall F, *et al.* Microfacies and origin of some Archean cherts (Pilbara, Australia). In: *Processes on the Early Earth.* (Reimold WU, Gibson RL. eds.) Geological Society of America: New York; 2006; pp 133–156.

Orell A, Schopf S, Randau L, *et al.* Biofilm lifestyle of thermophile and acidophile archaea. *Biocommun Archaea* 2017; 133–146; doi: 10.1007/978-3-319-65536-9_9

Rampe EB, Blake DF, Bristow TF, *et al.* Mineralogy and geochemistry of sedimentary rocks and eolian sediments in Gale Crater, Mars: A review after six Earth years of exploration with Curiosity. *Geochemistry* 2020;80(2):125605; doi: 10.1016/j.chemer.2020.125605

Rasmussen B, Buick R. Oily old ores: Evidence for hydrothermal petroleum generation in an Archean volcanogenic massive sulfide deposit. *Geology* 2000;28(8):731–734; doi: 10.1130/0091-7613(2000)28<731:OOOEFH >2.0.CO;2

Rasmussen B, Muhling JR, Fischer WW. Ancient oil as a source of carbonaceous matter in 1.88-billion-year-old gunflint stromatolites and microfossils. *Astrobiology* 2021;21(6): 655–672; doi: 10.1089/ast.2020.2376

Razzell Hollis J, Sharma S, Abbey W, *et al.* A deep ultraviolet Raman and fluorescence spectral library of 51 organic compounds for the SHERLOC instrument onboard Mars 2020. *Astrobiology* 2023;23(1):1–23; doi: 10.1089/ast.2022.0023

Rickaby REM. Goldilocks and the three inorganic equilibria: How Earth's chemistry and life coevolve to be nearly in tune. *Philos Trans R Soc Math Phys Eng Sci* 2015;373(2037): 20140188; doi: 10.1098/rsta.2014.0188

Robbins LJ, Lalonde SV, Planavsky NJ, *et al.* Trace elements at the intersection of marine biological and geochemical evolution. *Earth Sci Rev* 2016;163:323–348; doi: 10.1016/j.earscirev.2016.10.013

Rouzaud JN, Oberlin A. Structure, microtexture, and optical properties of anthracene and saccharose-based carbons. *Carbon* 1989;27(4):517–529; doi: 10.1016/0008-6223(89)90002-X

Ruff SW, Farmer JD. Silica deposits on mars with features resembling hot spring biosignatures at El Tatio in Chile. *Nat Commun* 2016;7(1):13554; doi: 10.1038/ncomms13554

Scheller EL, Razzell Hollis J, Cardarelli EL, *et al*. Aqueous alteration processes in Jezero Crater, Mars—Implications for organic geochemistry. *Science* 2022;378(6624):1105–1110; doi: 10.1126/science.abo5204

Schidlowski M. Carbon isotopes as biogeochemical recorders of life over 3.8 Ga of Earth history: Evolution of a concept. *Precambrian Res* 2001;106(1–2):117–134; doi: 10.1016/S0301-9268(00)00128-5

Schultze-Lam S, Fortin D, Davis BS, *et al.* Mineralization of bacterial surfaces. *Chem Geol* 1996;132(1–4):171–181; doi: 10.1016/S0009-2541(96)00053-8

Sephton MA. Organic compounds in carbonaceous meteorites. *Nat Prod Rep* 2002;19(3):292–311; doi: 10.1039/B103775G

Sforna MC, Loron CC, Demoulin CF, *et al*. Intracellular bound chlorophyll residues identify 1 Gyr-old fossils as eukaryotic Algae. *Nat Commun* 2022;13(1):146; doi: 10.1038/s41467-021-27810-7

Sharma S, Roppel RD, Murphy AE, *et al.* Diverse organic-mineral associations in Jezero Crater, Mars. *Nature* 2023; 619(7971):724–732; doi: 10.1038/s41586-023-06143-z

Simon JI, Hickman-Lewis K, Cohen BA, *et al*. Samples collected from the floor of Jezero Crater with the Mars 2020 Perseverance rover. *J Geophys Res Planets* 2023;128(6): e2022JE007474; doi: 10.1029/2022JE007474

Steele A, McCubbin FM, Fries M, *et al*. A reduced organic carbon component in martian basalts. *Science* 2012; 337(6091):212; doi: 10.1126/science.1220715

Steele A, McCubbin FM, Fries MD. The provenance, formation, and implications of reduced carbon phases in martian meteorites. *Meteorit Planet Sci* 2016;51(11):2203–2225; doi: 10.1111/maps.12670

Steele A, Benning LG, Wirth R, *et al*. Organic synthesis on Mars by electrochemical reduction of CO2. *Sci Adv* 2018; 4(10):eaat5118; doi: 10.1126/sciadv.aat5118

Summons RE, Amend JP, Bish D, *et al*. Preservation of martian organic and environmental records: Final report of the Mars Biosignature Working Group. *Astrobiology* 2011;11(2):157–181; doi: 10.1089/ast.2010.0506

Tarnas JD, Mustard JF, Lin H, *et al.* Orbital identification of hydrated silica in Jezero Crater, Mars. *Geophys Res Lett* 2019;46(22):12771–12782; doi: 10.1029/2019GL085584

van den Boorn SHJM, van Bergen MJ, Vroon PZ, *et al*. Silicon isotope and trace element constraints on the origin of ~3.5Ga Cherts: Implications for early Archaean marine environments. *Geochim Cosmochim Acta* 2010;74(3):1077–1103; doi: 10.1016/j.gca.2009.09.009

Vago JL, Westall F, Pasteur Instrument Teams LSSWG and Other Contributors, *et al.* Habitability on early Mars and the search for biosignatures with the ExoMars Rover. *Astrobiology* 2017;17(6–7):471–510; doi: 10.1089/ast.2016.1533

van Wolferen M, Orell A, Albers S-V. Archaeal biofilm formation. *Nat Rev Microbiol* 2018;16(11):699–713; doi: 10.1038/s41579-018-0058-4

Velbel MA, Cockell CS, Glavin DP, *et al*. Planning implications related to sterilization-sensitive science investigations associated with Mars Sample Return (MSR). *Astrobiology* 2022;22(Suppl 1):S112–S164.

Wacey D. *Early Life on Earth: A Practical Guide*. Springer: Dordrecht; 2009.

Westall F, de Vries ST, Nijman W, *et al.* The 3.466 Ga ''Kitty's Gap Chert,'' an Early Archean microbial ecosystem. In: *Processes on the Early Earth.* (Reimold WU, Gibson RL. eds.) Geological Society of America: New York; 2006; pp 105–131.

Westall F, Foucher F, Cavalazzi B, *et al.* Volcaniclastic habitats for early life on Earth and Mars: A case study from ~3.5Ga-old rocks from the Pilbara, Australia. *Planet Space Sci* 2011; 59(10):1093–1106; doi: 10.1016/j.pss.2010.09.006

Westall F, Loizeau D, Foucher F, *et al.* Habitability on Mars from a microbial point of view. *Astrobiology* 2013;13(9): 887–897; doi: 10.1089/ast.2013.1000

Westall F, Campbell KA, Bréhéret JG, *et al*. Archean (3.33 Ga) microbe-sediment systems were diverse and flourished in a hydrothermal context. *Geology* 2015a;43(7):615–618; doi: 10.1130/G36646.1

Westall F, Foucher F, Bost N, et al. Biosignatures on Mars: What, where, and how? Implications for the search for martian life. *Astrobiology* 2015b;15(11):998–1029; doi: 10.1089/ast.2015.1374

Westall F, Brack A, Fairén AG, *et al.* Setting the geological scene for the origin of life and continuing open questions about its emergence. *Front Astron Space Sci* 2023;9: 1095701; doi: 10.3389/fspas.2022.1095701

Williams RJP, Fraústo Da Silva JJR. Evolution was chemically constrained. J Theor Biol 2003;220(3):323–343; doi: 10.1006/jtbi.2003.3152

Zerkle AL. Biogeochemical signatures through time as inferred from whole microbial genomes. *Am J Sci* 2005;305(6–8): 467–502; doi: 10.2475/ajs.305.6-8.467

Zhyrovetsky VM, Popovych DI, Savka SS, *et al.* Nanopowder metal oxide for photoluminescent gas sensing. *Nanoscale Res Lett* 2017;12:1–5; doi: 10.1186/s11671-017-1891-5

Address correspondence to:
Frances Westall
CNRS-Centre de Biophysique Moléculaire
Avenue de la Recherche Scientifique
Orléans 45071
France

E-mail: frances.westall@cnrs.fr

Submitted 25 July 2023
Accepted 1 January 2024
Associate Editor: Sherry L. Cady

Abbreviations Used

μPIXE = microscale proton-induced X-ray emission
CM = carbonaceous matter
DUV = deep-ultraviolet
EDX = energy dispersive X-ray
EPS = extracellular polymeric substances
FIB = focused ion beam
FTIR = Fourier transform infrared
HR = high-resolution
HREE = heavy rare earth elements
ICP-OES = inductively coupled plasma optical emission spectrometry
IR = infrared
ISAR = International Space Analogue Rock Store
LA = laser ablation
LREE = light rare earth elements
MS = mass spectrometry
MSR = Mars Sample Return
MuQ = Mud from Queensland
RBS = Rutherford Backscattering Spectrometry
REE = rare earth elements
ROI = region of interest
SEM = scanning electron microscopy
S-TEM = scanning transmission electron microscopy
XRF = X-ray fluorescence